Title
Geometry and Dynamics of Active Topological Defects

Author
Vafa, Farzan

Publication Date
2021

University of California
Santa Barbara

Geometry and Dynamics of Active Topological Defects

A dissertation submitted in partial satisfaction
of the requirements for the degree

Doctor of Philosophy
in
Physics

by

Farzan Vafa

Committee in charge:

Professor Boris Shraiman, Chair
Professor M. Cristina Marchetti
Professor Zvonimir Dogic

June 2021

The Dissertation of Farzan Vafa is approved.

Professor M. Cristina Marchetti

Professor Zvonimir Dogic

Professor Boris Shraiman, Committee Chair

May 2021

Geometry and Dynamics of Active Topological Defects

To my parents Afarin and Cumrun

Acknowledgements

There are too many people to properly thank and acknowledge here to do it justice in the little space I have, but nonetheless I will try.

First, I would like to thank my advisor Boris I. Shraiman for introducing me to the world of biophysics. I am deeply grateful for your wisdom, patience, and guidance. Your door was always open.

Thank you M. Cristina Marchetti and Mark Bowick for welcoming me to the world of active matter. Thank you M. Cristina Marchetti also for creating and fostering a congenial active matter community.

I'm also grateful for Zvonimir Dogic for agreeing to serve on both my advancement to candidacy as well as my thesis defense committees.

Thank you Cenke Xu for letting me try hard condensed matter physics. You genuinely cared about my well-being and helped me build a solid foundation.

Thank you Sebastian Streichan for introducing me to and teaching me about developmental biology and the world of experiments, as well as the many patient explanations of intricacies of Matlab.

Thank you David Nelson and L Mahadevan for welcoming me into your groups. I have learned a lot and on a variety of different subjects. Thank you L Mahadevan also for the wonderful collaboration on our morphogenesis project.

For the many science discussions, thank you members of Boris' group: Dillon Cislo, Nicholas Noll, Nikolas Claussen, and Shahriar Shadkhoo; Sebastian's group: Aimal Khankel, Hannah Gustafson, and Vishank Jain-Sharma; and Cristina's and Mark's groups: Arthur Hernandez, Austin Hopkins, Paarth Gulati, Zhihong You, Zhitao Chen, and Sattvic Ray from Zvonimir Dogic's group, as well as Michael Landry. I would also like to thank my collaborators whose projects I am not covering in this thesis: Biao Lian, Chunxiao Liu, and Shoucheng Zhang. It has been a pleasure interacting with all of you.

There is life outside of physics. . Thank you Sicheng Wang for the tennis. Thank you Neelay Fruitwalla for the squash. Thank you Mark Arildsen for the trips. Thank you Gabriel Treviño Verastegui and Peter Dotti for being wonderful housemates. Thank you Dan Kutner for the trivia. Thank you Wayne Weng and Jared Goldberg for the walks. Thank you Amber Cai for the board games and classical music. Thank you Seth Koren for the various excursions. Thank you Alex for the hikes.

Thank you to UCSB student organizations Iranian Graduate Student Association and Persian Student Group for keeping me connected to my culture.

Thank you my grandparents Baba Javad, Maman Simeen, Maman Foroogh, and Baba Nasser for encouraging me to pursue excellence in all forms. Last but not least, thank you my parents Afarin and Cumrun for being there and supporting me from the beginning and my brothers Keyon and Neekon for being the best little brothers.

Curriculum Vitæ

Farzan Vafa

Education

2021	Ph.D. in Physics (Expected), University of California, Santa Barbara.
2019	M.A. in Physics, University of California, Santa Barbara.
2015	B.A. with Honors in Physics and Mathematics, Harvard College.

Publications

1. F. Vafa and L. Mahadevan, “Active nematic defects and epithelial morphogenesis,” arXiv:2105.01067 [cond-mat.soft].
2. F. Vafa, M. J. Bowick, B. I. Shraiman, and M. C. Marchetti, “Fluctuations can induce local nematic order and extensile stress in monolayers of motile cells,” Soft Matter 17 (2021) 3068–3073.
3. F. Vafa, “Defect dynamics in active polar fluids vs. active nematics,” arXiv:2009.10723 [cond-mat.soft].
4. F. Vafa, M. J. Bowick, M. C. Marchetti, and B. I. Shraiman, “Multi-defect dynamics in active nematics,” arXiv:2007.02947 [cond-mat.soft].
5. C. Liu, F. Vafa, and C. Xu, “Symmetry-protected topological hopf insulator and its generalizations”, Phys. Rev. B, vol. 95, p. 161 116, 16 Apr. 2017.
6. B. Lian, C. Vafa, F. Vafa, and S.-C. Zhang, “Chern-simons theory and wilson loops in the brillouin zone”, Phys. Rev. B, vol. 95, p. 094 512, 9 Mar. 2017.

Abstract

Geometry and Dynamics of Active Topological Defects

by

Farzan Vafa

In this thesis, we study aspects of active matter with the aim of application to biological systems and processes such as morphogenesis, using tools and ideas from condensed matter physics, non-equilibrium physics, topology, and geometry.

We begin by examining the origin of local nematic order and extensile stress. We develop a mesoscopic model where tissue flow is generated by fluctuating traction forces coupled to the nematic order parameter, and show that the resulting tissue dynamics can spontaneously produce local nematic order and an extensile internal stress. A key assumption of the model is that in the presence of local nematic alignment, cells preferentially crawl along the nematic axis, resulting in anisotropy of fluctuations.

Assuming the existence of active stresses and local nematic order, for example generated via the noise mechanism discussed here, we study the dynamics of 2D active nematics, for which topological defects play a key role. We employ the power of complex analysis to study defects in the deep nematic limit where the nematic texture is determined by the defect positions. In particular, the polarization of a defect is not an independent degree of freedom, but rather is directly determined by the position of all of the other defects. Relaxational dynamics leads to a set of coupled ordinary differential equations for the defect positions. We discover novel dynamical aspects of defects, including a position-dependent "collective mobility" matrix, and non-central and non-reciprocal pair-wise interactions. We consider extensions and applications of this model, including excited states, continuum model, and different geometries and topologies, as well as for active polar fluids and its orientation dynamics. In particular, we highlight that for contractile (extensile) active nematic systems, $+1$ vortices (asters) should emerge as bound states of a pair of $+1/2$ defects, which has been recently observed.

Combining what we have learned about defect dynamics and inspired by recent experiments that highlight the role of nematic defects on the morphogenesis of epithelial tissues, we develop a minimal framework to study the dynamics of an active nematic on a curved surface which itself deforms in response to the nematic field. Allowing also the geometry of the surface to evolve via relaxational dynamics leads to a theory linking nematic defect dynamics, cellular division rates, and Gaussian curvature. Regions of large positive (negative) curvature and positive (negative) growth are colocalized with the presence of positive (negative) defects. Applying this framework to the dynamics of cultured murine neural progenitor cells (NPCs) in an ex-vivo setting, we find that cells accumulate at positive defects and form mounds, and that cells are depleted at negative defects. In contrast, applying this to the dynamics of a basal marine invertebrate *Hydra* in an in-vivo setting, we show that a bound $+1$ defect state surrounded by two $-1/2$ defects can create a stationary ring configuration of tentacles, consistent with observations.

Contents

Chapter 1

Introduction

1.1 Order parameter, topological defects, and non-equilibirum physics

1.1.1 Order parameter

[?]

A fundamental challenge of condensed matter physics is to classify and understand the various possible phases of matter. Phases of matter are generally classified by broken symmetries. For example, a crystal breaks translational order, a liquid crystal breaks rotational invariance, a ferromagnet breaks spin rotational invariance, and a superconductor breaks gauge symmetry. Formally, this paradigm is known as "spontaneous symmetry breaking," and can be used to describe both classical and quantum phases transitions [1]. Introduced by Landau [2], a non-zero object called the "order parameter," which quantities the amount of symmetry breaking, can distinguish the broken-symmetry phase from the symmetry preserving phase. Landau subsequently developed an effective field theory in terms of the order parameter and its variations in space, an early example being superconductivity [3].

1.1.2 Topological defects

We now turn our discussion to topological defects, which are discontinuities of the order parameter [4, 5]. They come up in many different areas of physics, ranging from continuum solids [6], crystalline solids [7, 8, 9], liquid crystals [10, 11, 12, 13], Skyrmions [14], cosmology [15, 16, 17], superconductors, superfluids, kink, vortex, magnetic monopole [18, 19], instantons in Yang-Mills [20]. Mathematically speaking, topological defects are non-trivial configurations which arise from non-trivial topology of field space, and are classified by homotopy theory [21]. They are the lowest-energy excitations of the homogeneous ordered state or ground state for a given topological charge. Equivalently, they can be treated as particles or extended objects, and sometimes provide a dual description of the order parameter [22], such as solitons in the Sine-Gordon model which are dual to fermions [23].

1.1.3 Non-equilibrium physics

The discussion up to now has been in the context of systems in equilibrium, where much progress has been made. However, much of the real world is out of equilibrium. There are numerous ways for a system to be out of equilibrium. For example, the system can be prepared in a non-equilibrium state and simply be allowed to relax to its equilibrium state without any energy input [24]. Another example is that the system can be externally driven, such as in the bulk, as seen in sedimentation [25] or periodically driven (Floquet) systems [26, 27], or along the boundary, as seen in sheared turbulent fluids [28] or in Rayleigh–Bénard convection [29, 30, 31]. Here, though, motivated by living matter, we shall focus on yet another way.

1.2 Active Matter

Living matter differ from nonliving matter in that they can adapt, reproduce, evolve, process information, autonomously move, dynamically organize, and do work. To simplify the enormous complexity of living systems, we shall restrict ourselves to a rather common class of living systems called active matter [32, 33, 34, 35]. In active matter, the agents are active, that is they can self-propel, the self-propulsion sustained by continuously taking in and consuming energy from the surrounding environment [36]. Moreover, the driving is local, for example, at the level of each particle or agent, and breaks detailed balance [37, 38]. We shall adopt the viewpoint that active matter as a novel class of internally drive nonequilibrium system can be used to study living systems using techniques and tools from condensed matter physics [39, 32, 40].

In the past couple of decades, there has been an increasing number of experimental realizations of active matter in both living and synthetic systems [41]. Among living systems, examples cover a vast array of length scales, ranging from the macroscopic scale, such as bird flocks [42, 43], fish schools [44, 45], sheep herds [46], insect swarms [47, 48, 49, 50] and human crowds [51, 52, 53, 54], to the intermediate mesocopic scale, such as bacteria collectives [55, 56, 57, 58, 59, 60, 61], sperm cells [62], and cellular monolayers [63, 64, 65, 66, 67, 68, 69, 70, 71, 72], and even all the way down to the microscopic scale, such as sub-cellular structures [73, 74]. Synthetic model active systems are similarly diverse, examples including vibrated grains [75, 76, 77], self-propelled colloids [78, 79], artificial robots [80, 81, 82] and liqiud crystals consisting of biofilaments [83, 84, 85, 86, 87, 88].

Since active units such as cells or bacteria are often elongated in shape, we can model them as rods. In this case, the active units can align, locally developing two types of orientional order: apolar (nematic), where there is head-tail symmetry of the rods, or polar (vectorial), where there is no head-tail symmetry of the rods. We shall discuss both types of order separately in the following two sections, restricted to two dimenions. However, we before do that, we would like to make a final comment. Although this thesis is by no means a historical review, we would like to point out that the active matter idea is not completely new. In [89], the authors posited that active stresses can arise from metabolic activity in the fluid, and liquid crystal textures were observed in [90]. However, the active matter framework to explain the nonequilibrium behavior had not been developed yet and thus was lacking until recently [33].

1.2.1 Nematics

Examples of active nematics include cell sheets [66, 67, 68, 70], suspensions of cytoskeletal filaments and associated motor proteins [84, 85, 88], bacteria collectives [91, 60, 61], vibrated granular rods [75], and developing organisms [72]. For sufficiently large activity, topological defects proliferate in the nematic texture [92, 93, 94, 95, 96], and understanding of the dynamics of topological defects has been advanced by treating the defects as quasiparticles [85, 75, 92, 97, 98, 99, 100, 101]. We will follow this perspective.

With this qualitative overview, we now become a bit more quantitative and technical. We will first review the topological and geometric properties of defects in the passive case. We will then demonstrate, following the argument presented in [102], that the nematic order can induce stress, which through the activity will modify the dynamics of defects.

The nematic order can be described by the unit nematic director field $\hat{\mathbf{n}}$, with $\hat{\mathbf{n}} = -\hat{\mathbf{n}}$ reflecting the head-tail symmetry. However, $\hat{\mathbf{n}}$ does not describe the magnitude of the order, which would be useful in the presence of defects. Since we are interested in defects, we consider the nematic order parameter $\mathbf{Q}$, defined to be

$$Q^{\mu\nu} = A[\hat{n}^{\mu}\hat{n}^{\nu} - \frac{1}{2}\delta^{\mu\nu}], \tag{1.1}$$

where A is the magnitude of the nematic order. Another advantage of using $\mathbf{Q}$ instead of $\hat{\mathbf{n}}$ is that $\mathbf{Q}$ automatically enforces the nematic symmetry. A two-dimensional passive nematic, also known as a liquid crystal, is described by the Landau-de Gennes free energy [10, 5], $\mathcal{F}(\{\mathbf{Q}\})$,

$$\mathcal{F}(\{\mathbf{Q}\}) = \frac{1}{2}\int dxdy \left[K\ Tr(\boldsymbol{\nabla}\mathbf{Q})^2 + g[1 - 2Tr(\mathbf{Q}^2)]^2\right] \ , \tag{1.2}$$

with $2D$ traceless tensor order parameter of the form

$$Q_{ab} = A[\hat{n}_a\hat{n}_b - \frac{1}{2}\delta_{ab}] \tag{1.3}$$

expressed in terms of the position dependent director field $\hat{\mathbf{n}}$. The rigidity parameter, K, defines the energetic cost of spatial variation of $\mathbf{Q}$ (for simplicity we consider the single Frank constant approximation) and g, with units of energy density, controls the strength of nematic order, via the coherence length $\xi = \sqrt{K/2g}$ controls spatial variations in the magnitude of the order parameter A.

Since are in 2D, it is useful to work in complex coordinates. In terms of the complex positional coordinates $z = x+iy$ and $\bar{z} = x-iy$, and the complex order parameter [103, 10]

$$Q = (Q_{xx} - Q_{yy}) + i2Q_{xy} = Ae^{i\theta} \ , \tag{1.4}$$

the (dimensionless) LdG free energy has the form

$$\mathcal{F}(\{Q\}) = \int dzd\bar{z}\left[4|\partial Q|^2 + \epsilon^{-2}(1 - |Q|^2)^2\right] \ , \tag{1.5}$$

where $\partial = \partial_z = \frac{1}{2}[\partial_x - i\partial_y]$ (and $\bar{\partial} = \partial_{\bar{z}} = \frac{1}{2}[\partial_x + i\partial_y]$).

Stationary textures in the passive case minimize the LdG free energy and hence solve [10, 104]

$$\frac{\delta\mathcal{F}}{\delta\bar{Q}} = -4\bar{\partial}\partial Q - 2\epsilon^{-2}(1 - |Q|^2)Q = 0 \ . \tag{1.6}$$

We look for a solution for a single defect of charge σ of the form

$$Q = A(r)e^{2i\sigma\varphi} \ . \tag{1.7}$$

$A(r)$ would thus satisfy

$$A''(r) + \frac{A'}{r} + \left(2\epsilon^{-2} - \frac{4\sigma^2}{r^2} - 2\epsilon^{-2}A^2\right) A = 0 \ . \tag{1.8}$$

For example, for $\sigma = \pm 1/2$, $A(r)$ can be approximated as [104]

$$A(r) = \tilde{r}\sqrt{\frac{.68 + .28\tilde{r}^2}{1 + .82\tilde{r}^2 + .28\tilde{r}^4}} \ , \tag{1.9}$$

where $\tilde{r} = r/\epsilon$. As $r \to 0$, $A(r) \propto r$, and for $r \gg \epsilon$, $A(r) \simeq 1 - \frac{\epsilon^2}{4r^2}$. The defect core size a, which is the length scale over which A goes from 0 to 1, is of the order $a \sim \epsilon$.

Nematic defects are characterized by their charge, which is half-integral. Formally, this is due to the fact that $\pi_1\mathbb{RP}^1 = \mathbb{Z}/2$. For example, the director of a $\pm 1/2$ defect rotates by $\pm\pi$ as it goes around a circle, so its charge is $\pm\pi/(2\pi) = \pm 1/2$. See Fig. 1.1 for a sketch.

We now discuss the geometrical properties of $\pm 1/2$ defects. A $+1/2$ defect has a single axis of symmetry, and a $-1/2$ defect has three axis of symmetry. Thus if detects were to self-propel, we would expect the $+1/2$ defect to propel along its symmetry axis (either in the direction of the comet or opposite it), and for the $-1/2$ defect to be stationary because of the three-fold symmetry. We will formalize this idea of phase dependence of motility once we introduce activity.

Before we introduce the activity, we will compute the free energy in the passive case for a pair of defects. The free energy takes the form [10, 5]

$$\mathcal{F} \sim -\sigma_i\sigma_j \ln\frac{r}{L} \tag{1.10}$$

where σ_i and σ_j are the charges of defects i and j, separated by distance r, and L is the system size. We thus get the 2D Coulomb potential, which tells us that in the passive case, the defects interact with each other like point charges in electricity and magnetism.

We now introduce the activity. Suppose we have a collection of self-propelled particles (SPP), which we model as rods. At time t, rod α has axis $\hat{\mathbf{n}}_\alpha(t)$, with center $\mathbf{r}_\alpha(t)$ and

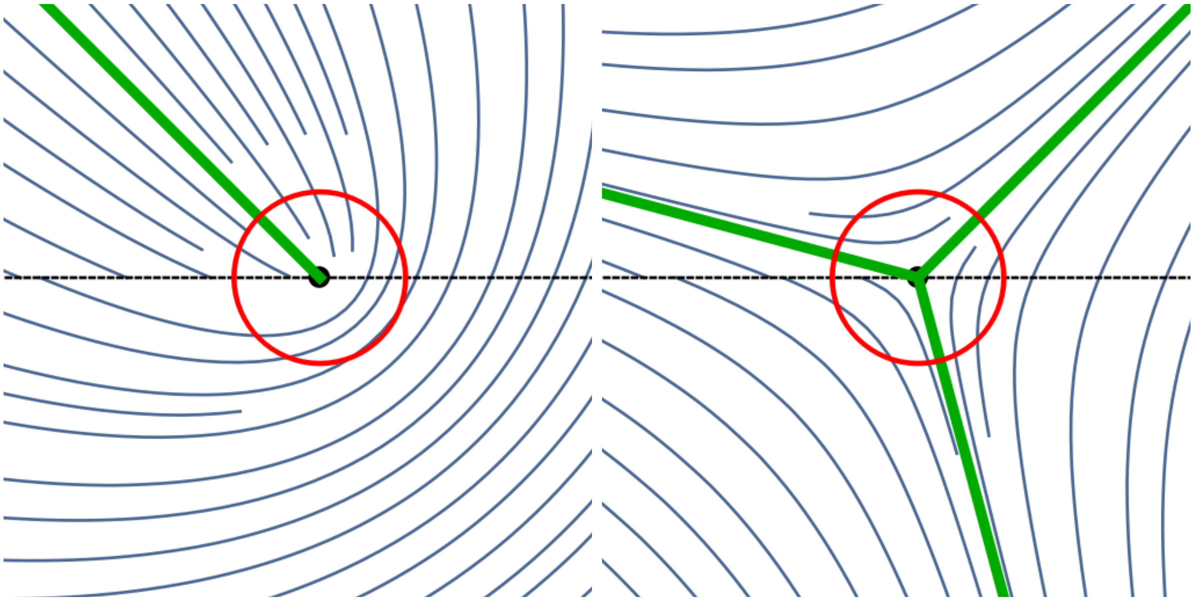

(a) +1/2 defect (b) −1/2 defect

Figure 1.1: Sketches of single defect textures for (a) a +1/2 and (b) a −1/2 defect, where green lines indicate the axes of symmetry.

endpoints $\mathbf{r}_\alpha \pm a$. It also experiences point forces equal magnitude f on its ends, along its axis $\pm\hat{\mathbf{n}}$. See Fig. 1.2 for a sketch. In the context of cells, f can arise for example from myosin motors or intercellular forces. Summing over all of the rods yields a force density

$$\mathbf{f}(\mathbf{r},t) = \pm f \sum_\alpha \hat{\mathbf{n}}_\alpha(t)[\delta(\mathbf{r}-\mathbf{r}_\alpha(t)-a\hat{\mathbf{n}}_\alpha(t)) - \delta(\mathbf{r}-\mathbf{r}_\alpha(t)+a\hat{\mathbf{n}}_\alpha(t))] \tag{1.11}$$

Expanding the delta functions about $\mathbf{r}_\alpha$ gives

$$f^i(\mathbf{r},t) = \mp a f \partial_j \sum_\alpha \hat{\mathbf{n}}^i_\alpha \hat{\mathbf{n}}^j_\alpha \delta(\mathbf{r}-\mathbf{r}_\alpha) + \mathcal{O}(\nabla^2) \tag{1.12}$$

Coarse-graining leads to

$$f^i(\mathbf{r},t) = \alpha \partial_j Q^{ij} \tag{1.13}$$

where

$$Q^{ij} = \hat{n}^i \hat{n}^j - \frac{1}{d}\delta^{ij} \tag{1.14}$$

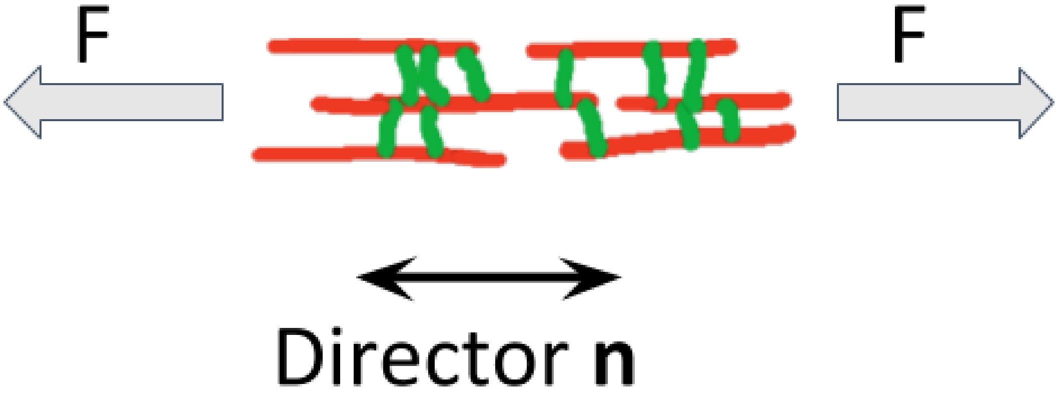

Figure 1.2: Cartoon of stress induced by nematic order (the example of actomyosin filaments).

known as the nematic tensor, or alignment tensor, takes the form of a stress (and d is dimension of space). The paramater α is known as the activity, with $\alpha > 0$ ($\alpha < 0$) denoting contractile (extensile) activity. Now if we evaluate $\mathbf{\nabla} \cdot \mathbf{Q}$ for a single $\pm 1/2$ defect configuration at the location of the ± 12 defect, we see that for a $+1/2$ defect, it points towards (away from) the comet for extensile (contractile) activity, but vanishes for a $-1/2$ defect. This is consistent with our expectations about the difference in motility between $\pm 1/2$ defects due to symmetry. We will later see in Chapter 3 that this phase dependence will play a crucial role in our analysis of defect dynamics.

1.2.2 Polar fluids

Examples of polar fluids include groups of animals [42, 43, 44, 45, 46, 47, 48, 49, 50, 51, 52, 53, 54], bacterial suspensions [55, 56, 57, 58], sperm cells [62], and cellular monolayers [65]. In contrast to active nematics, since active polar fluids have long range order [105, 106], defects are not spontaneously generated, and if generated due to boundary effect for example, the defects are expected to be transient [107, 108, 109]. That being said, aspects of dynamics of defects in active polar fluids have been studied in [110, 111, 112, 113, 114, 115, 107].

With this qualitative overview, we now become a bit more quantitative and technical. Here we review the topological and geometric properties of defects in the passive case, which will be useful to us in this dissertation.

We consider a two-dimensional polar fluid with density ρ and vector order parameter $\mathbf{p}$ described by the free energy [10, 116] $\mathcal{F}(\{\mathbf{p}\})$:

$$\mathcal{F}(\{\mathbf{p}\}) = \mathcal{F}_n(\{\mathbf{p}\}) + \mathcal{F}_p(\{\mathbf{p}\}) \ , \tag{1.15}$$

where

$$\mathcal{F}_n(\{\mathbf{p}\}) = \frac{1}{2}\int dxdy \left[C\left(\frac{\delta\rho}{\rho_0}\right)^2 + K \ Tr(\boldsymbol{\nabla}\mathbf{p})^2 + g(1-\mathbf{p}^2)^2 \right] \ , \tag{1.16}$$

$$\mathcal{F}_p(\{\mathbf{p}\}) = \int dxdyB\frac{\rho}{\rho_0}\boldsymbol{\nabla}\cdot\mathbf{p} \tag{1.17}$$

and ρ_0 is the equilibrium value of ρ.

The first term, $\mathcal{F}_n(\{\mathbf{p}\})$, is the usual free energy of a liquid crystal which contains only terms even in $\mathbf{p}$ [10], and the second term, $\mathcal{F}_p(\{\mathbf{p}\})$, contains additional terms that break this $\mathbf{p} \to -\mathbf{p}$ symmetry. K is the Frank constant in the one-constant approximation, and g controls the strength of polar order. The coherence length $\xi = \sqrt{K/2g}$ is the smallest relevant lengthscale and $|\vec{p}| \approx 1$ except within polar defect cores of size $a \sim \xi$.

Again, similar to the case of nematics, it is convenient to adopt the language of complex analysis. In terms of complex coordinates $z = x + iy$ and $\bar{z} = x - iy$, the complex partial derivatives $\partial = \partial_z = \frac{1}{2}(\partial_x - i\partial_y)$ and $\bar{\partial} = \partial_{\bar{z}} = \frac{1}{2}(\partial_x + i\partial_y)$, and the complex order parameter $p = p_x + ip_y$, the (dimensionless) free energy takes the form

$$\mathcal{F}(\{p\}) = \int dzd\bar{z} \left[4|\partial p|^2 + \epsilon^{-2}(1-|p|^2)^2\right] \ . \tag{1.18}$$

Since this is the same as the nematic case, then the analysis for the stationary defect solutions follow, except here we are limited to integral charge, instead of half-integral charge. Mathematically, this is because $\pi_1 S^1 = \mathbb{Z}$. For example, the director of a ± 1 defect rotates by $\pm 2\pi$ as it goes around a circle, so its charge is $\pm 2\pi/(2\pi) = \pm 1$. See Fig. 1.3 for a sketch.

It is also useful to talk about the geometric property. Defects have also a phase associated with them. For example, for a $+1$ defect, ϕ is the angle of $\mathbf{p}$ relative to the radial line. It is 0 for asters, $\pi/2$ for vortices, and for generic ϕ it s a spiral. (See also Fig. 1.3 for a sketch.) This orientation of the defect, a geometry property, will be important to us when we analyze defects in Chapter 5.

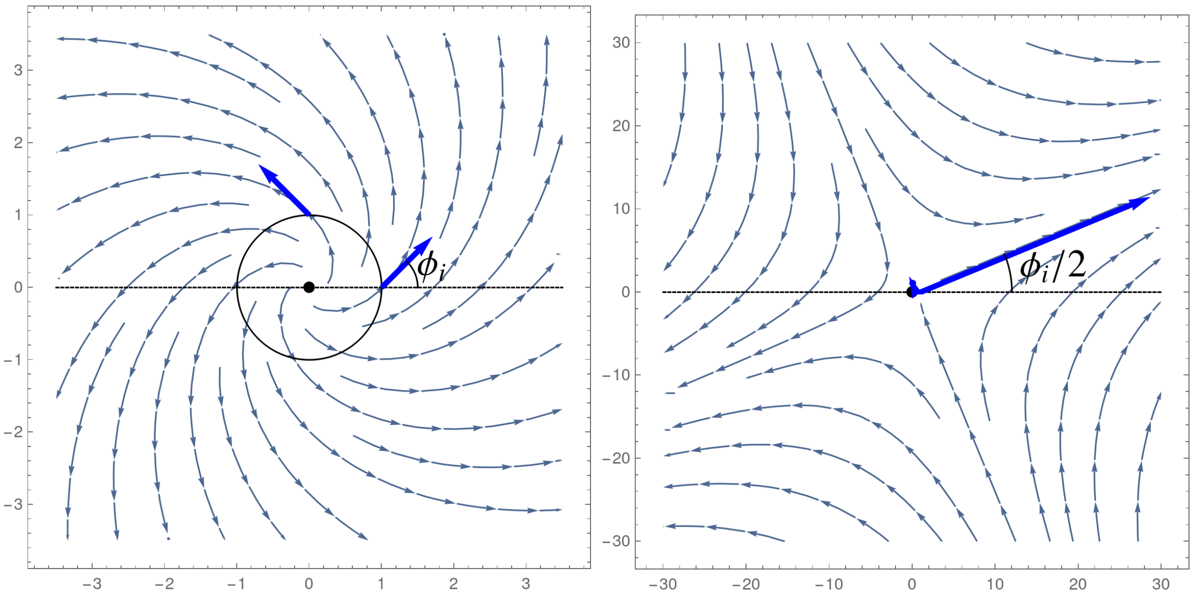

(a) +1 defect (b) −1 defect

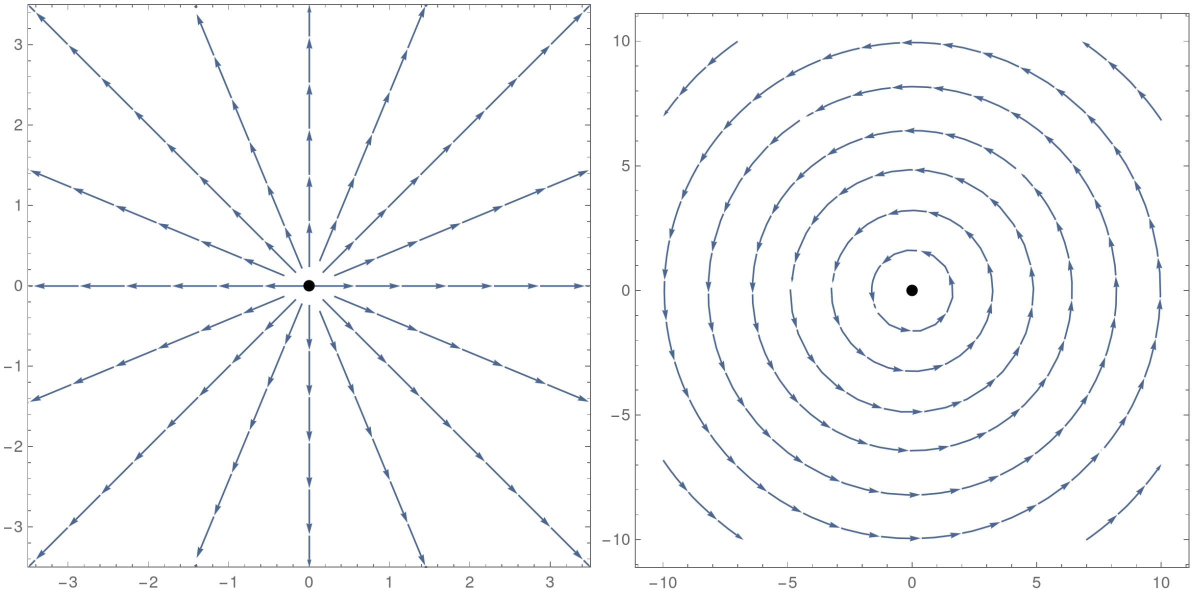

(c) aster (d) vortex

Figure 1.3: Sketches of single defect textures showing the angle ϕ_i (the phase of $\mathbf{p}$) for (a) a +1 defect where ϕ_i is the angle between P_i and $\hat{r}$, (b) a −1 defect where $\phi_i/2$ is the angle of the separatrix. Special values of ϕ_i are shown in (c) and (d) for a +1 defect: (c) is an aster ($\phi_i = 0$), and (d) is a vortex ($\phi_i = \pi/2$).

1.3 Morphogenesis

An important goal in developmental biology is understanding morphogenesis, which naturally benefits from an approach that incorporates mathematics and physics in addition to biology and chemistry. In 1917, D'Arcy Thompson advocated this approach in his monumental treatise, *On Growth and Form* [117]. Specifically, he argued that physical processes and mechanical forces are responsible for biological form.

In a different but related thread of thought, much research has focused on the way chemical patterns emerge during development [118], that is, via reaction-diffusion and positional information models. A few decades after D'Arcy, in 1952 Alan Turing introduced in *The Chemical Basis of Morphogenesis* the simple idea that biological-like patterns can spontaneously emerge from chemical reactions of diffusing molecules [119]. The set of equations describing pattern formation are now known as "reaction-diffusion equations," and he coined the term "morphogen" to describe such molecules responsible for pattern formation. A couple decades after Turing, in 1969 Lewis Wolpert introduced a complementary idea, positional information. In these models, cells determine their position because of the value of a morphogen specified by its gradient, and interpret this information to act accordingly.

However, both reaction–diffusion and positional information models lack mechanical processes (in particular feedback), which needs to be resolved since the three-dimensional shape is determined by mechanical processes. A complete theory requires at the minimum the integration of mechanical with biochemical processes. We are not the first to do this; for example, see [120, 121, 122, 123, 124, 125, 126, 127, 128] for reviews. In this thesis, we shall study morphogenesis using the lens of active matter, and in conjunction with geometrical ideas, a la D'Arcy.

However, given the myriad diversity of biology, is it possible to come up with a "grand unification theory" of morphogenesis? In fact, remarkably, the molecules involved in embryonic developmental, the molecular toolbox, are conserved among species [129, 130, 131]. This universality of the molecular toolbox encourages the study of theories whose universality classes would incorporate the important differences between species.

Philosophical considerations aside, on a more practical level, is this actually possible in connection to the real world? In plant tissues, where cells do not change their relative positions, there has been much progress in linking molecular and cellular processes to tissue formation [132, 133]. And in animal tissues, the ability to tag and track thousands of cells in space and time [134, 135, 136, 137, 138, 139] allow us to begin answering similar questions linking cellular processes to tissue shape [140, 141, 120, 121, 122, 123, 124, 125, 126, 127].

1.4 Thesis Overview

In the remainder of this dissertation, we will study the dynamics of active systems, both with nematic and polar orientational order. In particular, we will focus on the dynamics of topological defects as they play a key role in understanding the dynamics of the texture. We apply our results for defect dynamics to present a model of morphogenesis where the active topological defects drive the dynamics of the curved surface.

In Chapter 2, we show how fluctuations can induce both local nematic order and extensile stress. A key element of the model is the assumption that in the presence of local nematic alignment, cells preferentially crawl along the nematic axis, resulting in anisotropy of fluctuations. We demonstrate that activity can drive either extensile or contractile stresses in tissue, depending on the relative strength of the contractility of the cortical cytoskeleton and tractions by cells on the extracellular matrix.

With the establishment of the existence of both active stresses and local nematic order via the noise mechanism, in Chapter 3 we study the multi-defect dynamics of a nematic texture in the deep nematic limit. We show that the polarization of a defect, a geometric property, is not an independent degree of freedom, but it is directly determined by the position of all other defects. We find that interestingly, because of the non-orthogonality of textures associated with individual defects, their motion is coupled through a position dependent "collective mobility" matrix. In addition to the familiar active self-propulsion of the $+1/2$ defect, we identify new collective effects of activity that can be interpreted in terms of non-central and non-reciprocal interactions between defects. In Chapter 4, we consider various extensions such as allowing for the polarization to be dynamical, formulating the continuum model, and analyzing geometries such as finite disc and torus.

In Chapter 5, we apply the same analysis to a system with polar order and compare and contrast our results with the nematic case. Similar to the nematics case, we get non-central and non-reciprocal interactions, but in contrast, we find that the orientation dynamics of $+1$ defects are not locked to defect positions and relaxes to asters. Moreover, using a scaling argument, we explain the transient feature of active polar defects and show that in the steady state, active polar fluids are either devoid of defects or consist of a single aster. We argue that for contractile (extensile) active nematic systems, $+1$ vortices (asters) should emerge as bound states of a pair of $+1/2$ defects, which has been recently observed. Moreover, unlike the polar case, we show that for active nematics, a linear chain of equally spaced bound states of pairs of $+1/2$ defects can screen the activity term. A common feature in both models is the appearance of $+1$ defects (elementary in polar and composite in nematic) in the steady state.

Finally, in Chapter 6 we address the question of morphogenesis in the context of nematic systems using what we have learned in the previous chapters. We develop a minimal framework to study the dynamics of a curved surface drive by the nematic texture. Allowing the surface itself to evolve via relaxational dynamics leads to a correlation between the nematic defects and the cell density growth rate as well as the Gaussian curvature. Regions of large plus (negative) curvature and larger growth (reduction) in density is colocalized with plus (negative) defects. As an example, we apply this framework to two different systems: cultured murine neural progenitor cells (NPCs), and *Hydra.* For the example of NPCs, we find that cells accumulate at plus defects and form mounds, and that cells are depleted at minus defects. For *Hydra*, by modeling a tentacle as a bound $+1$ defect state surrounded by two $-1/2$ defects, we numerically show that activity stabilizes a bound $+1$ defect state by creating an incipient tentacle, while a bound $+1$ defect state surrounded by two $-1/2$ defects can create a stationary ring configuration of tentacles, consistent with observations.

1.5 Permissions and Attributions

1. The content of Chapter 2 is based upon a collaboration with Mark Bowick, Boris Shraiman, and M. Cristina Marchetti, which has previously appeared in *Soft Matter* [142].
2. The content of Chapter 3 is based upon a collaboration with Mark Bowick, M. Cristina Marchetti, and Boris Shraiman [100].
3. The content of Chapter 4 is independent work, with the exception of the content in Chapter 4.5.2, which is adapted from a collaboration with Mark Bowick, M. Cristina Marchetti, and Boris Shraiman [100].
4. The content of Chapter 5 is based on [143].
5. The content of Chapter 6 is based upon a collaboration with Lakshminarayanan Mahadevan [144].

Chapter 2

Fluctuations can induce local nematic order and extensile stress

2.1 Introduction

We saw in Chapter 1 that importantly, the direction of motion of the comet-like $+1/2$ defect is controlled by the sign of active stresses: extensile active stresses, as generated in cytoskeletal suspensions by cross-linking motor proteins or in living cells through division, drive the defect to move towards the head of the comet, while contractile stresses, as occurring for instance in the acto-myosin cytoskeleton, drive the defect to move towards the tail [92]. This behavior has been verified extensively in simulations [96]. A surprising experimental finding is that in almost all realizations of two-dimensional active nematics, the motion of the $+1/2$ defect suggests that extensile activity dominates. While in bacteria this has been clearly associated with cell division [145, 146], the origin of the extensile activity observed in layers of human bronchial epithelial cells [70], in Madin-Darby canine kidney (MDCK) cells [68], in stem cells [67], and in simulations [147] on times scales shorter than those associated with appreciable cell division has only recently been explored [148].

The dynamics of cells crawling on a substrate is generally driven by two types of active mechanisms: (i) internal active forces generated within a cell by myosin-driven cellular contractility and transmitted throughout the tissue via supracellular actin coordination, and (ii) traction forces between the tissue and the substrate that drive cell motility. Internal forces due to cellular contractility yield active stresses, but no net force, while tractions provide an external forcing of the tissue. A naive expectation is that contractile active stresses dominate the behavior of epithelial tissue, while active tractions provide the main contribution to cell dynamics in mesenchymal tissue. The relative role, though, of these two types of active processes remains to be quantified. Here we use a continuum model of an incompressible tissue on a substrate to examine the interplay between these two types of activity. We show that *fluctuating* traction forces advected by flow can generate both local nematic order and effective extensile stresses in an otherwise isotropic tissue. Essentially, polar active migration drives local cell alignment captured by a nematic order parameter. A key assumption of our model is that cells will preferentially move along the direction of local cell alignment, rather than transverse to it. This is incorporated in the model by coupling the noise that drives the fluctuating cell tractions to local nematic order. By working perturbatively in the noise strength, we show that the nonlinear advection of active tractions by cellular flow can be recast in the form of a mean active force that has the structure of an extensile stress and drives cell dynamics. Flow alignment generated by this active forcing in turn destabilizes the isotropic state, suggesting the onset of a state with spatially modulated texture and rotating director field. While the fact that extensile activity can build local nematic order in what would be an isotropic state in the passive limit has been highlighted before [149, 150, 151, 152], a new result of our model is that the extensile stress observed in crawling tissue may arise from fluctuating cellular tractions.

2.2 Model of Crawling Tissue

We describe the tissue at the continuum level as a contractile active gel [153] in terms of the cell density ρ, the flow velocity $\mathbf{v}$ and a nematic order parameter $\mathbf{Q} = (2\hat{\mathbf{n}}\hat{\mathbf{n}} - \mathbf{1})S$ that captures cell shape anisotropy and alignment of elongated cells, with S the magnitude of nematic order and $\hat{\mathbf{n}}$ the unit nematic director field that identifies the direction of local order. The tissue is in contact with a substrate and force balance requires that the force on a tissue element due to the surrounding cells be balanced by the traction force density $\mathbf{t}$ that the tissue exerts of the substrate, according to

$$\partial_j \sigma_{ij} - t_i = 0 \ , \tag{2.1}$$

where $\sigma_{ij} = -p\delta_{ij} + 2\eta S_{ij} + \sigma^a_{ij}$ is the tissue stress tensor, with p the pressure, η the tissue shear viscosity, $S_{ij} = \frac{1}{2}(\partial_i v_j + \partial_j v_i)$ the rate of strain tensor, and $\sigma^a_{ij} = \alpha_c Q_{ij}$ an active stress. The traction force is written as $\mathbf{t} = \Gamma \mathbf{v} - \mathbf{f}$, where Γ is the effective friction with the substrate and $\mathbf{f}$ a *fluctuating* propulsive force density caused by transiently polarized cryptic lamellipodia activity which underlies cell motility. This form for the traction $\mathbf{t}$ allows for local misalignment of cell propulsion and tissue velocity due to intracellular interactions, consistent with experimental findings [154, 155]. Assuming the tissue to be incompressible ($\boldsymbol{\nabla} \cdot \mathbf{v} = 0$, hence $\rho =$ constant), the dynamics is described by the following equations

$$\eta \nabla^2 \mathbf{v} - \boldsymbol{\nabla} p + \alpha_c \boldsymbol{\nabla} \cdot \mathbf{Q} = \Gamma \mathbf{v} - \mathbf{f} \ , \tag{2.2}$$

$$D_t \mathbf{Q} = \lambda \mathbf{S} - \frac{1}{\gamma} \left[\frac{\delta F(\mathbf{Q})}{\delta \mathbf{Q}} \right]^{ST} \ , \tag{2.3}$$

$$\left(\partial_t + \mathbf{v} \cdot \boldsymbol{\nabla} \right) \mathbf{f} = -\frac{\mathbf{f}}{\tau} + \boldsymbol{\xi} \ , \tag{2.4}$$

where $D_t = \partial_t + \mathbf{v} \cdot \boldsymbol{\nabla} - [\boldsymbol{\Omega}, \cdot]$ is the comoving and corotational derivative, with $\Omega_{ij} = \frac{1}{2}(\partial_i v_j - \partial_j v_i)$ the vorticity tensor, and the superscript ST in Eq. (2.3) denotes the symmetric traceless part of any tensor [33, 96]. Other couplings to flow gradient are generally allowed in Eq. (2.4) for f_i, such as $\Omega_{ij}f_j$ and $\lambda S_{ij}f_j$. These terms, however, do not contribute to the noise-renormalized mean propulsion force evaluated below and are therefore not included in the equation.

The Stokes equation, Eq. (2.2), includes two types of active processes. First, force dipoles due to the pulling action of myosins and transmitted across the epithelial tissue by cell-cell interactions mediated by E-cadherins result in an *apolar* contractile active stresses $\alpha_c\mathbf{Q}$ [102, 33, 153], with $\alpha_c > 0$ an activity parameter that incorporates the biochemical processes responsible for cellular contraction and controlled by myosin density and ATP concentration. Second, the presence of the substrate allows for *polar* terms described by the *fluctuating* propulsive force density $\mathbf{f}$. This may arise, for instance, from intermittent protrusions and retractions of cryptic lamellipodia at a rate controlled by cell-substrate interaction mediated by focal adhesion complexes. We assume that the traction force density $\mathbf{f}$ tends to align with the long axis of the cell that controls the direction of local nematic order, but switches direction on a time scale τ much shorter than the time scale τ_Q controlling the reorientation of the local nematic texture. As a result, there is no polar order of propulsive forces at the tissue scale. This separation of time scales allows us to treat this source of activity independently and examine how microscopic cell scale fluctuations feed back on the tissue-scale active stress. Finally, we have neglected in the Stokes equation elastic liquid crystalline stresses. These terms are of higher order in the gradients than the active stress and do not change the results described below.

The dynamics of the nematic order parameter is controlled by flow alignment driven by coupling to vorticity and rate of strain, with λ the flow alignment parameter, and relaxation controlled by the de Gennes-Ginzburg-Landau free energy [156, 157], $F = \frac{1}{2}\int_{\mathbf{x}} \{a\ Tr[\mathbf{Q}^2] + K(\boldsymbol{\nabla}\cdot\mathbf{Q})^2\}$, with K the nematic stiffness (in the one-elastic constant approximation) and γ the rotational friction of the nematic. We assume that the tissue is isotropic ($a > 0$), and hence neglect stabilizing terms of order $\mathcal{O}(\mathbf{Q}^4)$ in the free energy, so that

$$-\frac{1}{\gamma}\frac{\delta F(\mathbf{Q})}{\delta \mathbf{Q}} = -\frac{\mathbf{Q}}{\tau_Q} + D\nabla^2\mathbf{Q} \ , \tag{2.5}$$

with $\tau_Q = \gamma/a$ the relaxation time of the nematic texture and $D = K/\gamma$ a diffusivity.

The fluctuating local propulsive force $\mathbf{f}$ (Eq. (2.4)) persists over a time τ, and is then randomized by interactions with other cells and short scale active processes embodied by a zero mean random force $\boldsymbol{\xi}$, with correlations

$$\langle \xi_i(\mathbf{x},t)\xi_j(\mathbf{x}',t')\rangle = \varepsilon^2\delta(t-t')\delta(\mathbf{x}-\mathbf{x}')[\delta_{ij} + \kappa\langle Q_{ij}(\mathbf{x},t)\rangle] \ , \tag{2.6}$$

with $\kappa > 0$ and ε^2 the strength of the noise. The noise correlations are chosen to depend on $\mathbf{Q}$ so as to capture the fact that local alignment will result in different cell motility along and transverse to the director. The positive sign of κ favors motion along the director and penalizes displacements transverse to the direction of local order. We also assume that $\kappa S < 1$ to ensure that the variance of the noise is positive. Given $\tau \ll \tau_Q$, we then examine the behavior of the tissue on times long compared to τ, but in the presence of finite local nematic order. The separation of these two time scales in epithelial tissue is evidenced by the observation of negligible cell motility (corresponding to $\langle \mathbf{f} \rangle = 0$) and appreciable regions of local nematic order (corresponding to $\langle \mathbf{Q} \rangle \neq 0$).

To impose incompressibility we take the divergence of Eq. (2.2) to obtain $\nabla^2 p = \boldsymbol{\nabla}\cdot(\mathbf{f} + \alpha_c\boldsymbol{\nabla}\cdot\mathbf{Q})$. Eliminating the pressure, the Stokes equation can then be formally written as

$$\Gamma v_i - \eta\nabla^2 v_i = \mathcal{P}_{ij}\left(f_j + \alpha_c\partial_l Q_{jl}\right) \ , \tag{2.7}$$

with $\mathcal{P}_{ij} = (\delta_{ij} - \nabla^{-2}\partial_i\partial_j)$ being the incompressibility projection operator.

2.3 Noise induced extensile stress

To linear order, the only steady state solution of our noise-averaged equation is $\langle \mathbf{v} \rangle = \langle \mathbf{f} \rangle = \langle \mathbf{Q} \rangle = 0$. In this section we show, however, that noisy traction forces renormalize the flow velocity, inducing both nematic alignment and extensile active stresses.

Taking the Fourier transform in space and time, Eqs. (2.7) and (2.4) can be written as

$$v_i(\mathbf{k},\omega) = \frac{1}{\Gamma + \eta k^2}\left(\delta_{ij} - \hat{k}_i\hat{k}_j\right)\left[f_j(\mathbf{k},\omega) + \alpha_c i k_l Q_{jl}(\mathbf{k},\omega)\right] \ , \tag{2.8}$$

$$f_i(\mathbf{k},\omega) = \frac{\xi_i(\mathbf{k},\omega)}{\tau^{-1} + i\omega} - \frac{i}{\tau^{-1} + i\omega}\int_{\omega'}\int_{\mathbf{q}}(k_j - q_j)v_j(\mathbf{q},\omega')f_i(\mathbf{k} - q, \omega - \omega') \ , \tag{2.9}$$

where $\int_\omega = \int \frac{d\omega}{2\pi}$ and $\int_\mathbf{q} = \int \frac{d\mathbf{q}}{(2\pi)^2}$. Substituting Eq. (2.8) into Eq. (2.9) and averaging over noise gives

$$\langle f_i(\mathbf{k},\omega)\rangle = -\frac{i}{\tau^{-1} + i\omega}\int_{\omega'}\int_{\mathbf{q}}\frac{\delta_{j\ell} - \hat{q}_j\hat{q}_\ell}{\Gamma + \eta q^2}(k_j - q_j)\langle f_\ell(\mathbf{q},\omega')f_i(\mathbf{k} - q, \omega - \omega')\rangle \tag{2.10}$$

Here we have explicitly used the fact that due to the separation of time scales, we can treat $\mathbf{f}$ as uncorrelated with $\mathbf{Q}$. We now have to compute the two point force correlation $\langle f_\ell(\mathbf{q},\omega')f_i(\mathbf{k} - q, \omega - \omega')\rangle$. To first order in the noise amplitude, using Eq. (2.9) we have

$$\begin{aligned}\langle f_\ell(\mathbf{q},\omega')f_i(\mathbf{k} - q, \omega - \omega')\rangle &= \frac{1}{(\tau^{-1} + i\omega')(\tau^{-1} + i[\omega - \omega'])}\langle \xi_\ell(\mathbf{q},\omega')\xi_i(\mathbf{k} - q, \omega - \omega')\rangle \\ &= \frac{\varepsilon^2}{(\tau^{-1} + i\omega')(\tau^{-1} + i[\omega - \omega'])}\left[\delta(\mathbf{k})\delta(\omega)\delta_{\ell i} + \kappa\langle Q_{\ell i}(\mathbf{k},\omega)\rangle\right]\end{aligned} \tag{2.11}$$

where in the 2nd line we computed the Fourier transform of Eq. (2.6). Substituting into Eq. (2.10) leads to

$$\langle f_i(\mathbf{k},\omega)\rangle = -\frac{i\varepsilon^2\kappa k_j\langle Q_{\ell i}(\mathbf{k},\omega)\rangle}{\tau^{-1} + i\omega}\int_{\omega'}\frac{1}{(\tau^{-1} + i\omega')(\tau^{-1} + i[\omega - \omega'])}\int_{\mathbf{q}}\frac{\delta_{j\ell} - \hat{q}_j\hat{q}_\ell}{\Gamma + \eta q^2} \tag{2.12}$$

Exploiting the fact that the two integrals decouple, we calculate the renormalization of the traction force to first order in the noise amplitude, with the result

$$\langle f_i(\mathbf{k},\omega)\rangle = -\frac{\varepsilon^2\kappa\ln(\ell_v/a)}{4\pi\eta}\frac{ik_j\langle Q_{ij}(\mathbf{k},\omega)\rangle}{(\tau^{-1}+i\omega)(2\tau^{-1}+i\omega)} \ , \tag{2.13}$$

where we have used

$$\int_{\omega'}\frac{1}{(\tau^{-1}+i\omega')(\tau^{-1}+i[\omega-\omega'])} = \frac{1}{2\tau^{-1}+i\omega} \tag{2.14}$$

$$\int_{\mathbf{q}}\frac{\delta_{j\ell}-\hat{q}_j\hat{q}_\ell}{\Gamma+\eta q^2} = \frac{\delta_{j\ell}}{8\pi\eta}\ln\left(1+\frac{\ell_v^2}{a^2}\right) \approx \frac{\delta_{j\ell}}{4\pi\eta}\ln\left(\frac{\ell_v}{a}\right) \ , \tag{2.15}$$

with $\ell_v = \sqrt{\eta/\Gamma}$ the viscous screening length and a a short scale cutoff of the order of the cell size.

Since we are interested in time $t \gg \tau$, with $\tau \ll \tau_Q$, we can neglect ω in the denominator of Eq. (2.13). Taking the inverse Fourier transform yields a mean force

$$\langle \mathbf{f}\rangle = \alpha_f \boldsymbol{\nabla}\cdot\langle \mathbf{Q}\rangle \ , \tag{2.16}$$

where

$$\alpha_f = -\frac{\varepsilon^2\kappa\tau^2}{8\pi\eta}\ln\left(\frac{\ell_v}{a}\right) < 0 \tag{2.17}$$

is an extensile activity. Extensile stresses arise because persistent cell tractions $\mathbf{f}$ along the direction of local nematic order tends to elongate local regions of the tissue in that direction. This effect is transient (only lasts a short time τ), but due to the nonlinearity of the advection term in the $\mathbf{f}$ equation it leads to a nonzero value of $\langle \mathbf{f}\rangle$ that corresponds to extensile stresses. This is seen by writing $\partial_t f_i \sim -(\mathbf{v}\cdot\boldsymbol{\nabla})f_i \sim -(f_j\nabla_j)f_i$, and so $\langle f_i\rangle \sim -\langle \tau(f_j\nabla_j)f_i\rangle \sim -(...)\nabla_j\langle Q_{ij}\rangle$.

We now return to Eqs. (2.7) and (2.3), average over noise, and use Eq. (2.16) to eliminate the mean traction force. The linear dynamics of fluctuations from the quiescent disordered state with $\langle \mathbf{v} \rangle = \langle \mathbf{Q} \rangle = 0$ is then governed by the equations

$$\Gamma \langle v_i \rangle - \eta \nabla^2 \langle v_i \rangle = \alpha \mathcal{P}_{ij} \partial_l \langle Q_{jl} \rangle \ , \tag{2.18}$$

$$\partial_t \langle Q_{ij} \rangle = \frac{\lambda}{2} \left(\partial_i \langle v_j \rangle + \partial_j \langle v_i \rangle \right) - \frac{\langle Q_{ij} \rangle}{\tau_Q} + D \nabla^2 \langle Q_{ij} \rangle \ , \tag{2.19}$$

where

$$\alpha = \alpha_c + \alpha_f \tag{2.20}$$

is the total activity, with sign controlled by the interplay of contractile activity ($\alpha_c > 0$) from actomyosin contractility and extensile activity ($\alpha_f < 0$) from fluctuating propulsive forces.

2.4 An equivalent model with white noise

Something that may be unsatisfactory about the model above is that we assumed that the noise is not white noise, but rather is correlated with the nematic tensor. It is natural to ask whether we can construct a model where the noise is white. We now show that indeed there is such a model.

The same noise-renormalization of the mean force (Eq. (2.16)) can be obtained by considering a related model. In this model, we explicitly include an alignment term $Q_{ij}f_j$ in the dynamics of $\mathbf{f}$, that is,

$$(\partial_t + \mathbf{v}\cdot\boldsymbol{\nabla})f_i = -\tau^{-1}f_i + \zeta Q_{ij}f_j + \tilde{\xi}_i, \tag{2.21}$$

with $\zeta > 0$ and where $\tilde{\xi}$ is Gaussian white noise, with zero mean and correlations

$$\langle \tilde{\xi}_i(x,t)\tilde{\xi}_j(x',t')\rangle = \varepsilon^2\delta(t-t')\delta(x-x')\delta_{ij}. \tag{2.22}$$

For stability, we will need to assume that $\zeta\tau < 1$, and here the noise is isotropic and has no preferred direction, unlike the model we studied in Chapter 2.3.

We now will show that we can derive $\langle \mathbf{ff}\rangle$ (Eq. (2.11)), essentially justifying the choice of noise correlation in Eq. (2.6). To leading order in noise amplitude,

$$\partial_t f_i = -\tau^{-1}f_i + \zeta Q_{ij}f_j + \tilde{\xi}_i \tag{2.23}$$

We have dropped the advection term here since it is 2nd order. Taking the Fourier transform in space and time leads to

$$f_i(\mathbf{k},\omega) = [i\omega + \tau^{-1} - \zeta Q]^{-1}_{ij}\tilde{\xi}_j(\mathbf{k},\omega) \tag{2.24}$$

Here we have explicitly used the fact that due to separation of length and time scales, we can effectively treat $\mathbf{Q}$ as constant.

Similar to before, computing the correlation gives

$$\langle f_\ell(\mathbf{q},\omega')f_i(\mathbf{k}-q,\omega-\omega')\rangle = \varepsilon^2[\tau^{-1}+i\omega'-\zeta\langle\mathbf{Q}\rangle]^{-1}_{\ell m}[\tau^{-1}+i(\omega-\omega')-\zeta\langle\mathbf{Q}\rangle]^{-1}_{ij}\delta(\mathbf{k})\delta(\omega)\delta_{mj} \tag{2.25}$$

To leading order in $\tau\zeta$, we finally arrive at

$$\langle f_\ell(\mathbf{q},\omega')f_i(\mathbf{k}-q,\omega-\omega')\rangle = \frac{\varepsilon^2}{(\tau^{-1}+i\omega')(\tau^{-1}+i[\omega-\omega'])}[\delta(\mathbf{k})\delta(\omega)\delta_{\ell i}+2\tau\zeta\langle Q_{\ell i}(\mathbf{k},\omega)\rangle] \tag{2.26}$$

We have thus recovered Eq. (2.11) for $\kappa = 2\zeta\tau \ll 1$.

2.5 Noise induced nematic order

We next demonstrate that extensile stresses from fluctuating tractions also build up local nematic order, justifying our choice of an anisotropic noise correlator. Taking the spatial Fourier transform of Eqs. (2.18) and (2.19) and eliminating the velocity in favor of the alignment tensor, we obtain a closed equation for $\langle Q_{ij}(\mathbf{k},t)\rangle$, similar to [149, 150]:

$$\begin{aligned}\partial_t\langle Q_{ij}\rangle = &-\left(\tau_Q^{-1}+Dk^2\right)\langle Q_{ij}\rangle\ ,\\ &+\frac{\alpha\lambda}{2(\Gamma+\eta k^2)}\left[-k_i k_l\langle Q_{jl}\rangle - k_j k_l \langle Q_{il}\rangle + 2k_i k_j \Psi^{\parallel}\right]\ ,\end{aligned} \tag{2.27}$$

where $\Psi^{\parallel}=\hat{k}_i\hat{k}_j\langle Q_{ij}\rangle$. Upon contraction of Eq. (2.27) with $\hat{k}_i\hat{k}_j$ and $\epsilon_{is}\hat{k}_s\hat{k}_j$, the longitudinal mode $\Psi^{\parallel}$ and the transverse mode $\Psi^{\perp}=\epsilon_{is}\hat{k}_s\hat{k}_j\langle Q_{ij}\rangle$ decouple, giving

$$\partial_t\Psi^{\parallel}(\mathbf{k},t) = -\left(\tau_Q^{-1}+Dk^2\right)\Psi^{\parallel}(\mathbf{k},t)\ , \tag{2.28}$$

$$\partial_t\Psi^{\perp}(\mathbf{k},t) = -\left[\tau_Q^{-1}+Dk^2+\frac{\alpha\lambda k^2/\Gamma}{1+\ell_v^2k^2}\right]\Psi^{\perp}(\mathbf{k},t)\ . \tag{2.29}$$

The decoupling of longitudinal and transverse modes follows from isotropy. Clearly $\Psi^{\parallel}$ is always stable as $\Psi^{\parallel}>0$. On the other hand, the mode controlling the decay of $\Psi^{\perp}$ can change sign if $\alpha<0$, corresponding to the case where extensile activity exceeds contractile activity. The homogeneous isotropic state becomes unstable for $\alpha<-\alpha^*$, with

$$\alpha^*=\frac{\Gamma D}{\lambda}\left(1+\sqrt{\frac{\eta}{\Gamma D\tau_Q}}\right)^2\ . \tag{2.30}$$

The fact that $\Psi^{\parallel}$ is stable while $\Psi^{\perp}$ can be unstable is not surprising. In Eq. (2.18), the incompressibility projection operator eliminates the component of $\mathbf{v}$ in the direction of $\boldsymbol{\nabla}\cdot\mathbf{Q}$ in Fourier space. Thus the active stress does not affect the longitudinal mode, but it can modify the behavior of the transverse mode, as we saw above.

This linear instability discussed here for the case of rod-like ($\lambda>0$) extensile ($\alpha<0$) active entities also occurs for disc-like ($\lambda<0$) contractile ($\alpha>0$) systems, similar to

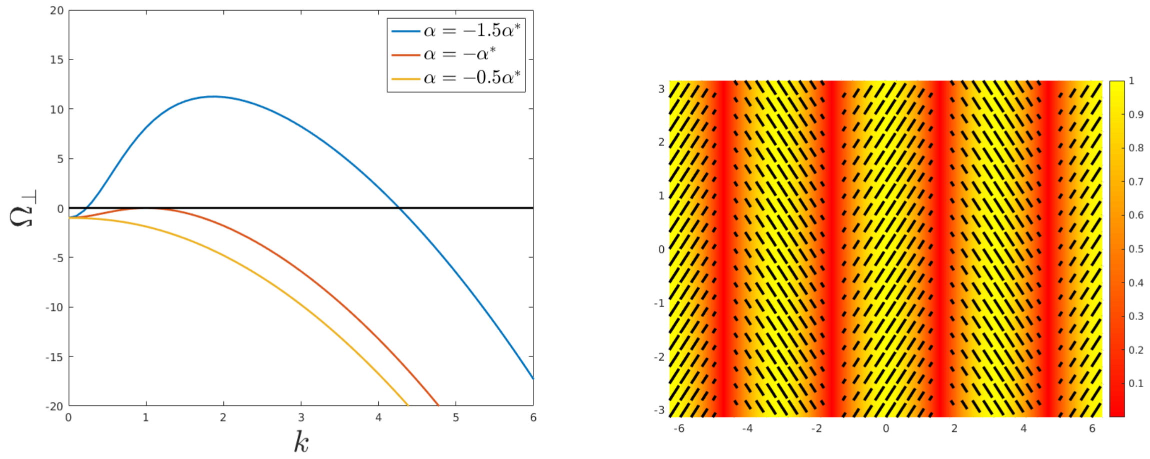

Figure 2.1: Left: the dispersion relation of the growth rate $\Omega_\perp$ (Eq. (2.31)) as a function of the wavenumber k for three values of activity: $\alpha = -0.5\alpha^*, \alpha = -\alpha^*$, and $\alpha = -1.5\alpha^*$. At the onset of instability for $|\alpha| = \alpha^*$, only the mode $k = k_0$ is unstable. Above the transition, the unstable modes lie in a $k_- < k < k_+$. Right: sketch of the nematic texture corresponding to the unstable mode with $\mathbf{k} = k_0\hat{\mathbf{x}}$ for $\phi = 0$. The length of the segments, as well as the color, is proportional to the strength of nematic order S. The angle between the director and the wavevector $\mathbf{k}$ is $\pm\pi/4$.

the effect noted in a different context in Ref. [158]. It is best discussed in terms of three length scales that control the dynamics of our model of cellular active nematics: (i) the viscous length ℓ_v, (ii) the nematic correlation length $\xi = \sqrt{D\tau_Q}$, and (iii) an active length $\ell_a = \sqrt{|\alpha|\lambda\tau_Q/\Gamma}$ that balances flows induced by active stresses against frictional dissipation [1]. In terms of these length scales, the dispersion relation of the mode controlling the dynamics of $\Psi^\perp$ is given by

$$\Omega_\perp = -\tau_Q^{-1}\left[1 + \xi^2 k^2 + \mathrm{sgn}(\alpha)\frac{\ell_\mathrm{a}^2\mathrm{k}^2}{1 + \ell_\mathrm{v}^2\mathrm{k}^2}\right] . \tag{2.31}$$

This mode becomes unstable ($\Omega_\perp > 0$) for extensile systems ($\alpha < 0$) of elongated

---

[1] The active length defined here is distinct from the one commonly used in the literature, $\ell_{active} = \sqrt{K/|\alpha|}$, which controls the dynamics of active nematics in the absence of substrate friction [96, 159].

particles ($\lambda > 0$) provided

$$\ell_a > \xi + \ell_v \ . \tag{2.32}$$

The dispersion relation for a few values of parameters is shown in Fig. 2.1. The wavevector of the fastest growing mode is $k_0 = \frac{1}{\ell_v}\left(\frac{\ell_a}{\xi} - 1\right)^{1/2}$, and the instability occurs in a band of wavevectors given by

$$k_\pm^2(\alpha) = \frac{\ell_a^2 - \xi^2 - \ell_v^2 \pm \sqrt{(\ell_a^2 - \xi^2 - \ell_v^2)^2 - 4\xi^2\ell_v^2}}{2\xi^2\ell_v^2} \ , \tag{2.33}$$

with $k_\pm(|\alpha| = \alpha^*) = k_0$. We can understand heuristically why there is a band: at small wavenumber, the active stress is small, and at large wavevnumber, the finite viscosity dampens or suppresses the instability.

The instability of the disordered state indicates that in extensile systems of elongated units, active flows build up local nematic order, as previously demonstrated for compressible nematics [149, 150]. Note that a finite viscosity is required to stabilize the system at short scales. The instability corresponds to growth of $\Psi^\perp$, and the associated nematic texture is obtained as solution of $\hat{k}_i\hat{k}_j\langle\tilde{Q}_{ij}\rangle = 0$. The component of the texture corresponding to wavevector $\mathbf{k}$ is then given by

$$Q_{ij}(\mathbf{x}) = A\cos(\mathbf{k}\cdot\mathbf{x} + \phi)(\epsilon_{i\ell}\hat{k}_\ell\hat{k}_j + \epsilon_{j\ell}\hat{k}_\ell\hat{k}_i) \ , \tag{2.34}$$

where we have explicitly included the Fourier factor $\cos(\mathbf{k}\cdot\mathbf{x} + \phi)$. This can be written in terms of a unit nematic director field $\hat{\mathbf{n}}$ as $\mathbf{Q} = (2\hat{\mathbf{n}}\hat{\mathbf{n}} - \mathbf{1})S$, where $\hat{\mathbf{n}}$ is the eigenvector of the largest eigenvalue of the matrix texture given in Eq. (2.34),

$$\hat{n}_i = \frac{1}{\sqrt{2}}[\delta_{ij} - \mathrm{sgn}[\cos(\mathbf{k}\cdot\mathbf{x} + \phi)]\mathrm{\epsilon_{ij}}]\hat{\mathrm{k}}_\mathrm{j} \ . \tag{2.35}$$

This satisfies $\cos(\hat{\mathbf{k}}\cdot\hat{\mathbf{n}}) = 1/\sqrt{2}$ and so $\hat{\mathbf{n}}$ is at an angle $\pm\pi/4$ to $\mathbf{k}$. A sketch of $\hat{\mathbf{n}}$ for the mode $\mathbf{k} = k_0\hat{\mathbf{x}}$ with amplitude modulated by $A|\cos(k_0x + \phi)|$ is shown in Fig. 2.1. It corresponds to a modulated chevron texture of periodicity $2\pi/k_0$, with alternating nematic domains tilted at 90° to each other, separated by thin isotropic bands. The structure is analogous to that obtained in certain passive nematic liquid crystals under shear [160, 161] and in lamellar phases of diblock copolymers [162].

2.6 Discussion

Using a mesoscopic model for a tissue layer, we have shown that fluctuations in the traction forces exerted by cells on the substrate can build up local nematic order in the tissue and lead to extensile active stresses that compete with those arising from actomyosin contractility. The sign of the net activity, $\alpha = \alpha_c + \alpha_f$, with $\alpha_c > 0$ controlled by contractile actomyosin forces and $\alpha_f < 0$ (given in Eq. (2.17)) determined by the interplay of single-cell motility and global tissue flow, is determined by the larger of these two contributions. The tissue dynamics may exhibit overall contractile or extensile behavior depending on the relative magnitude of these two contributions to the active stress. In confluent tissues with strong extracellular actin fibers capable of transmitting stresses across cells, we expect a dominance of actomyosin contractility. In mesenchymal tissue, in contrast, local tractions may dominate and mediate the build-up of local nematic order, with associated extensile dynamics of topological defects. Other mechanisms not directly considered here may also enable force transmission across the tissue. In particular, passive cell-cell adhesion provides intercellular couplings which enable one cell to *pull* another. Some of these effects are encoded in the tissue shear viscosity η. Finally, although here we have assumed incompressibility, which results in cells pushing on each other, finite compressibility may arise in epithelial cells due, for instance, to deformation of the nucleus or from apical surface tension. The role of the resulting density fluctuations remains to be explored.

Chapter 3

Multi-defect Dynamics in Active Nematics

3.1 Introduction

In Chapter 2, we saw explicitly how we can generate both local nematic order and effective extensile stresses, the mechanism being fluctuating traction forces advected by flow. With the establishment of nematic order and active stresses, we now study active nematic systems.

When active forces are sufficiently high, active nematics exhibit spatio-temporally chaotic self-sustained flows that have been dubbed “active turbulence”, where vortical flows are accompanied by the proliferation of topological defects in the nematic texture [92, 93, 94, 95]. The relevant nematic defects are $\pm 1/2$ disclinations, that are created and annihilated in opposite sign pairs, with the resulting average defect density increasing with activity [96]. Defects have also been identified in biological systems, where they have been associated with cell extrusion [68, 67], changes in cell density [61] and morphogenetic processes [72].

Previous theoretical work has made progress in formulating a description of "turbulent" active nematics by focusing on the dynamics of the topological defects as quasi-particles, with effective active interactions mediated by elastic distortions of the nematic texture and by active flows [92, 85, 98, 99]. This chapter highlights the importance of the anisotropy of nematic disclinations [163, 164], and in particular the role of the polarity of the $+1/2$ defect by describing it as an effective active particle, with propulsive forces [75, 84, 92, 97] and aligning torques [98, 99] determined by the active flows. Experiments and simulations of continuum active nematic hydrodynamics have suggested that active defects themselves exhibit emergent behavior and order in states with orientational order of defect polarity [165, 150, 149, 166, 167, 168, 169]. In spite of recent progress, the nature of this emergent behavior and its relevance to specific experimental situations remains largely not understood.

Much of the earlier work had focused on the limit where the distortions of the texture due to different defects can be treated as independent, an assumption that is at odds with the long-range nature of nematic elasticity. An important open question is the role of multi-defect interactions in governing the defect dynamics. To that end, Ref. [170] obtained explicit solutions of the linearized equations determining quasi-static textures for neutral defect pairs and used them to describe defect pair-creation and annihilation. Generalization of the methods to multi-defect states is, however, cumbersome.

In this chapter, we begin with the familiar hydrodynamic equations of a compressible active nematic film on a substrate and proceed by writing down the explicit quasistatic solution for a multi-defect nematic texture fully parameterized by arbitrary position of N defect cores. This forms a $2N$ dimensional "inertial manifold" on which slow dynamics associated with defect motion unfolds. To derive general equations for the defect dynamics driven by activity, we consider a system deep in the nematic state and take advantage of the variational principle. Our analysis transforms the partial differential equations of active nematic hydrodynamics into a set of ordinary differential equations for the defect positions that fully incorporates multi-defect interactions and yields a number of new results. First we show that, even in the passive limit, the overdamped dynamics of defects as quasiparticles is governed by a non-diagonal mobility matrix that captures the fact that because of the overlap of the textures associated with different defects, motion of one defect effectively "drags" the other defects, the source of the apparent non-locality being the long-range nature of elastic interactions in the nematic state. While the off-diagonal terms of the mobility matrix are small compared to the diagonal ones (that reduce to the well known defect friction [171]), the off-diagonal terms fall off only logarithmically with interdefect distance. Activity renders the $+1/2$ defect self propelled along its axis, as shown earlier [75, 84, 92, 97]. It additionally generates new active forces among defects that are qualitatively different from the well-known Coulomb interactions among defect charges. We also show that the forces on defects due to the active flow generated by all others are in general non-central and non-reciprocal, and are controlled by multi-defect dynamics. Previous work [98] had obtained the effective dynamics of individual defects in the mean-field of other defects, and in this approach, the orientation or polarization of the $+1/2$ defect was treated as an independent degree of freedom. Here, in contrast, we describe directly the dynamics of multi-defect textures without the need for the mean-field approximation. We show that in the deep nematic limit the polarization of a defect is not an independent degree of freedom, but rather it is directly determined by the position of all other defects, which we support by simulations. This provides a complete description of multi-defect dynamics, but yields defect-defect interactions that are intrinsically determined by the dynamics of all of the defects. Finally, this chapter makes explicit the non-reciprocal and non-central nature of the interaction between defects.

3.2 The Model

We consider a two-dimensional nematic liquid crystal described by the the Landau-de Gennes (LdG) free energy [5], $\mathcal{F}(\{\mathbf{Q}\})$,

$$\mathcal{F}(\{\mathbf{Q}\}) = \frac{1}{2}\int dxdy \left[K\ Tr(\boldsymbol{\nabla}\mathbf{Q})^2 + g[1 - 2Tr(\mathbf{Q}^2)]^2\right]\ , \tag{3.1}$$

with $2D$ traceless tensor order parameter of the form

$$Q_{ab} = A[\hat{n}_a\hat{n}_b - \frac{1}{2}\delta_{ab}] \tag{3.2}$$

expressed in terms of the position dependent director field $\hat{\mathbf{n}}$. The rigidity parameter, K, defines the energetic cost of spatial variation of $\mathbf{Q}$ (for simplicity we shall consider the single Frank constant approximation) and g, with units of energy density, controls the strength of nematic order, via the coherence length $\xi = \sqrt{K/2g}$ controls spatial variations in the magnitude of the order parameter A. Below we assume to be deep in the nematic state ($g \to \infty$), where ξ is smaller than all other relevant lengthscales. In this limit $A \approx 1$ and the magnitude of the order parameter $Tr(\mathbf{Q})^2 \approx 1/2$ *almost* everywhere, exceptions being the cores of nematic defects of size $\sim \xi$.

The dynamics of a nematic is controlled by the balance of relaxation towards the minimum of the LdG free energy and advection of the tensorial order parameter by flow $\mathbf{v}$, according to

$$\partial_t Q_{ab} + \mathbf{v}\cdot\boldsymbol{\nabla}Q_{ab} = \frac{1}{2}[\mathbf{Q},\boldsymbol{\omega}]_{ab} - \frac{D}{4K}\frac{\delta\mathcal{F}}{\delta Q_{ab}}\ , \tag{3.3}$$

where the diffusivity D governs relaxation towards equilibrium and $\omega_{ab} = \partial_a v_b - \partial_b v_a$ is the vorticity. In an *active* nematic, flow is generated spontaneously by local extensile (or contractile) activity described by the active stress tensor proportional to the order parameter $\sigma_{ab} = \tilde{\alpha}Q_{ab}$ [33, 102]. Here $\tilde{\alpha}$, with units of energy density, measures the strength of the activity, with $\tilde{\alpha} > 0$ ($\tilde{\alpha} < 0$) corresponding to contractile (extensile) activity. Assuming that flow is generated solely by the texture-dependent active force balanced by substrate friction μ, the flow velocity $\mathbf{v}$ is determined by the force balance equation, given by

$$\mu v_a = \tilde{\alpha}\partial_b Q_{ab} \ . \tag{3.4}$$

In Eq. (3.3) we have dropped the rate of strain alignment source term [33], because in $2D$ and in the friction dominated, overdamped limit described by Eq. (3.4), its effect on dynamics can be represented by renormalizing the rigidity constant [149, 150].

We rescale time with $\tau = \ell^2/D$, where ℓ stands for the characteristic separation between topological defects that are generated by activity [84, 92, 93]. We restrict ourselves here to the case where this length is much larger than the coherence length ξ, hence the density of defects is low. We also rescale all length with ℓ. Deep in the nematic regime where ξ is very small compared to all other relevant length-scales, we define $\epsilon = \xi/\ell \ll 1$. Finally, we also define the dimensionless activity parameter $\alpha = \tilde{\alpha}/4\mu D$.

Because our approach will be entirely based on complex analysis, we introduce it from the outset by defining the complex positional coordinates $z = x + iy$ and $\bar{z} = x - iy$ and the complex order parameter [103, 10]

$$Q = (Q_{xx} - Q_{yy}) + i2Q_{xy} = Ae^{i\theta} \tag{3.5}$$

in terms of which the (dimensionless) LdG free energy has the form

$$\mathcal{F}(\{Q\}) = \int dz d\bar{z} \left[4|\partial Q|^2 + \epsilon^{-2}(1 - |Q|^2)^2\right] \ , \tag{3.6}$$

where $\partial = \partial_z = \frac{1}{2}[\partial_x - i\partial_y]$ (and $\bar{\partial} = \partial_{\bar{z}} = \frac{1}{2}[\partial_x + i\partial_y]$).

In the complexified and rescaled form, $v = \alpha\partial Q$ and the dynamical equation is recast as

$$\partial_t Q = \mathcal{I}(Q) = -\frac{\delta\mathcal{F}(\{Q\})}{\delta\bar{Q}} + \alpha\mathcal{I}_\alpha(Q) \ , \tag{3.7}$$

where

$$\mathcal{I}_a(Q) = -(\partial Q \partial Q + \bar{\partial}\bar{Q}\bar{\partial}Q) + (\partial^2 Q - \bar{\partial}^2 \bar{Q})Q \tag{3.8}$$

represents the active drive obtained by eliminating the flow velocity in favor of Q. The 1st and the 2nd terms describe, respectively, the advection of the order parameter and its rotation by the vorticity.

3.3 Stationary and quasi-stationary textures deep in the nematic state

Stationary textures in the limit of zero activity ($\alpha = 0$) minimize the LdG free energy and hence solve [10, 104]

$$\frac{\delta \mathcal{F}}{\delta \bar{Q}} = -4\bar{\partial}\partial Q - 2\epsilon^{-2}(1 - |Q|^2)Q = 0 \, , \tag{3.9}$$

the imaginary and the real part of which read, respectively,

$$\bar{\partial}\partial\theta + \bar{\partial}\log A \; \partial\theta + \partial \log A \; \bar{\partial}\theta = 0 \tag{3.10}$$

and

$$A^2 = 1 - 2\epsilon^2 \left[(\partial\theta)^2 - A^{-1}\bar{\partial}\partial A \right] \, . \tag{3.11}$$

Deep in the nematic state ($\epsilon \to 0$) and away from possible singularities, Eqs. (3.10) and (3.11) are approximately

$$\bar{\partial}\partial\theta = 0 + \mathcal{O}(\epsilon^2) \tag{3.12}$$

and

$$A^2 = 1 - 2\epsilon^2(\partial\theta)^2 + \mathcal{O}(\epsilon^4) \, . \tag{3.13}$$

Thus, to leading order in ϵ, interesting nematic textures correspond to non-trivial solutions of the Laplace equation $\bar{\partial}\partial\theta = 0$. While there are no non-constant harmonic functions on the plane (that are bounded at infinity), such functions exists on a punctured plane and define the "topological defect" solutions. The simplest solution, as reviewed in Chapter 1, has the form $\theta = i\sigma \log(\frac{\bar{z}}{z})$, with $\sigma = \pm\frac{1}{2}$ corresponding to the well known $2D$ nematic charge of $\pm 1/2$ disclinations, corresponding to

$$Q = \psi(z, \bar{z}) = A_c(|z|) \left(\frac{z}{\bar{z}} \right)^{\sigma} \, , \tag{3.14}$$

with the amplitude $A_c(|z|)$ describing the defect core [104]: $A_c(0) = 0$ and $A_c(|z|) \approx 1$ for $|z| > a$, where $a \sim \mathcal{O}(\epsilon)$. More generally, one can construct a multi-defect texture Q_0, starting with a harmonic function on a plane punctured at points z_i labeling the defect positions, as

$$Q_0 = e^{i2\psi} \prod_i \psi_i \tag{3.15}$$

where

$$\psi_i = A_i \left(\frac{z - z_i}{\bar{z} - \bar{z}_i} \right)^{\sigma_i} \tag{3.16}$$

is a single-defect texture satisfying Eq. (3.9) with α_i the charge of defect i. The amplitude A_i is defined to be

$$A_i = A(|z - z_i|) \ , \tag{3.17}$$

where A is a solution to Eq. 1.8. We assume that defects are separated by distances ℓ much larger than the core size $|z_i - z_j| \gg \epsilon$, in which case $|Q_0| \approx 1$ almost everywhere.

With the proviso of "charge neutrality" $\sum_i \sigma_i = 0$, this texture satisfies a fixed boundary condition $Q_0 \to e^{i2\psi}$ as $|z| \to \infty$. More generally, if $\sum_i \sigma_i \neq 0$, then this texture satisfies a boundary condition $Q_0 \to e^{i\varphi \sum_i \sigma_i} e^{i2\psi}$ as $|z| \to \infty$, where φ is the polar azimuthal angle.

Before proceeding with the analysis, we note that in the vicinity of a defect, e.g. $z \approx z_i$, we can write

$$Q_0(z, \bar{z}) \approx e^{i\phi_i} \psi_i \ . \tag{3.18}$$

In other words, the texture reduces to the isolated defect form, with a phase factor that depends on the positions of all defects (and the boundary condition at infinity)

$$e^{i\phi_i} = e^{i2\psi} \prod_{j \neq i} \left(\frac{z_i - z_j}{\bar{z}_i - \bar{z}_j} \right)^{\sigma_j} \ . \tag{3.19}$$

This phase factor will play an important role in controlling the active dynamics of defects. It also readily interpreted in terms of the geometry of the director field close to the disclination, which exhibits one $(+1/2)$ or three $(-1/2)$ separatrix lines emerging radially from the core, as shown in Fig. 3.1. The separatrix is defined by the condition that the director points radially away from the core, which means that the polar angle of the director $\frac{1}{2}\arg Q_0|_{z\to z_i} = \varphi + \pi k$. Since the director angle in the vicinity of z_i is $\frac{1}{2}\arg Q_0 = \sigma_i\varphi + \frac{1}{2}\phi_i$ where $\varphi = \arg(z - z_i)$, we can express the angle of the separatrix, Φ_i, in terms of ϕ_i via $\Phi_i = (\phi_i + 2\pi k)/(2 - 2\sigma_i)$ which takes a unique value $\Phi_i = \phi_i$ for a plus disclination and three values $\Phi_i^{(k)} = \phi_i/3 + 2\pi k/3$ (with $k = 0, \pm 1$) for a minus disclination.

We note that for a global rotation, under which $\varphi \to \varphi + \eta$ and $\psi \to \psi + \eta$, the complex order parameter transforms as $Q_0 \to Q_0 e^{i2\eta}$, with the phase factor arising from the transformation of ψ. It follows that "defect phases" ϕ_i transform in a way that depends on the associated charge $\phi_i \to \phi_i + 2(1 - \sigma_i)\eta$. In contrast, the phases $\Phi_i = \phi_i/(2 - 2\sigma_i)$ transform naturally (i.e., shift by the rotation angle η) under rotation.

We can now compute the free energy using Q_0. The free energy $\mathcal{F}_0 = \mathcal{F}(Q_0)$ can be written in terms of the defect positions in the well-known form

$$\mathcal{F}_0 \approx 4 \int dz d\bar{z}\ |\partial\theta|^2 = -8\pi \sum_{i\neq j} \sigma_i\sigma_j \log\frac{|z_j - z_i|}{a} + C \tag{3.20}$$

describing an effective Coulomb interaction between defect charges [5], where the constant C stands for the sum of the core energies of all defects. This of course means that, even in the absence of any "activity", the defect cores will move to minimize the free energy $\mathcal{F}_0$. Hence, Q_0 textures, while being extremal on a punctured plane, are only quasi-static. The manifold of textures $Q_0(z, \bar{z}|\{z_i\})$ parameterized explicitly by $\{z_i\}$ as independent "collective" coordinates, defines the "inertial manifold" on which the relatively slow dynamics due to defect interactions unfolds [172].

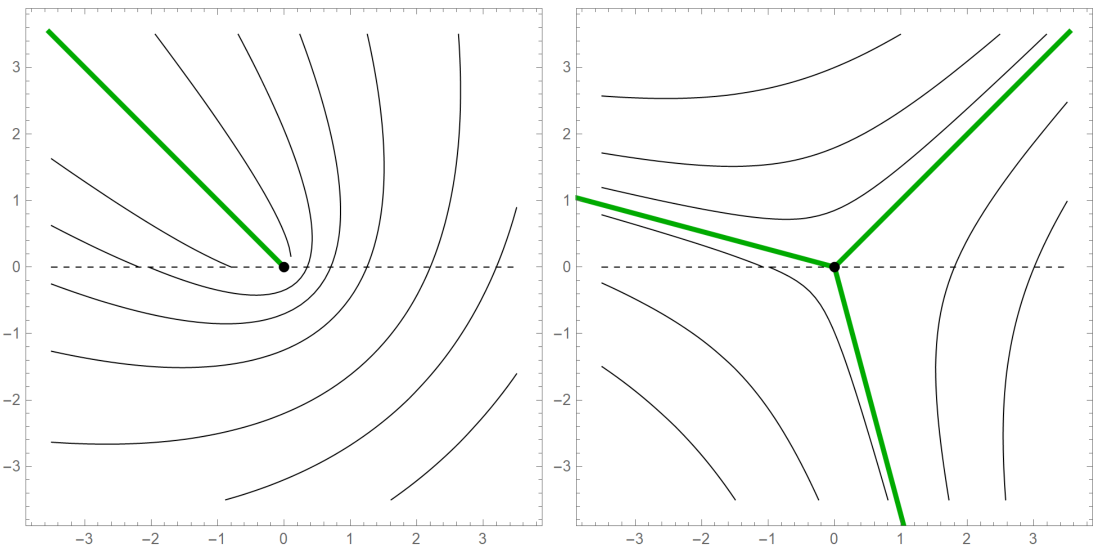

(a) +1/2 (b) −1/2 defect

Figure 3.1: Sketches of single defect textures showing the angles Φ_i for (a) a +1/2 defect where $\Phi_i = \phi_i = 3\pi/4$, and (b) a −1/2 defect where $\Phi_i^{(k)} = \phi_i/3 + 2\pi k/3$ for $k = 0 \pm 1$.

3.3.1 Matched asymptotics of moving defects

There is an exact solution for a single defect solution in the limit of linear potential, meaning that the defects are far away and conspire to create an exactly linear potential. In this case, we can find a steady-state solution of a slowly moving defect. Otherwise, we cannot do so, because there is no stationary solution because different defects move in different directions with different speeds and the assumption of the linearity of the potential breaks down. Therefore, we cannot generalize this method when there are multiple defects. Nonetheless, we will review it, because in principle it can be the beginning of a dynamic perturbative scheme.

A first step in determining the dynamics of a defect is to assume that it moves slowly and is far away from the other defects. In the limit of low density, since the defect is far from the others, we can linearize the potential, which leads to a constant force (gradient of the potential).

We will see that in order to determine the velocity, we will need to use the method of asymptotic expansions to match solutions in the defect core and the far field [173], which has been done in the passive [174, 175] and active [97, 98] cases. Here for simplicity we consider the passive case to illustrate the technique, following the presentation in Ref. [104].

Let $\mathbf{v}$ be the constant velocity of the defect. Then in the comoving defect frame, and assuming that in this frame the dynamics is quasistatic,

$$-\mathbf{v}\cdot\boldsymbol{\nabla}Q = \nabla^2 Q + 2\epsilon^{-2}(1-|Q|^2)Q \tag{3.21}$$

By small v, we mean $v = \mathcal{O}(\eta)$, where $\eta \ll 1$ is our small parameter. Similarly, we can expand the texture Q in terms of η as

$$Q = Q_0 + \eta Q_1 + \dots \tag{3.22}$$

where Q_0 is a single-defect solution to Eq. (3.9). Then the $\mathcal{O}(\eta)$ equation reads

$$-\mathbf{v}\cdot\nabla Q_0 = \mathcal{L}(Q_1, \bar{Q}_1) \tag{3.23}$$

where

$$\mathcal{L}(Q_1, \bar{Q}_1) = \nabla^2 Q_1 + 2\epsilon^{-2}(1-2|Q_0|^2)Q_1 - 2\epsilon^{-2}Q_0^2\bar{Q}_1 \tag{3.24}$$

The linear operator $\mathcal{L}$ is self-adjoint and has three eigenfunctions with zero eigenvalues, which we denote by Ψ: one corresponding to rotation ($\Psi = iQ_0$), and two corresponding to translations in the plane ($\Psi = \nabla Q_0$) of the defect. The former can be seen immediately by substitution and the latter by taking the gradient of Eq. (3.9). According to the "Fredholm alternative" condition [176], a linear system of equations can only be solved if the inhomogeneous term (in our case $\mathbf{v}\cdot\nabla Q_0$) is orthogonal to the null space of the linear operator (in our case $\mathcal{L}$).

Multiplying Eq. (3.23) by $\bar{\Psi}$ and integrating by parts twice the differential terms in $\mathcal{L}$ leads to

$$-\mathrm{Re}\int d^2x\bar{\Psi}\mathbf{v}\cdot\boldsymbol{\nabla}Q_0 = \mathrm{Re}\oint ds(\bar{\Psi}\hat{\mathbf{n}}\cdot\boldsymbol{\nabla}Q_1 - Q_1\hat{\mathbf{n}}\cdot\boldsymbol{\nabla}\bar{\Psi}) \tag{3.25}$$

Here we choose $\Psi = \nabla Q_0$. We also have to still specify the region of integration. For simplicity, we choose a disk of radius r_0, where r_0 is large compared to the defect core size a, but small compared to the far field scale set by v^{-1}, that is $a \ll r_0 \ll v^{-1}$. We do this so we can appropriately (asymptotically) match the near-field solution with the far-field solution. We now give a heuristic argument for the far field scale set by v^{-1}. Spin waves propagate from defects. We define the far field region at time t as the boundary of the wavefront of the spin waves at time t emanating from the defects at $t = 0$. In terms of time elapsed t, the wavefront emanating from a defect is at distance $\sqrt{Dt}$ from the defect, where D is the diffusivity. In the case of a single defect, we don't expect our ansatz to hold over a timescale where the defect has overtaken the spin waves. In time period t, a defect moves at most a distance $L = vt$. Equating this length scale with the length scale set by diffusion results in

$$L = vt = \sqrt{Dt} \implies L = \frac{D}{v} \tag{3.26}$$

Our task at hand is to evaluate Eq. (3.25) for a single ±1/2 defect. We do so by evaluating the LHS of Eq. (3.25) using the near-field solution and the RHS of Eq. (3.25) with the far-field solution.

In the near field, using the approximate form of Q_0 (Eq. (1.9)) to numerically compute the LHS of Eq. (3.25) leads to

$$-\mathrm{Re}\int d^2x\boldsymbol{\nabla}\bar{Q}_0\mathbf{v}\cdot\boldsymbol{\nabla}Q_0 = -\pi\mathbf{v}\ln\left(\frac{r_0}{1.126}\right) \tag{3.27}$$

In the far-field, $A \approx 1$, and so the phase of Q_1 to leading order satisfies

$$\mathbf{v}\cdot\boldsymbol{\nabla}\theta + \nabla^2\theta = 0 \tag{3.28}$$

This equation, subject to the topological charge condition $\oint d\theta = \pm\pi$ where the contour is taken around the $\pm 1/2$ defect, can be solved by introducing a dual function Φ which satisfies [104]:

$$\mathbf{v} \cdot \boldsymbol{\nabla}\Phi + \nabla^2\Phi = \pm\pi\delta(\mathbf{x}) \tag{3.29}$$

$$\hat{\mathbf{v}} \cdot \boldsymbol{\nabla}\Phi + \Phi = \pm\frac{1}{2}\hat{\mathbf{v}} \times \boldsymbol{\nabla}\theta, \quad \hat{\mathbf{v}} \times \boldsymbol{\nabla}\Phi = \mp\frac{1}{2}\hat{\mathbf{v}} \cdot \boldsymbol{\nabla}\theta \tag{3.30}$$

leading to

$$\boldsymbol{\nabla}\theta = \pm\frac{1}{2}e^{-\mathbf{v}\cdot\mathbf{r}/2}\epsilon \cdot \left[\mathbf{v}K_0\left(\frac{vr}{2}\right) - v\hat{\mathbf{r}}K_1\left(\frac{vr}{2}\right)\right] + \epsilon \cdot \mathbf{v}K \tag{3.31}$$

where $K_i(x)$ are modified Bessel functions of the 2nd kind, and K is a constant related to the weak external phase gradient due to the other defects, mentioned previously. Now evaluating the RHS of Eq. (3.25) using Eq. (3.31), and equating with the LHS of Eq. (3.25) leads to the following relation for the velocity,

$$\mathbf{v}\ln\frac{3.29}{v} = \pm 2\epsilon \cdot \boldsymbol{\nabla}\theta_{\text{ext}}, \tag{3.32}$$

where explicitly

$$\boldsymbol{\nabla}\theta_{\text{ext}}(z_i) = \partial_i \sum_{j\neq i} \sigma_j \ln\frac{r_{ij}}{a} \tag{3.33}$$

is the force felt at z_i due to all of the other defects.

3.4 Derivation of the multi-defect dynamics equations

To describe nematic dynamics in the limit of weak activity and low defect density, we shall assume that the order parameter texture $Q(z, \bar{z}, t)$ stays close to the inertial manifold $Q_0(z, \bar{z}|\{z_i(t)\})$ parameterized by time-dependent defect positions:

$$Q(z, \bar{z}, t) = Q_0(z, \bar{z}|\{z_i(t)\}) + \delta Q(z, \bar{z}, t) \ , \tag{3.34}$$

where δQ is locally perpendicular to the inertial manifold as defined by

$$\int dz d\bar{z} \ \partial_i \bar{Q}_0 \delta Q = \int dz d\bar{z} \ \bar{\partial}_i \bar{Q}_0 \delta Q = 0 \ . \tag{3.35}$$

We thus rewrite the complex texture dynamics equation Eq. (3.7) as

$$\begin{aligned} \dot{z}_i \partial_i Q_0 + \dot{\bar{z}}_i \bar{\partial}_i Q_0 + \partial_t \delta Q &= \mathcal{I} \\ &= -\frac{\delta \mathcal{F}(\{Q\})}{\delta \bar{Q}} + \alpha \mathcal{I}_\alpha(Q) \ . \end{aligned} \tag{3.36}$$

Multiplying by $\partial_i \bar{Q}_0$ and integrating over space, we find that

$$\dot{z}_j \int dz d\bar{z} \partial_i \bar{Q}_0 \partial_j Q_0 + \dot{\bar{z}}_j \int dz d\bar{z} \partial_i \bar{Q}_0 \bar{\partial}_j Q_0 = \int dz d\bar{z} \partial_i \bar{Q}_0 \mathcal{I} \ . \tag{3.37}$$

Similarly, if we multiply by $\bar{\partial}_i \bar{Q}_0$ and integrate over space, we find that

$$\dot{z}_j \int dz d\bar{z} \bar{\partial}_i \bar{Q}_0 \partial_j Q_0 + \dot{\bar{z}}_j \int dz d\bar{z} \bar{\partial}_i \bar{Q}_0 \bar{\partial}_j Q_0 = \int dz d\bar{z} \bar{\partial}_i \bar{Q}_0 \mathcal{I} \ . \tag{3.38}$$

If we use the physical fact that in our ansatz, $\dot{\bar{z}}_i$ is the complex conjugate of $\dot{z}_i$ (which means that in our time evolution $|Q_0|$ remains 1, which is the case in the deep nematic limit), we can combine these equations as follows by taking the complex conjugate of the first equation and adding it to the second, to get

$$\mathcal{M}_{ij} \dot{z}_j + \mathcal{N}_{ij} \dot{\bar{z}}_j = \int d^2 z [\bar{\partial}_i \bar{Q}_0 \mathcal{I} + \bar{\partial}_i Q_0 \bar{\mathcal{I}}] \ , \tag{3.39}$$

where

$$\mathcal{M}_{ij} = \int d^2z[\bar{\partial}_i\bar{Q}_0\partial_j Q_0 + \bar{\partial}_i Q_0\partial_j\bar{Q}_0] \tag{3.40}$$

$$\mathcal{N}_{ij} = \int d^2z[\bar{\partial}_i\bar{Q}_0\bar{\partial}_j Q_0 + \bar{\partial}_i Q_0\bar{\partial}_j\bar{Q}_0] \; . \tag{3.41}$$

Up to now, the discussion has been general. We will now work in the limit of small activity $\alpha \ll 1$ and large defect separation $\epsilon^{-1} \gg 1$. In this limit, $\delta Q \ll Q_0$ because the multi-defect texture $Q_0(z,\bar{z}|\{z_i\})$ minimizes the LdG free energy to order $\mathcal{O}(\epsilon^2)$ on the punctured plane with fixed z_i. Thus to leading order

$$\mathcal{I}(Q) \approx \mathcal{I}(Q_0) \; . \tag{3.42}$$

Now using the fact that

$$\frac{\partial\mathcal{F}}{\partial\bar{z}_i} = \int d^2z\bar{\partial}_i\bar{Q}_0\frac{\delta\mathcal{F}}{\delta\bar{Q}_0} + \int d^2z\bar{\partial}_i Q_0\frac{\delta\mathcal{F}}{\delta Q_0} \; , \tag{3.43}$$

we find that

$$\begin{aligned}\int d^2z[\bar{\partial}_i\bar{Q}_0\mathcal{I} + \bar{\partial}_i Q_0\bar{\mathcal{I}}] &= \int d^2z\bar{\partial}_i\bar{Q}_0[-\frac{\delta\mathcal{F}}{\delta\bar{Q}_0} + \alpha\mathcal{I}_\alpha(Q_0)] + \int d^2z\bar{\partial}_i Q_0[-\frac{\delta\mathcal{F}}{\delta Q_0} + \alpha\bar{\mathcal{I}}_\alpha(Q_0)] \\ &= -\frac{\partial\mathcal{F}}{\partial\bar{z}_i} + \alpha\int d^2z[\bar{\partial}_i\bar{Q}_0\mathcal{I}_\alpha + \bar{\partial}_i Q_0\bar{\mathcal{I}}_\alpha] \; . \end{aligned} \tag{3.44}$$

To summarize, our defect dynamics equations are

$$\mathcal{M}_{ij}\dot{z}_j + \mathcal{N}_{ij}\dot{\bar{z}}_j = -\frac{\partial\mathcal{F}_0}{\partial\bar{z}_i} + \mathcal{U}_i \; , \tag{3.45}$$

with

$$-\frac{\partial\mathcal{F}_0}{\partial\bar{z}_i} = 8\pi\sum_{j\neq i}\sigma_i\sigma_j\frac{1}{\bar{z}_i - \bar{z}_j} \tag{3.46}$$

being the Coulomb force computed by differentiating the Coulomb potential (Eq. (3.20)) and

$$\mathcal{U}_i = \alpha\int d^2z[\bar{\partial}_i\bar{Q}_0\mathcal{I}_\alpha + \bar{\partial}_i Q_0\bar{\mathcal{I}}_\alpha] \tag{3.47}$$

the active forcing.

It is perhaps not surprising that the equations of motion for $z_i(t)$ that we have obtained minimize the deviation of the dynamics on the inertial manifold Q_0 from the exact equation of motion Eq. (3.7). That is, we minimize

$$\begin{aligned} E &= \int d^2z \left| \partial_t Q(z,\bar{z},t) - \frac{d}{dt} Q_0(z,\bar{z}|\{z_i(t)\}) \right|^2 \\ &\approx \int d^2z \left| \mathcal{I}(Q_0) - \dot{z}_i \partial_i Q_0 - \dot{\bar{z}}_i \bar{\partial}_i Q_0 \right|^2 \end{aligned} \tag{3.48}$$

with respect to $\dot{z}_i$.

3.5 Dynamics of defects in active nematics

In the previous section, we derived multi-defect dynamics using the variational principle. In this section, we present the explicit form of the resulting equations of motion, using the results for $\mathcal{M}_{ij}$ from Appendix A.1 and for $\mathcal{U}_i$ from Appendix A.2, and discuss the nature of the various terms.

3.5.1 Mobility matrix

The matrix $\mathcal{M}_{ij}$ on the left hand side of Eq. (3.45) is the inverse mobility matrix [177] representing the correlation in the motion of defects due to the non-orthogonality of the associated textures of order parameter. A nonlocal mobility is known to occur for colloidal particles in flow due to hydrodynamic interactions [177]. Evaluating Eq. (3.40) in Appendix A.1, we find that

$$\mathcal{M}_{ij} \approx 4\pi\sigma_i\sigma_j \ln\frac{L}{r_{ij}} , \tag{3.49}$$

where

$$r_{ij} = \begin{cases} |z_i - z_j| & i \neq j \\ a \approx 0.8\epsilon & i = j \end{cases} \tag{3.50}$$

and L is system size. Only the diagonal part of $\mathcal{M}_{ij}$ receives contributions from the defect cores.

3.5.2 Interactions due to active flows

We next present the result of evaluating the active forcing term $\mathcal{U}_i$ defined in Eq. (3.47). In Appendix A.2, we show that

$$\alpha\mathcal{U}_i = \pi\alpha a^{-1} e^{i\phi_i}\delta_{2\sigma_i,1} + \sum_{j\neq i} f_{ij} , \tag{3.51}$$

where

$$f_{ij} = -2\pi\alpha \frac{\sigma_i \sigma_j}{1-\sigma_j} \frac{\bar{q}_{ij} - (-1)^{\delta_{\sigma_i+\sigma_j,1}} q_{ij}}{\bar{z}_i - \bar{z}_j} \tag{3.52}$$

and

$$q_{ij} = e^{i\phi_i} \left(\frac{z_i - z_j}{\bar{z}_i - \bar{z}_j} \right)^{\sigma_i - 1} = e^{2i(1-\sigma_i)\Phi_i} \left(\frac{z_i - z_j}{\bar{z}_i - \bar{z}_j} \right)^{\sigma_i - 1} , \tag{3.53}$$

with $\Phi_i = \frac{\phi_i}{2(1-\sigma_i)}$ the defect phase defined in Fig. 3.3.

The first term in Eq. (3.51) is the well-known "self-propulsion" of the $\sigma_i = +1/2$ defect that arises from the flows that the defect itself generates [92, 97], with the phase factor $e^{i\phi_i}$ controlling the direction. The latter is therefore recognized as the polarization (unit) vector of the +1/2 defect (see for e.g. [163, 164, 98]).

The second term describes forces induced by interaction with other defects, represented by the sum of pairwise terms, that like 2D Coulomb forces are inversely proportional to the pair separation $|z_i - z_j|$. Unlike Coulomb forces, pairwise forces here are in general non-reciprocal and depend on the relative positions of all other defects through the phase factor $e^{i\phi_i}$, thus incorporating many-body effects. Note that $\bar{q}_{ij} - (-1)^{\delta_{\sigma_i+\sigma_j,1}} q_{ij}$ is real, corresponding to a central force, only in the case of $\sigma_i = \sigma_j = 1/2$. In all other cases, this factor is purely imaginary, corresponding to active forces that act normal to the line joining defect positions, thus resulting in a torque acting on the pair, that depends on the orientation of the pair relative to other defects and the order parameter in the far field.

Finally, for completeness we provide an explicit form of the multi-defect dynamics equations including both passive and active forces. After eliminating common factor of 4π from both sides, these are given by

$$\sum_k \left(\sigma_i \sigma_k \log \frac{L}{r_{ik}} \right) \dot{z}_k = 2 \sum_{j \neq i} \frac{\sigma_i \sigma_j}{\bar{z}_i - \bar{z}_j} + \frac{\alpha e^{i\phi_i}}{4a} \delta_{2\sigma_i,1} - \frac{\alpha}{2} \sum_{j \neq i} \frac{\sigma_i \sigma_j}{(1-\sigma_j)} \frac{\bar{q}_{ij} - (-1)^{\delta_{\sigma_i+\sigma_j,1}} q_{ij}}{\bar{z}_i - \bar{z}_j} . \tag{3.54}$$

The three terms on the right hand side are, in order, the Coulomb interaction, the active self-propulsion of the $+1/2$ defects, and the active interactions. This description of defect dynamics has a number of new features discussed below.

3.5.3 Non-centrality and non-reciprocity in active interactions

In contrast to Coulombic interaction between defects, interactions mediated by active flow cannot be described by additive pair potentials. Nevertheless, active force acting on a given defect is represented as a sum of of pairwise terms which one interprets as a force exerted by one defect on another, even though this force depends in a specific way (through tensor q_{ij} appearing in Eq. (3.54)) on the global texture and hence on position of all other defects.

The active pairwise force term in Eq. (3.54) has a non-trivial form and we now examine it in greater detail. For a plus/minus disclination pair, we find that the force exerted on defect i by defect j is:

$$f_{ij} = -\frac{i\pi\alpha}{1-\sigma_j}\frac{\sin[2(1-\sigma_i)(\Phi_i-\theta_{ij})]}{\bar{z}_i-\bar{z}_j} \quad \text{for} \quad \sigma_i \neq \sigma_j \ , \tag{3.55}$$

where θ_{ij} is the angle of the line joining z_j to z_i relative to the x-axis and we have used $\phi_i = 2(1-\sigma_i)\Phi_i \pmod{2\pi}$. Notice that here, and in the following expressions, $\Phi_i - \theta_{ij}$ is the relative angle between the polarization and line connecting the defects. This force acts perpendicular to the line connecting the defects and is clearly non-reciprocal since $\sigma_i \neq \sigma_j$, hence $|f_{ij}| \neq |f_{ji}|$. As a result, the disclination pair will experience a net force acting on its center of mass, as well as a torque which tends to rotate the pair until the line joining the defect centers aligns with the far-field phase. This is particularly clear in a system with just a single neutral disclination pair. In this case, $2(1-\sigma_i)\Phi_i = 2\sigma_j\theta_{ij} + 2\psi$. Hence $\sin[2(1-\sigma_i)(\Phi_i-\theta_{ij})] = \sin(2\psi - 2\theta_{ij})$. Assigning $\sigma_i = 1/2$, $\sigma_j = -1/2$ (and

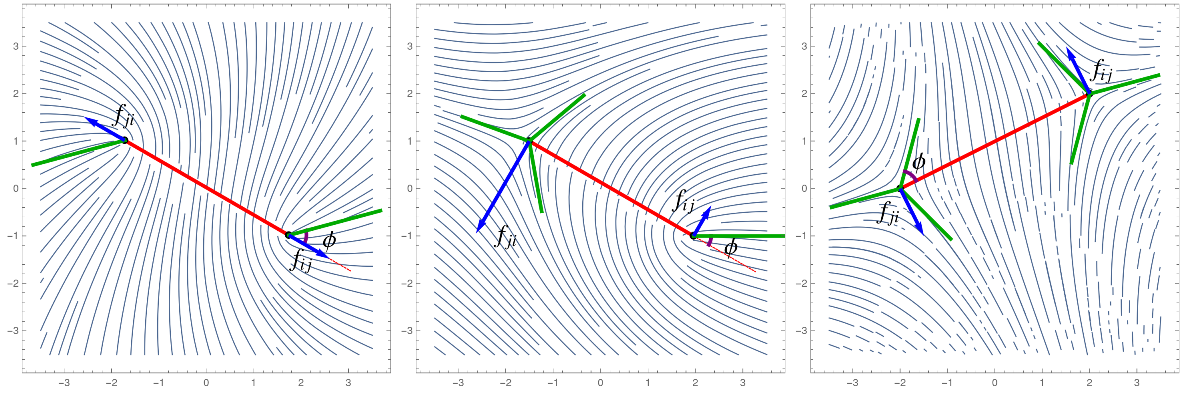

(a) +1/2 and +1/2 defects (b) −1/2 and +1/2 defects (c) −1/2 and −1/2 defects

Figure 3.2: Sketches of the active forces between defect pairs in an extensile system ($\alpha < 0$). The blue arrows denote the forces, the red line joins the center of the two defects, and $\phi = \Phi_i - \theta_{ij}$ denotes the angle of the polarization relative to the line connecting the two defects. For $(+1/2, +1/2)$ pairs, the forces are radial, but for the $(-1/2, +1/2)$ and $(-1/2, -1/2)$ pairs, they are perpendicular to the line connecting the defects, generating rotations of the pair.

defining $z_i - z_j = r_{ij}e^{i\theta_{ij}}$) we have

$$\begin{aligned} f_{ij} &= -\frac{1}{3}\,\frac{2i\pi\alpha e^{i\theta_{ij}}}{r_{ij}}\sin 2(\psi - \theta_{ij}) \\ f_{ji} &= \frac{2i\pi\alpha e^{i\theta_{ij}}}{r_{ij}}\sin 2(\psi - \theta_{ij})\ . \end{aligned} \tag{3.56}$$

Due to the $1/(1-\sigma_j)$ prefactor in Eq. (3.55), the force acting on the plus-disclination (i) is 3 times smaller than the force acting on the minus-disclination (j), resulting in a net force acting on the center of mass, perpendicular to the axis of the pair. There is also a torque $T_{ij} = \frac{2}{3}|f_{ji}|r_{ij}$ that rotates the pair so as to align θ_{ij} with ψ - the order parameter orientation in the far field. Physically, this dynamics is due to the entrainment of the defects to the active flows generated by the global texture, with rotational invariance broken by the nematic orientation in the far field.

The force on a plus disclination at z_i arising from a second plus disclination at z_j is

$$f_{ij} = \frac{2\pi\alpha\cos(\Phi_i - \theta_{ij})}{\bar{z}_i - \bar{z}_j} \quad \text{for} \sigma_i = \sigma_j = 1/2 \ . \tag{3.57}$$

This force acts along the line connecting the two defects. For a pair of plus-disclinations far away from all other defects, $\phi_i = \phi_j + \pi$, and so $f_{ij} + f_{ji} = 0$. Otherwise, $\phi_i \neq \phi_j + \pi$, and so $f_{ij} + f_{ji} \neq 0$. This lack of reciprocity is due to the gradient of the "phase field" of the nematic texture. The presence of other defects cannot be forgotten in this case because a pair of same sign defects alone does not satisfy the boundary conditions at infinity: at least two negative charge disclinations must be present to satisfy (topological) charge neutrality. We also note explicit dependence of f_{ij} on the phase of Q at infinity, 2ψ, (which additively contributes to ϕ_i). Rotating this phase would modulate the magnitude of f_{ij} - an effect that is made plausible by noting that the same phase uniformly rotates the active stress tensor everywhere and hence rotates the direction of active flow relative to $z_i - z_j$.

Finally, for a pair of minus-disclinations the force acting on z_i is given by

$$f_{ij} = \frac{i2\alpha\pi}{3}\frac{\sin(3(\Phi_i - \theta_{ij}))}{\bar{z}_i - \bar{z}_j} \quad \text{for} \quad \sigma_i = \sigma_j = -\frac{1}{2} \ . \tag{3.58}$$

Like the force in a neutral pair, this force also acts perpendicular to the line $z_i - z_j$, thus generating a "2-body torque". It is also non-reciprocal, thus yielding a net force acting on the pair.

The nonreciprocity and non-central character of the forces between defect pairs arise because the texture, as described by the Q tensor, is nonlinear in the director, hence in the defect phases. So, even if we write the texture as a linear superposition of individual defect phases, the flow generated by the texture is a nonlinear superposition of the flow generated by individual defects. As a result, the flow near one defect depends on the flow due to the other defects.

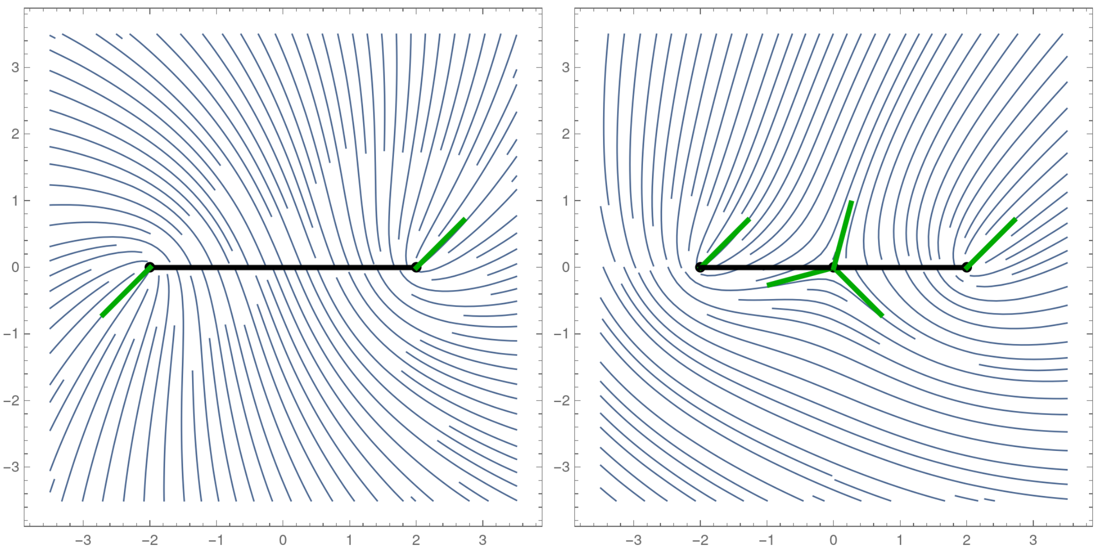

(a) Two neighboring +1/2 defects

(b) Two +1/2 defects separated by a −1/2 defect

Figure 3.3: In (a), two neighboring +1/2 defects anti-align, and in (b), since the +1/2 defects are separated by a −1/2 defect, they align.

3.5.4 Dynamics of +1/2 defect polarization

To illustrate our results and make contact with earlier work [85, 98, 99], we also construct an explicit equation for the dynamics of the polarization of a "tagged" +1/2 defect defined by the phase ϕ_i in the field of other defects. Differentiating Eq. (3.19) with respect to time, we obtain

$$\frac{d\phi_i}{dt} = -i\sum_{j\neq i}\sigma_j\left(\frac{\dot{z}_i-\dot{z}_j}{z_i-z_j} - c.c\right) . \tag{3.59}$$

For simplicity, we evaluate this equation in the dilute limit, when interaction between defects (and the off-diagonal elements of the mobility matrix) can be neglected and defect motion is dominated by the active drift of plus-defects, with the result

$$\begin{aligned}\frac{d\phi_i}{dt} &\approx -ic\alpha \sum_{j\neq i} \frac{\sigma_j e^{i\phi_i}}{z_i - z_j} + ic\alpha \sum_{j^+\neq i} \frac{\sigma_{j_+} e^{i\phi_j}}{z_i - z_{j_+}} + c.c \\ &= -2c\alpha\ \mathcal{E}_i \sin(\Theta_i - \phi_i) - 2c\alpha \sum_{j_+\neq i} \frac{\sigma_{j_+}}{r_{ij_+}} \sin(\theta_{ij_+} - \phi_{j_+})\ , \end{aligned} \tag{3.60}$$

where $c = [a \ln L/a]^{-1}$. In the 1st term, we have defined

$$\mathcal{E}_i e^{i\Theta_i} = \sum_{j\neq i} \frac{\sigma_j}{\bar{z}_i - \bar{z}_j}\ . \tag{3.61}$$

and in the 2nd term, the sum over j_+ runs only over plus-defects. Up to a numerical factor, $\mathcal{E}_i$ is the "electrostatic field" at point z_i due to other defects. The 1st term in Eq. (3.60) describes the tendency of the plus-defect polarization in extensile (contractile) systems to align (anti-align) with the direction of net Coulomb force acting on it. This term already appeared in the equation for polarization dynamics derived in [98] by examining the dynamics of a single defect in the mean field of other defects. It is purely kinematic in origin as it arises from defect self-advection. The second term in Eq. (3.60) is new. The general structure of the polarization dynamics equation persists when defect dynamics $\dot{z}_i$ includes interaction terms of Eq. (3.54), which will cause the motion of minus-defects contributing to the second term in Eq. (3.60). Finally, we note in our formulation of the problem the equation for defect polarization dynamics is superfluous, as this polarization is defined kinematically by defect positions via Eq. (3.19).

Explicit dependence of polarization on defect positions given by Eq. (3.19) provides some useful insights. For example, it is easy to see that two neighboring plus disclinations far removed from all other defects have their polarizations anti-align with each other (independent of the orientation of the pair axis). However, the presence of a minus-disclination (or plus-disclination) in between leads to the alignment of the polarizations of the two flanking plus-disclinations (see Fig. 3.3). These effects have been noted in earlier work on defect orientation [163, 164], as well as in recent numerical and experimental studies [168, 169].

3.6 Discussion

We have presented a general formalism, based on the variational principle, to derive a set of coupled ordinary differential equations governing multi-defect dynamics for a 2D active nematic deep in the nematic phase. Our analysis goes beyond earlier work that obtained the dynamics of a single "tagged" defect in the mean-field of other defects [98], to capture the coupled dynamics of a many-defect texture. This yields a number of new results and explicitly demonstrates the non-central and non-reciprocal nature of active stress-induced defect-defect interactions [178].

Central to our approach is the realization that deep in the nematic state, order parameter textures stay close to a 2N-dimensional "inertial manifold" defined by the quasi-static multi-defect solution Q_0 parameterized by defect positions. By explicitly describing multi-defect configurations, we obtain a closed formulation that describes defect dynamics entirely in terms of the defect positions. This avoids the need to treat polarization as an independent degree of freedom, as was done in earlier work [98]. Here the polarization of the $+1/2$ defect and the orientation of the $-1/2$ as defined by the "defect phase" Φ_i are expressed explicitly in terms of defect positions through Eq. (3.19).

Dynamics of the latter defines the relatively slow flow on the inertial manifold of textures by comparison to the rapid ($\sim \mathcal{O}(\epsilon^{-2})$) rate of relaxation of deviations away from the manifold. The separation of time scales that enables us to describe the dynamics of Q by projecting it onto the inertial manifold holds as long as the mean separation between defects is large compared to the coherence length ξ ($\epsilon^2 \ll 1$). In our analysis here, the defect density was treated as given by the initial condition. More realistically, nematic disclinations are subject to pairwise creation and annihilation. Extensive simulations of the continuum equations of active nematics have demonstrated that the state of spatio-temporal chaotic defect dynamics is characterized by a steady mean defect density $\ell^{-2} =$

$\ell_{active}^{-2} \sim \alpha$ [94, 159, 96].

One of the new results of our analysis is the recognition that defect velocities are directly coupled to each other through the inverse mobility matrix (on the left hand side of Eq. (3.54)). This effect, while resembling a "collective drag", is purely kinematic in origin as it arises from the non-orthogonality of order parameter deformations, $\partial_i Q_0$, associated with translational motion of individual defects. Off-diagonal elements of the mobility matrix are only logarithmically smaller than the diagonal ones $\sim \log(L/r_{ij})/\log(L/a)$.

Chapter 4

Extensions of Multi-defect Dynamics in Active Nematics

In this chapter, we extend and build upon the material presented in Chapter 3 in several different directions. First, as a check of our model, we compute the residual error and present the results of various simulations. Then in considering the first excited states, we allow the polarization to be dynamical. We also formulate the continuum model, including the case where the polarization is dynamical. Finally, we initiate analysis on the torus, an example of a non-trivial geometry, as well as on a finite disk.

4.1 Residual

As a first check of our model, we can compute the residual error R^2, which we define as

$$R^2 = \frac{E}{\int d^2z|\mathcal{I}|^2} \tag{4.1}$$

We first compute R^2 in the passive case ($\alpha = 0$), and then in the active case ($\alpha \neq 0$).

4.1.1 $\alpha = 0$

When $\alpha = 0$, we have

$$\int d^2z|\mathcal{I}_{\text{passive}}|^2 \approx \int d^2zA^2 \left| \sum_{<ij>} \frac{1}{(z-z_i)(\bar{z}-\bar{z}_j)} \right|^2 \tag{4.2}$$

which has leading part

$$\int d^2z|\mathcal{I}|^2 \approx 4\pi \sum_{<ij>} \frac{\alpha_i^2\alpha_j^2 \log r_{ij}/a}{r_{ij}^2} \tag{4.3}$$

The leading part of $\mathcal{M}_{ij}^{-1}$ is

$$\mathcal{M}_{ij}^{-1} \approx \frac{1}{4\pi\alpha_i^2 \log L/a}\delta_{ij} \tag{4.4}$$

and using

$$V_i = 8\pi\alpha_i \sum_{j\neq i} \alpha_j \frac{\hat{z}_{ij}}{r_{ij}} \tag{4.5}$$

we arrive at

$$R^2 \approx 1 - \frac{1}{\log L/a} \frac{\sum_i \left| \sum_{j\neq i} \frac{(2\alpha_j)\hat{z}_{ij}}{r_{ij}} \right|^2}{\sum_{<ij>} \frac{\log r_{ij}/a}{r_{ij}^2}} \tag{4.6}$$

If r is a typical separation between defects,

$$R^2_{\alpha=0} \approx 1 - \frac{1}{(\log L/a)(\log r/a)} \tag{4.7}$$

Note that in this formula, we can take L to be the smallest L that contains all of the defects. If we assume we have N defects, and if we assume $r \sim N^{\gamma} a$ for some $\gamma > 0$, then we find that

$$R^2_{\alpha=0} \approx 1 - \frac{1}{\gamma(\gamma+1)(\log N)^2} \tag{4.8}$$

4.1.2 $\alpha \neq 0$

When $\alpha \neq 0$, the leading contribution of $\mathcal{I}$ comes from $\mathcal{I}_{\text{active}}$, so

$$\mathcal{I}_{\text{active}} \approx -Q^2 \sum_i \frac{\alpha_i}{(z-z_i)^2} + \sum_i \frac{\alpha_i}{(\bar{z}-\bar{z}_i)^2} \tag{4.9}$$

Integrating

$$\int d^2z |\mathcal{I}|^2 = 2\alpha^2 \int d^2z \left| \sum_i \frac{\alpha_i}{(z-z_i)^2} \right|^2 = \frac{N\pi\alpha^2}{2a^2} \tag{4.10}$$

where we have dropped the cross term which only appears if we have +1 defects.

Comparing to Eq. (4.3), we find that if

$$\alpha^2 \gg 8 \sum_{<ij>} \left(\frac{a}{r_{ij}}\right)^2 \log \frac{r_{ij}}{a} \tag{4.11}$$

which is reasonable assumption since $a/r_{ij} \ll 1$, we find that Eq.4.10 dominates over the other term.

Now using

$$V_i = \frac{\pi\alpha}{a} Q_i \delta_{2\alpha_i,1} \tag{4.12}$$

we find that

$$R^2 \approx 1 - \frac{2f^+}{\log L/a} \tag{4.13}$$

where $f^+ = N^+/N$ is the fraction of +1/2 defects. Now if we assume charge neutrality, $f^+ = 1/2$, and so

$$R^2_{\alpha\neq 0} \approx 1 - \frac{1}{\log L/a} \tag{4.14}$$

If r, the typical separation between defects, scales as $r \sim N^{\gamma} a$ for some $\gamma > 0$, then we find that

$$R^2_{\alpha\neq 0} \approx 1 - \frac{1}{(\gamma + \frac{1}{2})(\log N)} \tag{4.15}$$

Thus comparing Eq. (4.15) to Eq. (4.8), we find that our ansatz for Q is better when $\alpha \neq 0$ because of the extra factor of $\log N$, making R^2 closer to 1 when $\alpha = 0$.

4.2 Numerical simulations

4.2.1 Method of Simulation

Our physical parameters are size of the square box L, the location of defects, g, and α. We run three different sets of simulations:[2] for the polarization, for eight defects, where half each are $+1/2$ and $-1/2$ defects, and for a pair of $-1/2$ defects.

4.2.2 Polarization

One of the striking features of our model is that the polarization for defects are fixed by the defect positions. We would like to check this prediction. In Fig. (4.1), we simulated the dynamics of 40 randomly positioned defects (twenty $+1/2$ defects, and twenty $-1/2$ defects). We used the defect positions from the simulation to compute the value of polarization for each $+1/2$ defect based on our model, and compared it to the polarization from the simulation. We found that the two are strongly correlated with Pearson correlation coefficient of 93%! This is despite the fact that some of the defects annihilated each other during the simulation.

4.2.3 Multi-defect interactions

For the case of 8 defects (half $+1/2$ defects and half $-1/2$ defects), we check our prediction for the defect velocity with the actual defect velocity from simulation. We choose $\alpha = 0.2$, $g = 10$, and system is a square box of length 200. Initially the defects are randomly positioned far from the boundary. We fix L by $\pi L^2 = L_x^2$, where $L_x = 200$ the size of the box. We also study the effect of toggling the various terms in our prediction for the defect velocities. We turn off one at a time the off-diagonal component of the mobility

---

[2] I would like to thank Zhihong You and Supavit Pokawanwit for sharing their code, which I adapted.

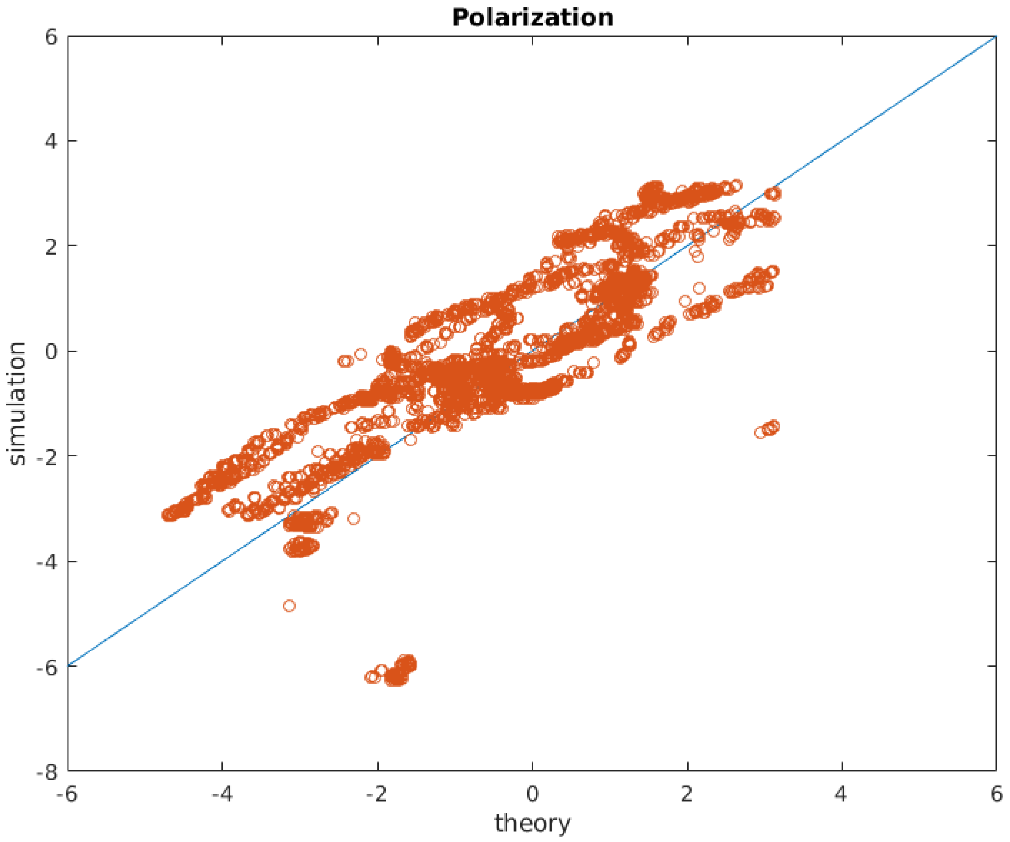

Figure 4.1: Scatter plot of polarization (theory vs simulation). $\alpha = 1.0$, $g = 10$, defects are in a square box of size 20, and system is square box of length 100.

matrix, the motility term, the Coulomb term, and the active pair-wise force interactions. We find that as expected the off-diagonal component of the mobility matrix is important for the drag of the $-1/2$ defects, and in particular, its absence is responsible for the tilt in Fig. 4.2(b). Similarly, we can see the importance of the other terms. We see in Fig. 4.2(c) that the motility is the most important term, followed by the Coulomb force. Since $\alpha = 0.2$ is small, the active pair-wise force interaction is much smaller than Coulomb and turning it off does not have much of an impact.

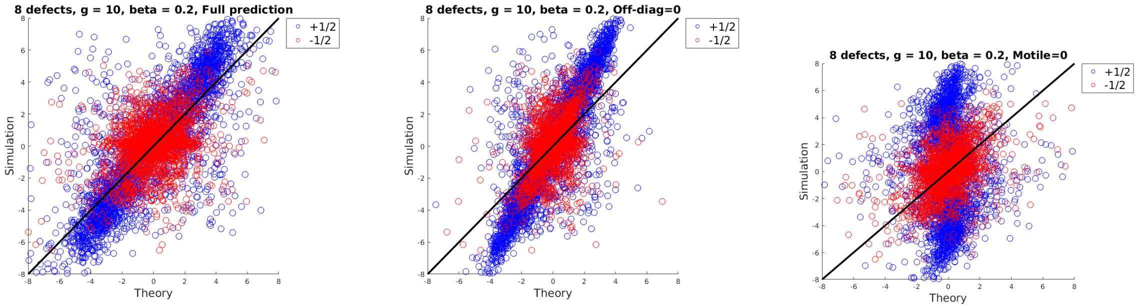

(a) Full prediction (b) Diagonal mobility (c) Motility term off

Figure 4.2: Scatter plot of velocity components (theory vs simulation) for four ±1/2 defect pairs randomly positioned far from the boundary. $\alpha = 0.2$, $g = 10$, and system is square box of length 200.

4.2.4 $-1/2$ defect pair

In order to isolate the effect of active pair-wise forces, it is best to consider the simplified case of only two $-1/2$ defects, where there are no motile forces that dominate the dynamics. In this case, we only have the collective defect drag force, the Coulomb force, and the torque-like active pair-wise force. For a pair of $-1/2$ defects, we check our prediction for the defect velocity with the actual defect velocity from simulation.

All length are in units of the coherence length $\xi = 1/\sqrt{g} = 1/\sqrt{10}$. System is square box of length 150ξ, where $\xi = 1/\sqrt{g}$. Velocity components are in units of D/ξ, where D is the diffusivity. Activity $\alpha = 1$. In Fig. We plot the theoretical predictions for the components of the defect velocities vs the simulation results (see Fig. (4.4)).

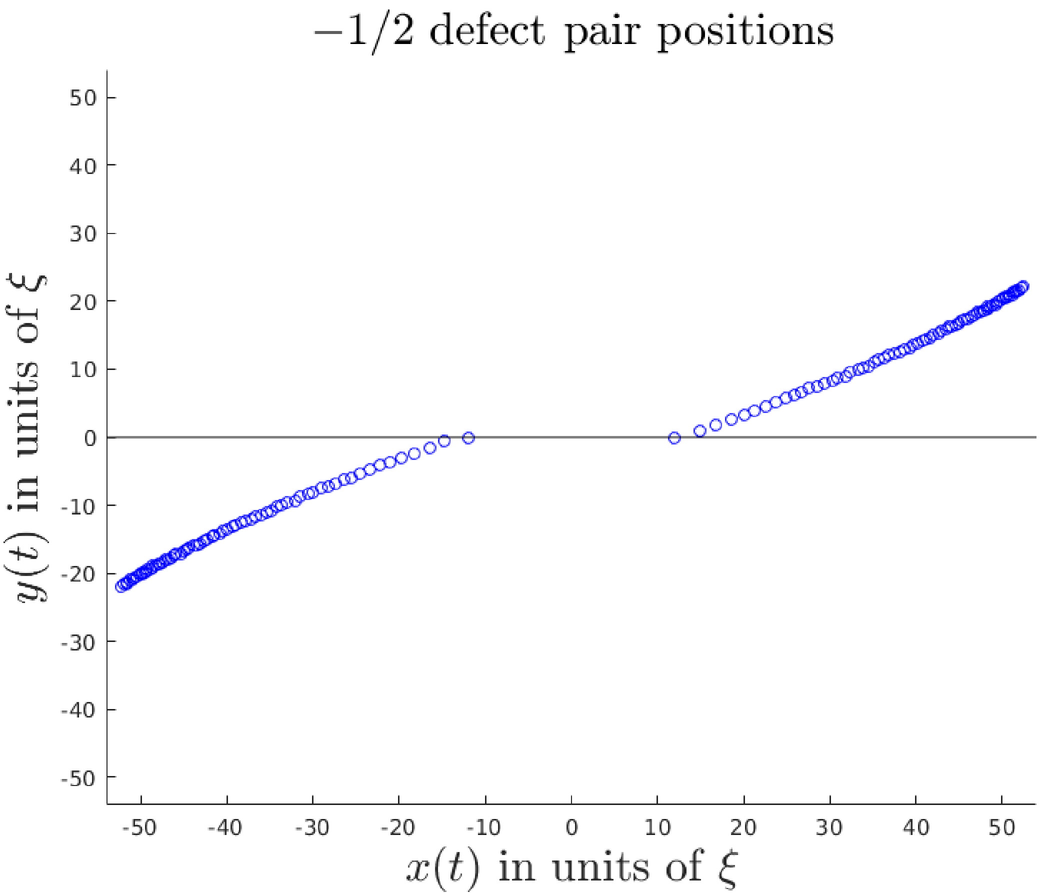

Figure 4.3: $-1/2$ defect positions as a function of time t.

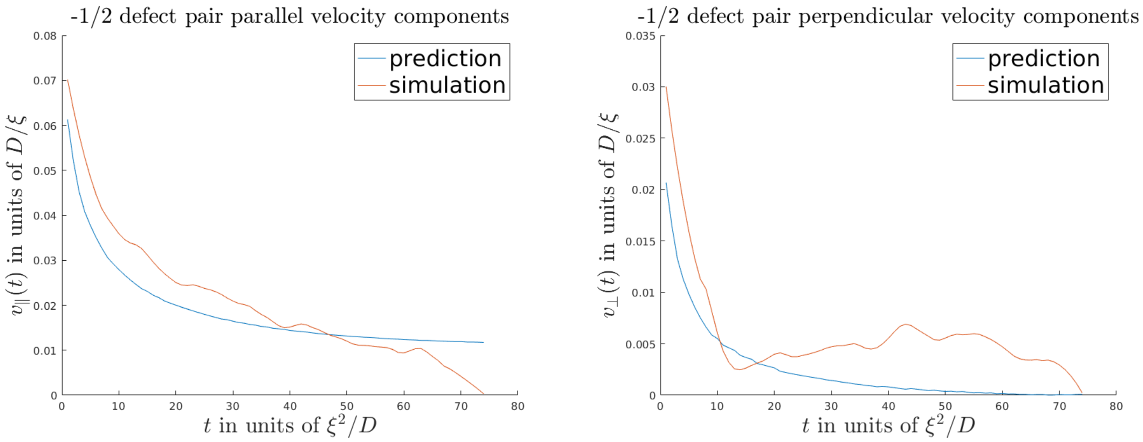

Figure 4.4: Parallel (left panel) and perpendicular (right panel) components of velocity as a function of time t. For later time, agreement is within discretization error.

4.3 Polarization deformation dynamics

Up to now, we have focused on ground state dynamics, where polarizations are frozen by defect positions. Here, we extend our analysis by considering higher energy excitations involving deformations of polarizations. The lowest energy configurations with deformation polarizations have been studied in [164] and they correspond to taking defect charge σ_i to have an imaginary part. That is, we take $\sigma_i \to \tilde{\sigma}_i = \sigma_i + \frac{1}{2} i\gamma_i$, where $\gamma_i \in \mathbb{R}$. Then

$$Q_0(z) \to Q_0(z) \prod_i e^{\frac{i}{2}\gamma_i \ln|z-z_i|^2} \tag{4.16}$$

$$Q_i \to Q_i \prod_j e^{\frac{i}{2}\gamma_j \ln|z_i-z_j|^2} \tag{4.17}$$

Therefore, writing $Q_i = e^{i\theta_i}$, we have

$$\theta_i \to \theta_i - \mathcal{M}_{ij}\gamma_j \tag{4.18}$$

where $\mathcal{M}_{ij} = \ln \frac{L}{r_{ij}}$ as defined previously. Due to boundary condition at infinity,

$$\sum_i \gamma_i = 0 \tag{4.19}$$

For simplicity, we consider the passive case where $\alpha = 0$ (but the analysis can easily be extended to $\alpha \neq 0$).

Differentiating E (Eq. (3.48)) with respect to $\bar{z}_i$, and γ_i, the equations of motion are, respectively,

$$\mathcal{M}_{ij}\dot{z}_j + \mathcal{N}_{ij}\dot{\bar{z}}_j + \mathcal{L}_{ij}\dot{\gamma}_j = \int d^2z[\bar{\partial}_i\bar{Q}_0\mathcal{I} + \bar{\partial}_i Q_0\bar{\mathcal{I}}] \tag{4.20}$$

$$\mathcal{K}_{ij}\dot{\gamma}_j + \mathcal{L}^{\dagger}_{ij}\dot{z}_j + \mathcal{L}^{T}_{ij}\dot{\bar{z}}_j = \int d^2z[\frac{\partial\bar{Q}_0}{\partial\gamma_i}\mathcal{I} + c.c] \tag{4.21}$$

where

$$\mathcal{M}_{ij} = \int d^2z[\bar{\partial}_i\bar{Q}_0\partial_j Q_0 + \bar{\partial}_i Q_0\partial_j\bar{Q}_0] \tag{4.22}$$

$$\mathcal{N}_{ij} = \int d^2z[\bar{\partial}_i\bar{Q}_0\bar{\partial}_j Q_0 + \bar{\partial}_i Q_0\bar{\partial}_j\bar{Q}_0] \tag{4.23}$$

$$\mathcal{L}_{ij} = \int d^2z[\bar{\partial}_i\bar{Q}_0\frac{\partial Q_0}{\partial\gamma_j} + \bar{\partial}_i Q_0\frac{\partial\bar{Q}_0}{\partial\gamma_j}] \tag{4.24}$$

$$\mathcal{K}_{ij} = \int d^2z\left[\frac{\partial\bar{Q}_0}{\partial\gamma_i}\frac{\partial Q_0}{\partial\gamma_j} + c.c\right] \tag{4.25}$$

First $\mathcal{M}_{ij}$ becomes

$$\mathcal{M}_{ij} = \delta_{ij}4\pi|\tilde{\sigma}_i|^2\ln\frac{L}{a} + (1-\delta_{ij})4\pi\bar{\tilde{\sigma}}_i\tilde{\sigma}_j\ln\frac{L}{r_{ij}} \tag{4.26}$$

$\mathcal{N}_{ij}$ is unmodified

$$\mathcal{N}_{ij} = 0 \tag{4.27}$$

$\mathcal{L}_{ij}$ is

$$\mathcal{L}_{ij} = -2i\bar{\tilde{\sigma}}_i\int d^2zA^2\frac{1}{\bar{z}-\bar{z}_i}\ln\left|\frac{z-z_j}{\ell}\right| = 4\pi i\bar{\tilde{\sigma}}_i z_{ij}\left(\frac{1}{2}+\ln\frac{L}{r_{ij}}\right) \tag{4.28}$$

because

$$\begin{aligned} 2\int d^2z\frac{1}{\bar{z}-\bar{z}_i}\ln\frac{|z-z_j|}{\ell} &= 4\bar{\partial}_i\int d^2z\ln\frac{|z-z_i|}{\ell}\frac{\ln|z-z_j|}{\ell} && (4.29)\\ &= 2\bar{\partial}_i\mathcal{K}_{ij} && (4.30)\\ &= -4\pi z_{ij}\left(\frac{1}{2}+\ln\frac{L}{r_{ij}}\right) && (4.31) \end{aligned}$$

The passive part becomes to modified to

$$\int d^2z[\bar{\partial}_i\bar{Q}_0\mathcal{I}_{\text{passive}} + \bar{\partial}_i Q_0\bar{\mathcal{I}}_{\text{passive}}] = 4\pi\sum_{j\neq i}\frac{1}{\bar{z}_{ij}}(\bar{\tilde{\sigma}}_i\tilde{\sigma}_j + c.c) \tag{4.32}$$

Putting it all together, we arrive at

$$\sum_j 4\pi\bar{\tilde{\sigma}}_i\tilde{\sigma}_j \ln\frac{L}{r_{ij}}\dot{z}_j + \sum_j 4\pi i\bar{\tilde{\sigma}}_i z_{ij}\left(\frac{1}{2}+\ln\frac{L}{r_{ij}}\right)\dot{\gamma}_j = 4\pi\sum_{j\neq i}\frac{1}{\bar{z}_{ij}}(\bar{\tilde{\sigma}}_i\tilde{\sigma}_j + c.c) \tag{4.33}$$

The mobility matrix for $\dot{\gamma}_i$ is

$$\mathcal{K}_{ij} = \int d^2z\left[\frac{\partial\bar{Q}_0}{\partial\gamma_i}\frac{\partial Q_0}{\partial\gamma_j} + c.c\right] = 2\int d^2zA^2\left(\ln\frac{|z-z_i|}{\ell}\right)\left(\ln\frac{|z-z_j|}{\ell}\right) \tag{4.34}$$

By symmetry, we can write $\mathcal{K}_{ij} = I(|z_{ij}|^2)$. Now using the fact that

$$\frac{\partial^2\mathcal{K}_{ij}}{\partial\bar{z}_i\partial z_j} = \pi\ln\frac{L^2}{z_{ij}\bar{z}_{ij}} \tag{4.35}$$

we find that $I(u = z_{ij}\bar{z}_{ij})$ obeys

$$-I' - uI'' = \pi\ln\frac{L^2}{u} \tag{4.36}$$

and so

$$\mathcal{K}_{ij} = I = -2\pi r_{ij}^2\left(1+\ln\frac{L}{r_{ij}}\right) \tag{4.37}$$

We now compute the Coulomb contribution. We first note that

$$\mathcal{I}_{\text{passive}} = \nabla^2 Q_0 + 2g(1-A^2)Q_0 = 4Q_0\sum_{<jk>}\bar{\partial}\log\psi_j\partial\log\psi_k \tag{4.38}$$

$$+ Q_0\sum_{jk}\left[-\frac{\gamma_j}{\bar{z}-\bar{z}_j}\frac{\gamma_k}{z-z_k} + 2i\bar{\partial}\ln\psi_j\frac{\gamma_k}{z-z_k} + 2i\frac{\gamma_j}{\bar{z}-\bar{z}_j}\partial\ln\psi_k\right] \tag{4.39}$$

and so

$$\frac{\partial \bar{Q}_0}{\partial \gamma_i}\mathcal{I}_{\text{passive}} + c.c$$

$$= 2A^2 \ln \frac{|z-z_i|}{\ell} \sum_{jk} \left[\bar{\partial} \ln \psi_j \frac{\gamma_k}{z-z_k} + \frac{\gamma_j}{\bar{z}-\bar{z}_j} \partial \ln \psi_k \right] + c.c \tag{4.40}$$

$$= 2A^2 \ln \frac{|z-z_i|}{\ell} \sum_{jk} \left[\left(\bar{\partial} \ln A_j - \frac{\alpha_j}{\bar{z}-\bar{z}_j} \right) \frac{\gamma_k}{z-z_k} + \frac{\gamma_j}{\bar{z}-\bar{z}_j} \left(\partial \ln A_k + \frac{\alpha_k}{z-z_k} \right) \right] + c.c \tag{4.41}$$

$$= 2A^2 \ln \frac{|z-z_i|}{\ell} \sum_{jk} \left[\bar{\partial} \ln A_j \frac{\gamma_k}{z-z_k} + \frac{\gamma_j}{\bar{z}-\bar{z}_j} \partial \ln A_k \right] + c.c \tag{4.42}$$

$$= 4A^2 \ln \frac{|z-z_i|}{\ell} \sum_{jk} \bar{\partial} \ln A_j \frac{\gamma_k}{z-z_k} + c.c \tag{4.43}$$

$$= 2 \ln \frac{|z-z_i|}{\ell} \sum_{jk} \partial_r (A_j^2) \frac{z-z_j}{|z-z_j|} \frac{\gamma_k}{z-z_k} + c.c \tag{4.44}$$

Integrating, we have

$$\int d^2z d_i \bar{Q}_0 \mathcal{I}_{\text{passive}} + c.c = 2 \int d^2z \ln \frac{|z-z_i|}{\ell} \sum_{jk} \partial_r (A_j^2) \frac{z-z_j}{|z-z_j|} \frac{\gamma_k}{z-z_k} + c.c \tag{4.45}$$

We now compute each term. We first note that because of phase integral,

$$\int d^2z \ln \frac{|z-z_i|}{\ell} \sum_{<jk>} \partial_r (A_j^2) \frac{z-z_j}{|z-z_j|} \frac{\gamma_k}{z-z_k} + c.c = 0 \tag{4.46}$$

Therefore, in the double sum, $j = k$. Using this observation, we compute:

$$2 \int d^2z \ln \frac{|z-z_i|}{\ell} \partial_r (A_i^2) \frac{\gamma_i}{|z-z_i|} + c.c = 8\pi \int dr \ln \frac{r}{\ell} \partial_r (A_i^2) \gamma_i = 8\pi \gamma_i \ln \frac{a''}{\ell} \tag{4.47}$$

where $a'' \approx \frac{1.04}{\sqrt{g}}$.

$$2\int d^2z \ln\frac{|z-z_i|}{\ell}\sum_{j\neq i}\partial_r(A_j^2)\frac{\gamma_j}{|z-z_j|}+c.c = 4\sum_{j\neq i}\ln\frac{r_{ij}}{\ell}\int d^2z\partial_r(A_j^2)\frac{\gamma_j}{|z-z_j|} \tag{4.48}$$

$$= 8\pi\sum_{j\neq i}\ln\frac{r_{ij}}{\ell}\int dr\partial_r(A_j^2)\gamma_j \tag{4.49}$$

$$= 8\pi\sum_{j\neq i}\gamma_j\ln\frac{r_{ij}}{\ell} \tag{4.50}$$

Putting it all together,

$$\sum_j\left[\left(4i\pi\tilde{\sigma}_j\bar{z}_{ij}\left(\frac{1}{2}+\ln\frac{L}{r_{ij}}\right)\dot{z}_j+c.c\right)-2\pi r_{ij}^2\left(1+\ln\frac{L}{r_{ij}}\right)\dot{\gamma}_j\right]=8\pi\sum_j\gamma_j\ln\frac{r_{ij}}{\ell} \tag{4.51}$$

Comparing the two expressions, we have

$$\sum_j 4\pi\bar{\tilde{\sigma}}_i\tilde{\sigma}_j\ln\frac{L}{r_{ij}}\dot{z}_j+\sum_j 4\pi i\bar{\tilde{\sigma}}_i z_{ij}\left(\frac{1}{2}+\ln\frac{L}{r_{ij}}\right)\dot{\gamma}_j = 4\pi\sum_{j\neq i}\frac{1}{\bar{z}_{ij}}(\bar{\tilde{\sigma}}_i\tilde{\sigma}_j+c.c) \tag{4.52}$$

$$\sum_j\left[\left(4i\pi\tilde{\sigma}_j\bar{z}_{ij}\left(\frac{1}{2}+\ln\frac{L}{r_{ij}}\right)\dot{z}_j+c.c\right)-2\pi r_{ij}^2\left(1+\ln\frac{L}{r_{ij}}\right)\dot{\gamma}_j\right]=8\pi\sum_j\gamma_j\ln\frac{r_{ij}}{\ell}+C \tag{4.53}$$

where C is constant chosen to enforce $\sum_j\dot{\gamma}_j=0$.

4.4 Continuum limit

In this section we derive the continuum limit of our model. We define

$$\rho(r) = \sum_i \alpha_i \delta^2(r - r_i) \tag{4.54}$$

$$v(r) = \sum_i \dot{z}_i \delta^2(r - r_i) \tag{4.55}$$

We also define ϑ to be the deviation of the polarization θ from that determined by defect positions. In other words,

$$\theta_{tot} = \theta + \vartheta \tag{4.56}$$

and it satisfies

$$\nabla^2 \vartheta = 2\pi\gamma \tag{4.57}$$

As a reminder, we consider the case where there is no activity, i.e. $\alpha = 0$. We first consider the simpler case of no polarization deformation dynamics allowed, and then we allow polarization deformations to be dynamical.

4.4.1 Static polarization deformations case

Let $n^{\pm}$ be the number density of ± defects, ϕ the Coulomb potential, and $\vec{J}^{\pm}$ the number current density of ± defects. Explicitly,

$$n^{\pm}(r) = \sum_{i=\pm} \delta^2(r - r_i) \tag{4.58}$$

$$\vec{J}^{\pm} = \sum_{i=\pm} \dot{z}_i \delta^2(r - r_i) \tag{4.59}$$

The continuity equation for $n^{\pm}$ reads

$$\frac{\partial n^{\pm}}{\partial t} + \boldsymbol{\nabla} \cdot \vec{J}^{\pm} = 0 \tag{4.60}$$

For notational convenience, we also define the charge density and charge current density as

$$\rho(r) = \frac{1}{2}(n^{+}(r) - n^{-}(r)) \tag{4.61}$$

$$\vec{J}(r) = \frac{1}{2}(J^{+}(r) - J^{-}(r)) \tag{4.62}$$

where the factors of 1/2 are due to the 1/2 charge.

Then the charge conservation equation is

$$\frac{\partial \rho}{\partial t} + \boldsymbol{\nabla} \cdot \vec{J} = 0 \tag{4.63}$$

and the Coulomb potential ϕ satisfies

$$\nabla^2 \phi = -2\pi\rho \tag{4.64}$$

which has solution

$$\phi(r) = \int d^2r' \log \frac{L}{|r - r'|} \rho(r') \tag{4.65}$$

In terms of $\vec{J}$ and ϕ, the continuum limit of the defect dynamics equation for $\alpha = 0$, Eq. (3.54), is

$$\int d^2r' \log \frac{L}{|r - r'|} \vec{J}(r') = -2\boldsymbol{\nabla}\phi \tag{4.66}$$

Interestingly enough, the mobility matrix, in the continuum limit, can be viewed as the 2D Green's function, i.e., inverse of the Laplacian, and that will be crucial for us, as we will now see.

To summarize, we are interested in solving the following set of coupled equations:

$$\nabla^2 \phi = -2\pi\rho \tag{4.67}$$

$$\frac{\partial \rho}{\partial t} + \boldsymbol{\nabla} \cdot \vec{J} = 0 \tag{4.68}$$

$$\int d^2r' \log \frac{L}{|r - r'|} \vec{J}(r') = -2\boldsymbol{\nabla}\phi \tag{4.69}$$

Taking the divergence of Eq. (4.69), we have

$$\begin{aligned}
-2\nabla^2\phi &= \boldsymbol{\nabla}\cdot\int d^2r' \log\frac{L}{|r-r'|}\vec{J}(r') \\
&= -\int d^2r' \left(\boldsymbol{\nabla}'\log\frac{L}{|r-r'|}\right)\cdot\vec{J}(r') \\
&= \int d^2r' \log\frac{L}{|r-r'|}\boldsymbol{\nabla}\cdot\vec{J}(r') \\
&= -\int d^2r' \log\frac{L}{|r-r'|}\frac{\partial\rho(r')}{\partial t} \\
&= -\frac{\partial}{\partial_t}\int d^2r' \log\frac{L}{|r-r'|}\rho(r') \\
&= -\frac{\partial\phi}{\partial t}
\end{aligned} \tag{4.70}$$

and so we arrive at a diffusion equation for ϕ

$$\frac{\partial\phi}{\partial t} = 2\nabla^2\phi \tag{4.71}$$

We can view the diffusion equation as relaxational dynamics for the Coulomb energy $E = \int d^2r(\boldsymbol{\nabla}\phi)^2$. Note that if assume that $\boldsymbol{\nabla}\times\vec{J} = 0$, we could have instead started here, i.e., assumed relaxational dynamics for ϕ and derived the mobility matrix, including the off-diagonal terms, in the defect dynamics equation. Therefore the off-diagonal nature of the mobility matrix is a necessary ingredient for the particle-vortex duality between θ and ϕ, which we will now review. The phase θ describes the vortex, i.e., defects, and the potential ϕ describes the density of the particles, i.e. defects. Explicitly,

$$\theta(z) = -i\frac{1}{2}\int d^2z' \log\frac{z-z'}{\bar{z}-\bar{z}'}n^+(z') + i\frac{1}{2}\int d^2z' \log\frac{z-z'}{\bar{z}-\bar{z}'}n^-(z') \tag{4.72}$$

$$= -i\int d^2z' \log\frac{z-z'}{\bar{z}-\bar{z}'}\rho(z') \tag{4.73}$$

$$\phi(z) = -\frac{1}{2}\int d^2z' \log\frac{|z-z'|^2}{L^2}n^+(z') + \frac{1}{2}\int d^2z' \log\frac{|z-z'|^2}{L^2}n^-(z') \tag{4.74}$$

$$= -\int d^2z' \log\frac{|z-z'|^2}{L^2}\rho(z') \tag{4.75}$$

Differentiating, we find that

$$\partial\phi = -i\frac{1}{2}\partial\theta \tag{4.76}$$

or in other words

$$d\theta = 2 * d\phi, \tag{4.77}$$

where $*$ is the Hodge star operator. This means that θ (which describes Q) is dual to ϕ and this is a manifestation of particle-vortex duality.

Note that ϕ is always well-defined. However, Eq. (4.77) only defines $\boldsymbol{\nabla}\theta$, not θ. In order for θ to be well-defined, it follows from Eq. (4.76) that

$$\nabla^2\phi = \nabla^2\theta = 0 \tag{4.78}$$

from which follows that

$$\rho = 0 \implies n^+ = n^- \tag{4.79}$$

$$\boldsymbol{\nabla}\cdot\vec{J} = 0 \implies \boldsymbol{\nabla}\cdot\vec{J}^+ = \boldsymbol{\nabla}\cdot\vec{J}_i \tag{4.80}$$

$$\frac{\partial\phi}{\partial t} = 0 \implies \phi = \phi(r) \tag{4.81}$$

Now if we assume at infinity that θ and ϕ are constants, then they are both constant everywhere since they are solutions of Laplace's equation.

4.4.2 Dynamical polarization deformations case

We now allow the polarization deformations to be dynamical. We define

$$\sigma(r) = \sum_i \tilde{\sigma}_i \delta^2(r - r_i) \tag{4.82}$$

The set of equations can be expressed as

$$\int d^2z' \begin{pmatrix} \bar{\sigma}(z)\partial\bar{\partial}\tilde{G} & 0 & \bar{\sigma}(z)\bar{\partial}\tilde{G} \\ 0 & \alpha(z)\partial\bar{\partial}\tilde{G} & -\alpha(z)\partial\tilde{G} \\ -\partial\tilde{G} & \bar{\partial}\tilde{G} & -\frac{1}{2}\tilde{G} \end{pmatrix} \begin{pmatrix} \alpha(z')v(z') \\ \bar{\sigma}(z')\bar{v}(z') \\ \dot{\alpha}(z') - \dot{\bar{\sigma}}(z') \end{pmatrix} \tag{4.83}$$

$$= -\int d^2z' \begin{pmatrix} \frac{1}{\bar{z}-\bar{z}'}(\bar{\sigma}(z)\alpha(z') + \alpha(z)\bar{\sigma}(z')) \\ \frac{1}{z-z'}(\bar{\sigma}(z)\alpha(z') + \alpha(z)\bar{\sigma}(z')) \\ 2\ln\frac{L}{|z-z'|}(\alpha(z') - \bar{\sigma}(z')) \end{pmatrix} \tag{4.84}$$

where

$$\tilde{G}(z,z') = |z-z'|^2\left(1 + \ln\frac{L}{|z-z'|}\right) , \tag{4.85}$$

which satisfies

$$\partial\bar{\partial}\tilde{G} = G(z,z') = -\ln\frac{|z-z'|}{L} . \tag{4.86}$$

The third equation gives dynamics of γ and we find that it leads to conserved current, that is,

$$\partial_t\gamma + \boldsymbol{\nabla}\cdot\vec{J}_\gamma = 0 \tag{4.87}$$

where

$$\vec{J}_\gamma = \gamma\vec{v} - \boldsymbol{\nabla}\gamma + 2\epsilon\cdot\vec{J}_\rho \tag{4.88}$$

$$\vec{J}_\rho = \rho\vec{v} \tag{4.89}$$

and ϵ is the 2D Levi-Civita symbol.

There are three contributions to $\vec{J}_\gamma$: one along $\vec{v}$, another perpendicular to $\vec{v}$, and the third along the gradient of γ. Note that interestingly enough, in addition to the terms that we may expect, we have the extra term $\epsilon\cdot\vec{J}_\rho$, which may have interesting consequences.

In terms of ϑ, which satisfies

$$\nabla^2\vartheta = 2\pi\gamma \tag{4.90}$$

and applying inverse of Laplacian, we find that

$$\partial_t\vartheta = \nabla^2\vartheta + \int d^2r' G(r,r')\nabla\cdot(\gamma\vec{v} + 2\epsilon\cdot\vec{J}_\rho) \tag{4.91}$$

which after integrating by parts becomes

$$\partial_t\vartheta = \nabla^2\vartheta + \int d^2r' \frac{\gamma(\vec{r}-\vec{r}')\cdot\vec{v} + 2\rho(\vec{r}-\vec{r}')\times\vec{v}}{|\vec{r}-\vec{r}'|^2} \tag{4.92}$$

For the polarization $\hat{e}_i$ of $+1/2$ defect (ignoring ϑ), we had obtained

$$\frac{d}{d\tau}\hat{e}_i = -\frac{\alpha}{2a}(\vec{F}_i^{Coul}\times\hat{e}_i)\varepsilon\cdot\hat{e}_i + \frac{\alpha}{a}\sum_{j^+\neq i}\frac{\hat{r}_{ij}\times\hat{e}_j}{r_{ij}}\varepsilon\cdot\hat{e}_i \tag{4.93}$$

Including the contribution of ϑ to θ_{tot}, and using Eq. (4.92), we obtain

$$\frac{d}{d\tau}\hat{e}_i = -\frac{\alpha}{2a}(\vec{F}_i^{Coul}\times\hat{e}_i)\varepsilon\cdot\hat{e}_i + A\nabla^2\vartheta + \frac{\alpha}{a}\sum_{j^+\neq i}\frac{\hat{r}_{ij}\times\hat{e}_j}{r_{ij}}\varepsilon\cdot\hat{e}_i + A\int d^2r'\frac{\gamma(\vec{r}-\vec{r}')\cdot\vec{v} + 2\rho(\vec{r}-\vec{r}')\times\vec{v}}{|\vec{r}-\vec{r}'|^2} \tag{4.94}$$

where $A = \log L/a$. Comparing to Eq. A10 of [99], we see that their terms correspond to the first two above and we get three additional terms.

The defect dynamics equation is now modified. What we had obtained when $\gamma = 0$ is for the dynamics of the potential ϕ, or equivalently ρ (related by $\nabla^2\phi = -2\pi\rho$), is

$$\partial_t\phi = 2\nabla^2\phi \tag{4.95}$$

$$\partial_t\rho = 2\nabla^2\rho \tag{4.96}$$

Note that in particular, the 2nd equation can be written as

$$\partial_t\rho + \boldsymbol{\nabla}\cdot\tilde{J}_\rho = 0 \tag{4.97}$$

where

$$\tilde{J}_\rho = -2\nabla\rho \tag{4.98}$$

Now we will work out the leading correction[3] to this equation for small $\gamma \ll \rho$, and we find that

$$\partial_t\rho + \boldsymbol{\nabla}\cdot\tilde{J}_\rho = 0 \tag{4.99}$$

where

$$\tilde{J}_\rho = -2\nabla\rho + \frac{\gamma}{2}\epsilon\cdot\vec{v} - \frac{1}{2\pi}\nabla\left(\nabla\left(\frac{\gamma}{\rho}\right)\times\nabla\phi\right) \tag{4.100}$$

It thus follows that

$$\boldsymbol{\nabla}\cdot\vec{J}_\rho = \boldsymbol{\nabla}\cdot\tilde{J}_\rho \tag{4.101}$$

and so (up to transverse piece)

$$\rho\vec{v} = -2\nabla\rho + \frac{\gamma}{2}\epsilon\cdot\vec{v} - \frac{1}{2\pi}\nabla\left(\nabla\left(\frac{\gamma}{\rho}\right)\times\nabla\phi\right) \tag{4.102}$$

---

[3] It is not hard to write the full equation, but we choose to not do so for simplicity of presentation.

4.5 Geometry

Up to now, we have only considered the geometry of an infinite plane. Consequently, the mobility matrix has a $\log L$ divergence, where L is the system size. We formally dealt with this infrared divergence by assuming that the defects are confined to a subregion much smaller than L. The analysis can be done on a finite disc using the method of images, or alternatively, on the surface of a sphere or a torus, where the radius naturally suppresses the divergence. We comment that studying these geometries is practically relevant as well since experiments have realized active nematics on such curved surfaces [85, 87, 72].

Here we initiate the analysis on a finite disc and a torus, and consider the spherical geometry in Chapter 6.

4.5.1 Torus

We now consider the case of the torus, a non-trivial geometry. Consider a periodic box where we identify $z \sim z+1 \sim z+\tau$, where $\tau = \tau_1 + i\tau_2$ (one can rescale by a factor of L if one wants). The Jacobi-Theta function $\vartheta(z) = \vartheta_{11}(z, q)$ is defined to be

$$\vartheta(z) = -2q^{1/4}\sin(\pi z)\prod_{m=1}^{\infty}(1-q^{2m})(1-q^{2m}e^{2\pi iz})(1-q^{2m}e^{-2\pi iz}) \tag{4.103}$$

where $q = e^{i\pi\tau}$. It is easy to check that

$$\vartheta(z+1) = -\vartheta(z), \qquad \vartheta(z+\tau) = e^{-2\pi iz - i\pi\tau}\vartheta(z) \tag{4.104}$$

It is also important to note that $\vartheta(z)$ has no poles and vanishes only at $z = 0$, where

$$\vartheta(z) = az + \mathcal{O}(z^2) \tag{4.105}$$

Any elliptic function f can be written as a product of ϑ-functions as follows:

$$f(z) = \prod_i \frac{\vartheta(z - z_i^+)}{\vartheta(z - z_i^-)} \tag{4.106}$$

where $z_i^{\pm}$ are the positions of the $\pm 1/2$ defects. Note that for f to be well-defined on the torus, i.e., $f(z) = f(z+1) = f(z+\tau)$, we must have (due to shift symmetries of ϑ-function)

$$\sum_i (z_i^+ - z_i^-) = 0 \tag{4.107}$$

which is consistent with Abel-Jacobi theorem. Therefore, our ansatz for the texture is

$$Q = \frac{f(z)}{|f(z)|} \tag{4.108}$$

However, there is a way to relax this constraint at the expense of making f not just a function of z. Since there is an equal number of poles and zeros, i.e. an equal number of $+1/2$ and $-1/2$ defects at arbitrary positions, by taking instead

$$f(z,\bar{z}) = e^{-\frac{\pi}{\tau_2}\sum_i (z_i^+ - z_i^-)(z-\bar{z})} \prod_i \frac{\vartheta(z - z_i^+)}{\vartheta(z - z_i^-)} \tag{4.109}$$

one can see that $f(z,\bar{z})$ is single-valued, even if $\sum_i (z_i^+ - z_i^-) \neq 0$. Now our ansatz for the texture becomes

$$Q = e^{i\theta} = \frac{f(z,\bar{z})}{|f(z,\bar{z})|} \tag{4.110}$$

Note that this is still a good ansatz for us because it satisfies $\partial\bar{\partial}\theta = 0$ as required in the deep nematic limit.

4.5.2 Finite disk

In the case of a finite disk, there are corrections to $\mathcal{M}_{ij}$. We compute the finite size contributions in a disc of radius R with a constant boundary condition on Q at $|z| = R$. We use the method of images by replacing

$$\log\left[\frac{z - z_i}{\bar{z} - \bar{z}_i}\right] \to \log\left[\frac{z - z_i}{\bar{z} - \bar{z}_i}\right] + \log\left[\frac{z^{-1}R^2 - \bar{z}_i}{\bar{z}^{-1}R^2 - z_i}\right] , \tag{4.111}$$

since the added term is analytic for $|z| < R$. Since $\mathcal{N}_{ij} \sim \mathcal{O}(R^0)$, it suffices to compute corrections to $\mathcal{M}_{ij}$. In other words, we are interested in computing

$$\mathcal{M}_{ij} = 2\sigma_i\sigma_j I \ , \tag{4.112}$$

$$I = \int d^2z \frac{\left(1 - \frac{r^2}{R^2}\right)^2}{(z - z_i)(\bar{z} - \bar{z}_j)} \frac{1}{\left(1 - \frac{z_i\bar{z}}{R^2}\right)\left(1 - \frac{\bar{z}_j z}{R^2}\right)} \ . \tag{4.113}$$

Using $z = rw$, where $w = e^{i\phi}$, and doing the contour integral over w, we get

$$I = 2\pi \frac{1}{1 - \frac{z_i\bar{z}_j}{R^2}} \left[\int_a^R \frac{dr}{r} \ \frac{\Theta(r - |z_i|) - \Theta(|z_j| - r)}{1 - r^{-2}z_i\bar{z}_j} \left(1 - \frac{r^2}{R^2}\right) - \frac{1}{R^2} \int r dr \frac{\left(1 - \frac{r^2}{R^2}\right)^2}{1 - \frac{r^2 z_i\bar{z}_j}{R^4}}\right] \tag{4.114}$$

Now doing the integral over r yields

$$\begin{aligned}
\mathcal{M}_{ij} &= 2\sigma_i\sigma_j I \\
&= 2\pi\sigma_i\sigma_j \left[\ln\left(\frac{R^2 - z_i\bar{z}_j}{r_{ij}^2}\right) - \frac{1 - \frac{r_i^2 + r_j^2}{R^2}}{1 - \frac{z_i\bar{z}_j}{R^2}}\right] \\
&+ \sigma_i\sigma_j \frac{\pi R^4 \left(\bar{z}_j z_i \left(3\bar{z}_j z_i - 2R^2\right) - 2\left(R^2 - \bar{z}_j z_i\right)^2 \log\left(1 - \frac{\bar{z}_j z_i}{R^2}\right)\right)}{\bar{z}_j^3 z_i^3 \left(\bar{z}_j z_i - R^2\right)} \\
&= 4\pi\sigma_i\sigma_j \left[\ln\frac{R}{r_{ij}} - \frac{5}{12} + \frac{1}{4R^2}(\bar{z}_j z_i \ln\frac{r_{ij}^2}{R^2} + r_i^2 + r_j^2 - \frac{11}{6}\bar{z}_j z_i)\right] \\
&\quad + \mathcal{O}(1/R^4)
\end{aligned} \tag{4.115}$$

Chapter 5

Defect Dynamics in Active Polar Fluids

5.1 Introduction

Up to now, we have mainly focused on active nematics. Another class of active matter is active polar fluids, which consists of active polar units that tend to align, locally generating polar order [32, 33, 109]. The phase diagram of active polar fluids has been extensively studied (for example, [116, 158, 179, 113, 115, 180, 109]), and defects have been observed in for example [55, 62, 56, 57, 114]. In contrast to active nematics, since active polar fluids have long range order [105, 106], defects are not spontaneously generated, and if generated due to boundary effect for example, the defects are expected to be transient [107, 108, 109]. That being said, aspects of dynamics of defects in active polar fluids have been studied in [110, 111, 112, 113, 114, 115, 107]. Here we study transient dynamics of defects, and give another perspective why they are transient.

In this chapter, we study both the transient and long-time behavior of defects in two-dimensional active polar fluids in the limit of strong order and overdamped, compressible flow. As in [101, 100], we consider an approximation for the global texture motivated from the passive case where the defects are widely separated and quasi-static, and use the variational principle to find defect dynamics within this ansatz. Here we shall follow the general approach of [100]. In contrast to previous work on the active nematics model [75, 84, 92, 97, 100], in this model we find that there are no active self-propulsion terms for the lowest charge (±1) energy excitations. Also in contrast to [100], we obtain interactions between two defects that are neither central nor perpendicular to a central force; they are generically non-central. By extending this ansatz to allow orientation dynamics of defects, we find that the orientation of +1 defects, unlike that of $\pm 1/2$ defects in active nematics [100], is not locked to defect positions and relaxes to asters, which we confirm with simulations. Moreover, using a scaling argument, we explain the transient feature of active polar defects and show that in the steady state, active polar fluids are either devoid of defects or consist of a single aster.

5.2 The Model

We consider a two-dimensional polar fluid with density ρ and vector order parameter $\mathbf{p}$ described by the free energy [10, 116] $\mathcal{F}(\{\mathbf{p}\})$:

$$\mathcal{F}(\{\mathbf{p}\}) = \mathcal{F}_n(\{\mathbf{p}\}) + \mathcal{F}_p(\{\mathbf{p}\}) \; , \tag{5.1}$$

where

$$\mathcal{F}_n(\{\mathbf{p}\}) = \frac{1}{2}\int dxdy \left[C\left(\frac{\delta\rho}{\rho_0}\right)^2 + K\; Tr(\boldsymbol{\nabla}\mathbf{p})^2 + g(1-\mathbf{p}^2)^2\right] \; , \tag{5.2}$$

$$\mathcal{F}_p(\{\mathbf{p}\}) = \int dxdy B\frac{\rho}{\rho_0}\boldsymbol{\nabla}\cdot\mathbf{p} \tag{5.3}$$

and ρ_0 is the equilibrium value of ρ.

The first term, $\mathcal{F}_n(\{\mathbf{p}\})$, is the usual free energy of a liquid crystal which contains only terms even in $\mathbf{p}$ [10], and the second term, $\mathcal{F}_p(\{\mathbf{p}\})$, contains additional terms that break this $\mathbf{p} \to -\mathbf{p}$ symmetry. K is the Frank constant in the one-constant approximation, and g controls the strength of polar order. We assume to be deep in the ordered state ($g \to \infty$), where the coherence length $\xi = \sqrt{K/2g}$ is the smallest relevant lengthscale and $|\vec{p}| \approx 1$ except within polar defect cores of size $a \sim \xi$. Although symmetry allows us to write terms that are odd in $\mathbf{p}$ as in $\mathcal{F}_p$, and that density fluctuations are generally important for polar fluids, for simplicity of analysis and in order to connect with a nematic we will assume that this contribution due to $\mathcal{F}_p(\{\mathbf{p}\})$ can be ignored, for example by imposing $\mathbf{p} \to -\mathbf{p}$ symmetry, or assuming that b is small, or we are in a region where gradients in density are small.

Relaxation towards the minimum of the free energy while advection by flow $\mathbf{v}$ leads to

$$\partial_t p_i + \mathbf{v}\cdot\boldsymbol{\nabla}p_i + \omega_{ij}p_j = -\frac{D}{4K}\frac{\delta\mathcal{F}}{\delta p_i} \; , \tag{5.4}$$

where D is the diffusivity and $\omega_{ij} = (\partial_i v_j - \partial_j v_i)/2$ is the vorticity. In the overdamped limit, $\mathbf{v} = v_0\mathbf{p}$, where v_0 has the dimensions of a speed and represents the speed of an isolated active particle. With this assumption, our equations now take the form of the Toner-Tu equations [105, 106, 181] (see [182] for a clear exposition):

$$\partial_t p_i + \frac{v_0}{2}\mathbf{p} \cdot \boldsymbol{\nabla} p_i = -\frac{D}{4K}\frac{\delta \mathcal{F}}{\delta p_i} \ , \tag{5.5}$$

In Eq. (5.4) we have dropped the rate of strain alignment term [116, 32] because in $2D$ and in the overdamped limit, its effect on dynamics can be represented by renormalizing the advection term. We rescale length with ℓ, where ℓ is the characteristic separation between topological defects, and time with $\tau = \ell^2/D$. We assume that defects are widely separated, that is $\ell \gg \xi$, and thus define the dimensionless small parameter $\epsilon = \xi/\ell \ll 1$. We also define the dimensionless activity parameter $\lambda = v_0/8D$.

As in [100], it is convenient to adopt the language of complex analysis. In terms of complex coordinates $z = x + iy$ and $\bar{z} = x - iy$, the complex partial derivatives $\partial = \partial_z = \frac{1}{2}(\partial_x - i\partial_y)$ and $\bar{\partial} = \partial_{\bar{z}} = \frac{1}{2}(\partial_x + i\partial_y)$, and the complex order parameter $p = p_x + ip_y$, the (dimensionless) free energy takes the form

$$\mathcal{F}(\{p\}) = \int dz d\bar{z} \left[4|\partial p|^2 + \epsilon^{-2}(1 - |p|^2)^2\right] \ . \tag{5.6}$$

Finally, the equation of motion can be written as

$$\partial_t p = \mathcal{I}(p) = -\frac{\delta \mathcal{F}(\{p\})}{\delta \bar{p}} + \lambda \mathcal{I}_\lambda(p) \ , \tag{5.7}$$

where

$$\mathcal{I}_\lambda(p) = -(p\partial + \bar{p}\bar{\partial})p \ . \tag{5.8}$$

5.3 Stationary and quasi-stationary textures deep in the ordered state

For simplicity, we first consider the passive case where $\lambda = 0$. Then we are interested in solving

$$\partial_t p = -\frac{\delta \mathcal{F}(\{p\})}{\delta \bar{p}} = 4\partial\bar{\partial} p + 2\epsilon^{-2}(1-|p|^2)\ . \tag{5.9}$$

Since this model was studied in [100], we will simply review it here. The single defect solution is

$$p = \psi(z,\bar{z}) = A(|z|)\left(\frac{z}{|z|}\right)^{\sigma}\ , \tag{5.10}$$

with the amplitude $A(|z|)$ describing the defect core [104]: as $r \to 0$, $A(r) \propto r$, and for $r \gg \epsilon$, $A(r) \simeq 1 - \frac{\epsilon^2}{4r^2}$.

The multi-defect solution takes the form

$$p_0(z,\bar{z}|\{z_i\}) = e^{i\psi}\prod_i \Psi_i = e^{i\psi}\prod_i A(|z-z_i|)\left(\frac{z-z_i}{|\bar{z}-\bar{z}_i|}\right)^{\sigma_i}\ , \tag{5.11}$$

where ψ is the phase of p at infinity. This texture satisfies the boundary condition $p \to e^{i\psi}e^{i\varphi\sum_i \sigma_i}$ as $|z| \to \infty$, where φ is the polar angle. In the special case of a charge neutral system, $\sum_i \sigma_i = 0$, and so p is constant on the boundary.

In the limit $\epsilon \to 0$, the multi-defect texture $p_0(z,\bar{z}|\{z_i\})$ is the minimizer of $\mathcal{F}(p)$ when defects are pinned (see e.g. [183] and references within). In terms of the defect positions z_i, the free energy $\mathcal{F}_0 = \mathcal{F}(p_0)$ takes the well-known form

$$\mathcal{F}_0 \approx 2\pi\sum_{i\neq j}\sigma_i\sigma_j \log\frac{|z_j - z_i|}{L}, \tag{5.12}$$

which describes a Coulomb interaction between defect charges [5], where L is the system size. Due to the Coulomb interaction, even in the absence of any “activity”, the defect cores will move to minimize the free energy $\mathcal{F}_0$. Thus even though p_0 textures minimize the free energy when defects are pinned, they are only quasi-static when the defects are no longer pinned.

As noted in [100], near a defect z_i, we can write

$$p_0(z,\bar{z}) \approx P_i \Psi_i(z-z_i, \bar{z}-\bar{z}_i) \; . \tag{5.13}$$

where

$$P_i = e^{i\phi_i} = e^{i\psi} \prod_{j\neq i} \left(\frac{z_i - z_j}{|z-z_j|} \right)^{\sigma_j} \; . \tag{5.14}$$

is a phase factor that will play an important role in the active induced dynamics of the defects. See Fig. 5.1 for a geometrical interpretation.

Finally, we note that for a global rotation, under which $z \to e^{i\eta} z$, the complex order parameter transforms as $p_0 \to p_0 e^{i\eta(1-\sum_i \sigma_i)}$. This implies that if $\sum_i \sigma_i \neq 1$, we can choose η such that it eliminates the global phase factor ψ. In particular, we cannot eliminate the phase for a single +1 defect. This obstruction is not surprising since +1 defects are unique among defects in that they are rotationally invariant as $p \propto z$. We will see in our analysis that ψ plays a crucial role for +1 defects.

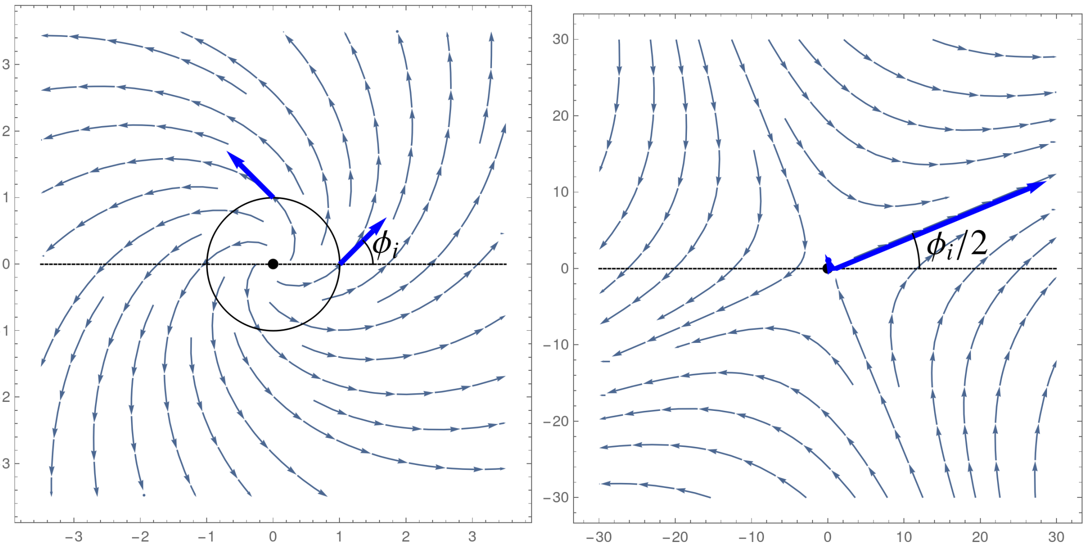

(a) +1 defect (b) −1 defect

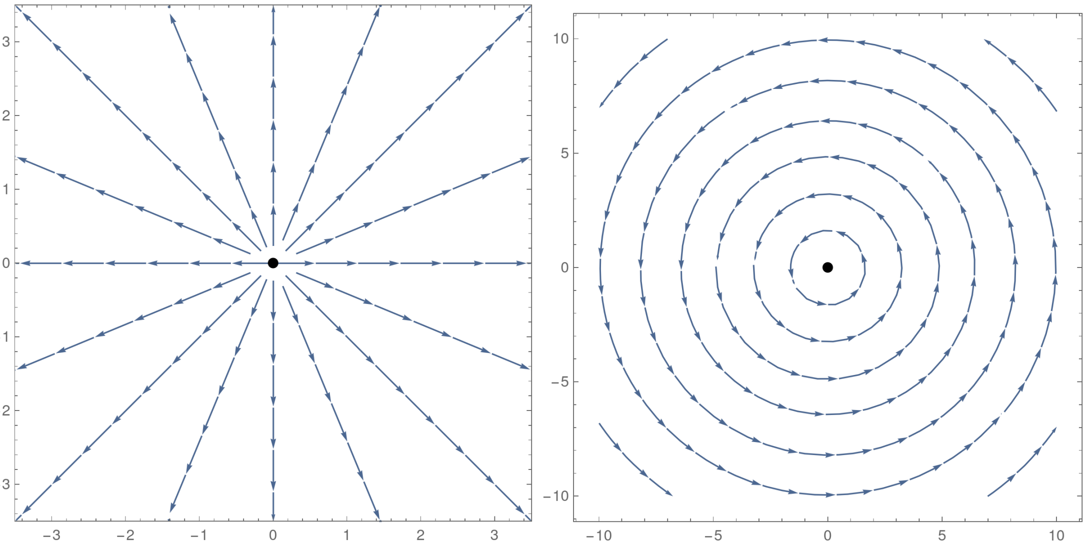

(c) aster (d) vortex

Figure 5.1: Sketches of single defect textures showing the angle ϕ_i (the phase of P_i) for (a) a +1 defect where ϕ_i is the angle between P_i and $\hat{r}$, (b) a −1 defect where $\phi_i/2$ is the angle of the separatrix. Special values of ϕ_i are shown in (c) and (d) for a +1 defect: (c) is an aster ($\phi_i = 0$), and (d) is a vortex ($\phi_i = \pi/2$).

5.4 Dynamics of active polar defects (interactions)

5.4.1 Method

We are interested in solving the following PDE:

$$\frac{\partial p}{\partial t} = \mathcal{I}(p) \tag{5.15}$$

We do so by following the variational method used in [101, 100], which we now review. We start by making the ansatz

$$p(z, \bar{z}, t) = p_0(z, \bar{z}, \{w_a(t)\}) \tag{5.16}$$

where $w_a(t)$ (perhaps infinitely many) are parameters that need to be specified. (For example, $w_a(t)$ can include the defect positions, but is not strictly limited to them.) Once specified, $w_a(t)$ are computed by minimizing the deviation of dp_0/dt from that described by the equation of motion, Eq. (5.7). In other words, we minimize the error

$$\begin{aligned} E &= \int d^2 dz d\bar{z} \left| \partial_t p(z, \bar{z}, t) - \frac{d}{dt} p_0(z, \bar{z} | \{w_a(t)\}) \right|^2 \\ &\approx \int dz d\bar{z} \left| \mathcal{I}(p_0) - \dot{w}_a \frac{\partial p_0}{\partial w_a} \right|^2 \end{aligned} \tag{5.17}$$

with respect to $\dot{w}_a$, where $\mathcal{I}$ is defined in Eq. (5.7). Of course, the goodness of our minimization depends on the ansatz and the chosen parameters w_a. We choose our ansatz to be p_0, because we know that when the defects are fixed and when $\lambda = 0$, p_0 is a good solution [183]. Specifically, we assume that the defects are far away from each other and that $\lambda \ll 1$, in which case p_0 is a quasi-static solution to Eq. (5.7). Taking into account that $\lambda \neq 0$ and the defects are not infinitely far away from each other leads to motion of the defects, and we will assume that the time-dependence of p is only through the defect positions $z_i(t)$, and that the motion is slow. In other words, we will make the ansatz

$$p(z,\bar{z},t) = p_0(z,\bar{z},\{z_i(t)\}) \tag{5.18}$$

where we have chosen $w_a(t)$ to be $z_i(t)$, the defect positions.

Doing so, one finds that [100]

$$\mathcal{M}_{ij}\dot{z}_j + \mathcal{N}_{ij}\dot{\bar{z}}_j = -\frac{\partial \mathcal{F}_0}{\partial \bar{z}_i} + \lambda \mathcal{U}_i \ , \tag{5.19}$$

where

$$\mathcal{M}_{ij} = \int d^2z[\bar{\partial}_i\bar{p}_0\partial_j p_0 + \bar{\partial}_i p_0 \partial_j \bar{p}_0] \tag{5.20}$$

$$\mathcal{N}_{ij} = \int d^2z[\bar{\partial}_i\bar{p}_0\bar{\partial}_j p_0 + \bar{\partial}_i p_0 \bar{\partial}_j \bar{p}_0] \ . \tag{5.21}$$

are the mobility matrices,

$$\mathcal{F}_0 = -2\pi \sum_{i\neq j} \sigma_i\sigma_j \ln\frac{|z_i - z_j|}{L} \ , \tag{5.22}$$

is the Coulomb free energy, and

$$\mathcal{U}_i = \int d^2z[\bar{\partial}_i\bar{p}_0\mathcal{I}_\lambda + \bar{\partial}_i p_0 \bar{\mathcal{I}}_\lambda] \ . \tag{5.23}$$

The mobility matrices $\mathcal{M}_{ij}$ and $\mathcal{N}_{ij}$ have been calculated in [100] to be

$$\mathcal{M}_{ij} \approx \pi\sigma_i\sigma_j \ln\frac{L}{r_{ij}} \tag{5.24}$$

$$\mathcal{N}_{ij} \approx 0 \ . \tag{5.25}$$

Before proceeding, we would like to emphasize that in order to determine z_i, we are doing a global fit within our ansatz that finds the z_i that minimizes the error. That is to say, although we interpret z_i as the positions of defects, z_i are simply parameters in our ansatz for the global texture that act as a proxy for the defect positions, and similarly $\dot{z}_i$ are not the true velocities of the defects. If we were interested in calculating the exact

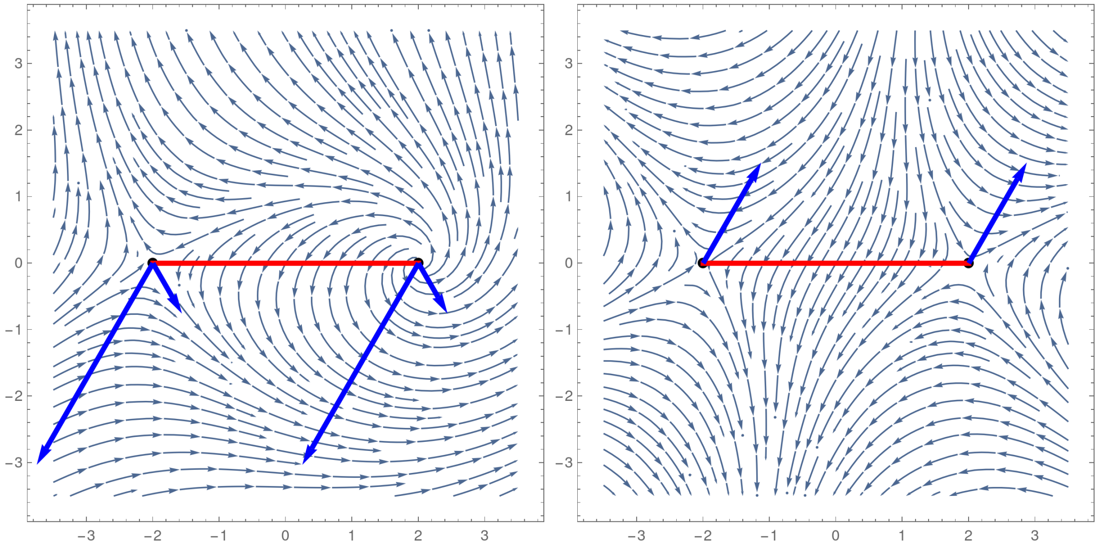

(a) -1 and $+1$ defects (b) -1 and -1 defects

Figure 5.2: Sketches of the active forces f_{ij} for $\lambda > 0$. The blue arrows denote the two components of the active force f_{ij}, and the red line joins the center of the two defects. For each pair, $f_{ij} = f_{ji}$, and the net forces are generically non-central.

defect velocities, then we could do so with a local calculation which tracks the zeros of p. However, we are interested in how p evolves everywhere, not just at specific points, which is why we minimize the error E in Eq. (5.17). Note that the fact that our equations depend on the system size L is not surprising given we are doing a global fit in a region of size L. And, we have the freedom, if we are interested, to focus on the physics in a subregion of size $\ell < L$ by minimizing Eq. (5.17) in this subregion.

5.4.2 Interactions

In Appendix B.1, we show that $\mathcal{U}_i$ (defined in Eq. (5.23)) can be explicitly written in terms of the defect positions as

$$\lambda \mathcal{U}_i = -8\pi \ln \frac{L}{a} \lambda \bar{P}_i \delta_{\sigma_i,2} + \sum_{j \neq i} f_{ij}, \tag{5.26}$$

where in terms of the unit vector $\hat{z}_{ij} = (z_i - z_j)/|z_i - z_j|$ and its complex conjugate $\hat{\bar{z}}_{ij}$,

$$f_{ij} = \frac{1}{2}\lambda\sigma_i\sigma_j\hat{z}_{ij}\left(P_i\hat{z}_{ij}^{\sigma_i-1}I_{ij}^{(1)} - \bar{P}_i\hat{\bar{z}}_{ij}^{\sigma_i-1}I_{ij}^{(2)}\right) \tag{5.27}$$

with

$$\begin{aligned} I_{++}^{(1)} &= I_{--}^{(1)} = 2\pi \\ I_{+-}^{(1)} &= I_{-+}^{(1)} = 2\pi\ln\frac{L}{r_{ij}} + \mathcal{O}(L^0) \\ I_{++}^{(2)} &= 2\pi\ln\frac{L}{r_{ij}} + \mathcal{O}(L^0); \quad I_{--}^{(2)} = 0 \\ I_{+-}^{(2)} &= I_{-+}^{(2)} = 2\pi\ . \end{aligned} \tag{5.28}$$

The first term in Eq. (5.26) is the “self-propulsion” of a +2 defect along the $\bar{P}_i$ direction, where P_i was defined in Eq. (5.14). Of course, we should not take this term too seriously, because a +2 defect can be interpreted as a bound state of two +1 defects, which is unstable because of the Coulomb repulsion. The second term in Eq (5.26) is the active induced pair-wise interaction, and its leading dependence on distance r_{ij} between two defects i and j is $\ln L/r_{ij}$.

We now examine the net force. Since $I_{ij}^{(1)} \neq I_{ij}^{(2)}$, then f_{ij} is a generic non-central force; in particular, it is also not orthogonal to the line connecting the two defects. We also comment that since $f_{ij} = f_{ji}$, then the defect pair moves together, as if it is a bound object. Another feature is that for a pair of −1 defects, there is no dependence on the distance between the defects, unlike in cases of the neutral pair or pair of +1 defects. See Fig. 5.2 and Fig. 5.3 for sketches.

We have learned that two +1 defects exert the same force on each other (same magnitude and direction), as if they’re bound. In the limit that these defects are really close to each other, then there is no reason a priori to expect that they are actually bound, as our assumptions no longer hold. However, interestingly enough, the two defects behave

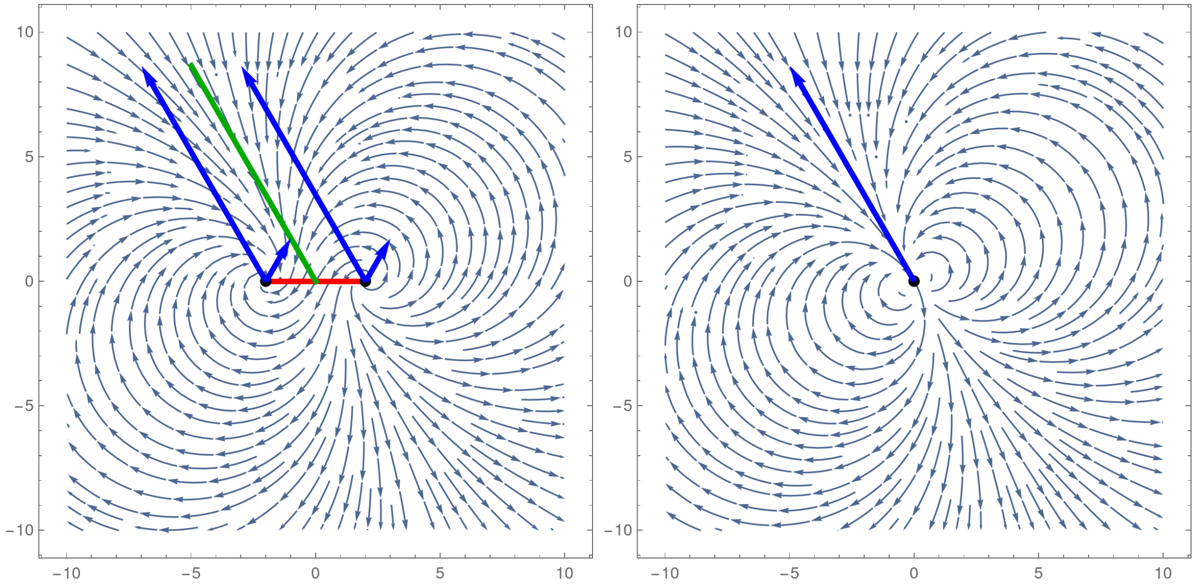

(a) Two +1 defects

(b) A single +2 defect

Figure 5.3: Sketches of active forces with $\lambda > 0$ for (a) two +1 defects, and (b), for a single +2 defect (the "self-propulsion" force). The forces for both cases are essentially in the same direction.

as if they're a +2 defect, a bound state of two +1 defects, which is "self-propelled" in the same direction, along its separatrix, consistent with the behavior of a +2 defect (see Fig. 5.3). This did not have to be the case, and does not hold for the other defect pairs.

5.5 Orientation dynamics

In the previous section, we ignored orientation dynamics. We now incorporate orientation dynamics and sketch out the argument here (the details of the computation are in Appendix B.2). For simplicity, we consider a single defect of charge σ at the origin, in which case our ansatz is

$$p_0 = e^{i\psi(t)} \left(\frac{z}{|z|} \right)^{\sigma} , \tag{5.29}$$

where now the phase $\psi(t)$ is dynamical. Choosing $w_a(t) = \psi(t)$ in Eq. 5.17 leads to

$$\int d^2 z |\frac{\partial p}{\partial \psi}|^2 \dot{\psi} = \frac{\lambda}{2} \int d^2 z \frac{\partial \bar{p}}{\partial \psi} \mathcal{I}_\lambda + c.c \tag{5.30}$$

and upon evaluation in a region of size ℓ near the defect, where $a \ll \ell \ll L$ and a is the core size,

$$\pi \ell^2 \dot{\psi} = -2\pi\lambda\ell \sin\psi \delta_{\sigma,1} \implies \dot{\psi} = -2\frac{\lambda}{\ell} \sin\psi\delta_{\sigma,1} \ . \tag{5.31}$$

Only the solution for +1 defects is nontrivial, which for completeness is given by

$$\psi(t) = 2 \operatorname{arccot} \left(\mathrm{e}^{\frac{2\lambda}{\ell}\mathrm{t}} \cot\left(\frac{\psi(0)}{2} \right) \right) \ . \tag{5.32}$$

Note that we can interpret Eq. 5.31 as relaxational dynamics

$$\dot{\psi} = -\frac{2}{\ell}\frac{dV}{d\psi} \tag{5.33}$$

for the potential $V = -\lambda \cos\psi$ (see Fig. 5.4 for a plot). Thus for $\lambda > 0$, the defect will relax to an aster ($\psi = 0$), and for $\lambda < 0$, the defect will relax to an inward-pointing aster ($\psi = \pi$).[4]. In other words, there is a preferred phase. Stable asters have been observed in related simulations [184, 185, 112, 113, 115, 107], as well as analyzed in related models [186, 187, 110, 111, 112].

---

[4] Note that there is a symmetry of our system when $\lambda \to -\lambda$ and $p \to -p$ symmetry.

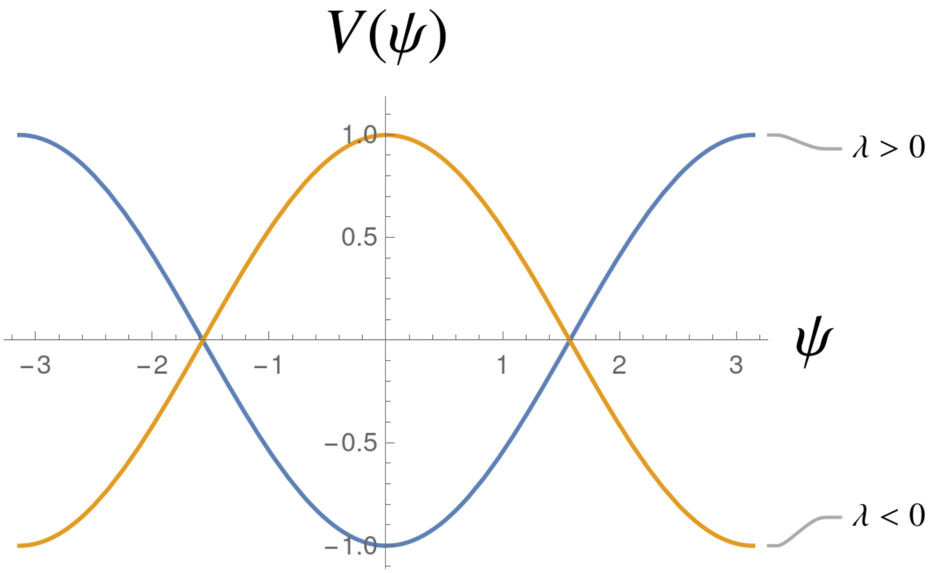

Figure 5.4: Plot of $V(\psi)$ for $\lambda > 0$ and $\lambda < 0$. Extrema are at $\psi = 0, \pi$. Minimum for $\lambda > 0$ is at $\psi = 0$, whereas minimum for $\lambda < 0$ is at $\psi = \pi$.

We also check our theory with simulations. We evolve an isolated +1 defect for nonzero $\lambda = 1$, where initially the phase $\psi(0) = \pi/2$. We computed the phase in two different ways: a local computation, which locates the +1 defect and measures the phase, and a global computation, which calculates the defect position and phase by minimizing in a region of size $\ell = 30a \ll L = 300a$ the deviation of our ansatz p_0 from the measured p_0, which is basically equivalent minimizing Eq. (5.17), as we did in deriving Eq. (5.31). We find that initially and at long times, the two different measurements of the phase agree, and even though they are not identical in the middle, they both are similar. Moreover, we checked our measured global definition of $\psi(t)$ vs that predicted from theory obtained by integrating Eq. (5.33), and find remarkable agreement (see Fig. 5.5).

Given that our method suggests that there appear to be two different stationary solutions for +1 defects (aster or inward-pointing aster, depending on the sign of λ), it raises the question whether these solutions are stationary solutions of Eq. (5.7). By inspection,

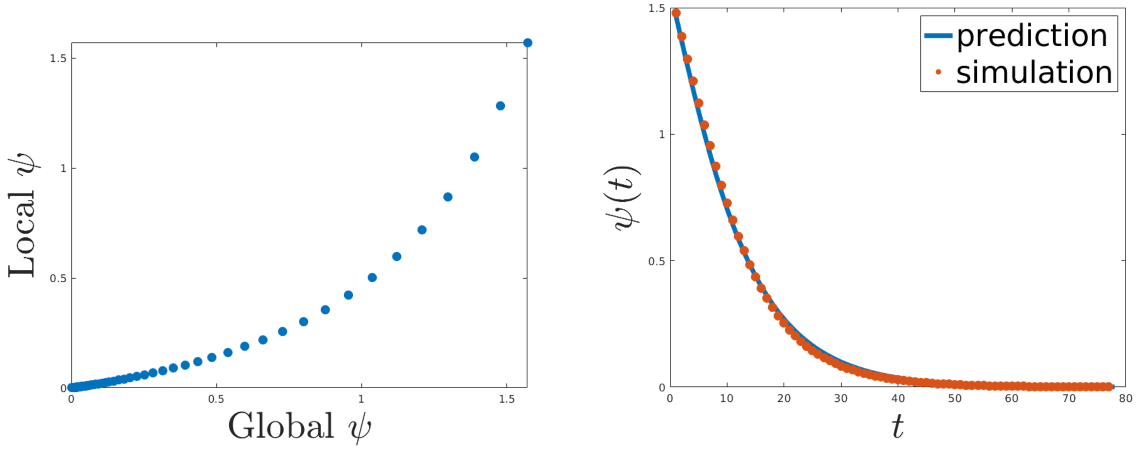

(a) +1 defect (b) −1 defect

Figure 5.5: Dynamics of the phase $\psi(t)$ of a single +1 defect for $\lambda > 0$ with $\psi(0) = \pi/2$. In (a), plot of local computation vs global computation of the phase ψ for a single +1. Their ending points are the same, but they are not identical in the middle. In (b), theoretical prediction vs simulation of $\psi(t)$.

+1 defects, in particular asters or inward-pointing asters, are indeed stationary solutions of Eq. (5.7).

Since the phase appears to be important, it is natural to ask if we can modify our ansatz in Eq. (5.18) to take into account the phase, for example by taking $\Psi_i \to e^{i\phi_i f(|z-z_i|)}\Psi_i$, where for example as in [164] $f(|z-z_i|) = e^{i\gamma_i \ln|z-z_i|}$ [5]. We leave this analysis to future work.

---

[5] We do not assume this form of f as this modified ansatz leads to an infinite free energy addition.

5.6 Stationary solution through scaling argument

In this paper, we have focused on defects. Here we make contact with the discussion contained in [109], and provide another perspective about why defects are transient in active polar fluids.

We make use of a scaling argument. By inspection, there is a scaling symmetry; that is, solutions obey[6]

$$p(z,t;\lambda) = p(z/\beta, t/\beta^2; \beta\lambda) \ . \tag{5.34}$$

We are interested in the stationary, longtime behavior, which means that we are looking for p such that for any t

$$\lim_{\gamma\to\infty} \frac{\partial}{\partial t} p(z, \gamma^2 t; \lambda) = 0 \ . \tag{5.35}$$

From our scaling relation in Eq. 5.34, choosing $\beta = \gamma$ is equivalent to finding p such that

$$\lim_{\gamma\to\infty} \frac{\partial}{\partial t} p(z/\gamma, t; \gamma\lambda) = 0 \ . \tag{5.36}$$

We thus look for steady states for large λ. For large λ, the advection term in Eq. (5.7) dominates, and thus long-time stationary states satisfy

$$\partial_t p = -\lambda(p\partial + \bar{p}\bar{\partial})p = 0 \ . \tag{5.37}$$

We will now show that the only solutions to the above equation other than constant p is a single aster or inward-pointing aster, which as we commented in Sec. 5.5 satisfies the above equation. Because we are deep in the ordered phase, our ansatz is $p = \frac{f(z)}{\bar{f}(\bar{z})}$. Then

$$\partial_t p = -\lambda(p\partial + \bar{p}\bar{\partial})p = -\frac{\lambda}{\bar{f}^2}(f\partial f - \bar{f}\bar{\partial}\bar{f}) \tag{5.38}$$

---

[6] For notational convience, we drop the explicit dependence on g. Explicitly, g scales as $p(z,t;g,\lambda) = p(z/\beta, t/\beta^2; \beta^2 g, \beta\lambda)$. Since we are in the deep nematic limit, $g \to \infty$, so it is unaffected by rescaling. But for finite g, this is how it would scale.

which vanishes only if $\partial(f^2) = c_1$, where $c_1 \in \mathbb{R}$. Therefore, $f^2 = c_1 z + c_2$, and so p is constant if $c_1 = 0$, and otherwise

$$p = e^{i\psi} \frac{(z - z_i)^{1/2}}{(\bar{z} - \bar{z}_i)^{1/2}} \tag{5.39}$$

where either $\psi = 0$ (aster) or $\psi = \pi$ (inward pointing aster), depending on the sign of λ; no other ψ is allowed. Note that this single aster stationary state is consistent with the single vortex to aster transition, as in Eq. (5.33). We have thus provided another perspective for transient behavior of defects.

5.7 Comparison with active nematics model

5.7.1 Overview

In this section, we compare our model to the active nematics model studied in [100]. We first present a general overview, and then study the consequences. The similarities are that both models advect an order parameter deep in the ordered phase and in the overdamped limit. In the case of nematic, the order parameter is a rank 2 symmetric traceless tensor $\mathbf{Q}$, and in the case of polar, the order parameter is a vector. This difference implies that there are extra terms in the advection of $\mathbf{Q}$. In the case of nematic, overdamped limit implies $\mathbf{v} = \alpha \boldsymbol{\nabla} \cdot \mathbf{Q}$, where α is a measure of activity, and in the case of polar, $\mathbf{v} = \lambda \mathbf{p}$. This difference in dependence of length scaling implies that in the nematic model, α cannot be scaled out of the problem, but in the polar model, λ can be scaled out. Although these models are different, they are similar, and by studying these models in depth it is interesting to learn which features are common and which are model-dependent.

5.7.2 Forces

We now compare the forces. In the absence of activity, the models are equivalent. The forces that arise because of activity are different. In the active nematics case, a $+1/2$ defect, the smallest allowed energy excitation, is “self-propelled”, whereas in the active polar case, a ± 1 defect, the smallest allowed energy excitation, is not “self-propelled”; a $+2$ defect is “self-propelled”. Another difference between these two models arise in the pair-wise interactions induced by activity. In the active nematics case, the active forces are central for a $(+1/2, +1/2)$ pair, and for the other pairs are orthogonal to line connecting the defects. Also, the forces for $(+1/2, -1/2)$ pair are non-reciprocal. All of

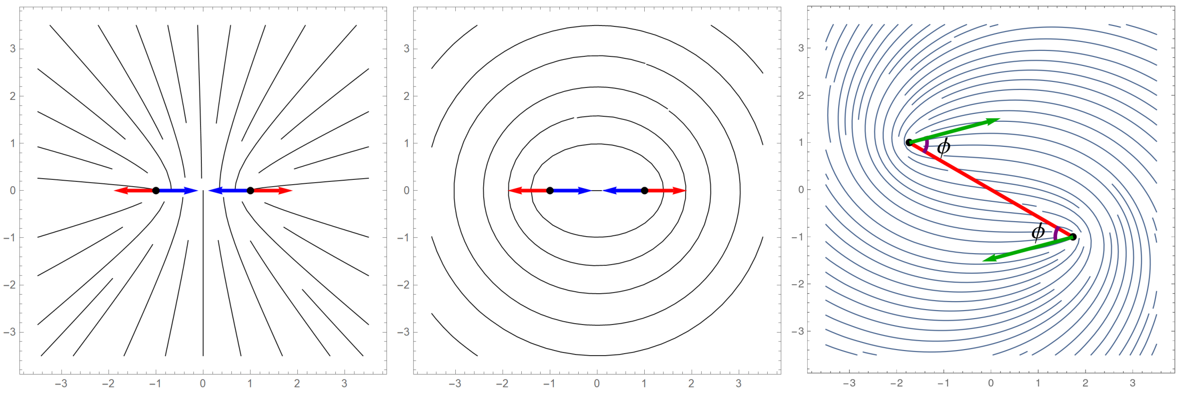

(a) Aster bound state (b) Vortex bound state (c) Spiral bound state

Figure 5.6: In active nematics model, sketches of bound state of two $+1/2$ defects. In (a), bound aster state in extensile system when $\psi = 0$, (b), bound vortex state in contractile system when $\psi = \pi$, and in (c), bound spiral state in contractile system when $0 < \psi < \pi/2$.

these forces fall off as $1/r$, where r is the distance between the defects, and the magnitude depends on the geometry, that is, overall phase of Q. In contrast, in the case of active polar, the active forces are neither central forces nor orthogonal to the line connecting the two defects. They are also always equal, and except for the -1 defect pair, goes as $\ln L/r$. Similar to active nematic, the magnitude of the force depends on the geometry, that is, the phase of p.

5.7.3 Orientation dynamics / solutions

In this paper, we learned that $+1$ asters (inward-pointing asters) are stationary solutions and that they are stable for $\lambda > 0$ ($\lambda < 0$). It is natural to ask whether in the nematic model there can be stationary $+1$ defect configurations, and does the existence of solutions, or stability, depend on the phase of the defects. We show that indeed solutions exist, and the type of solution depends on the phase of the defects.

We first check to see what happens if we incorporate orientation dynamics into the active nematics model. The active nematics model has the following equation of motion,

$$\partial_t Q = \mathcal{I}(Q) = -\frac{\delta \mathcal{F}(\{Q\})}{\delta \bar{Q}} + \alpha \mathcal{I}_\alpha(Q) \ , \tag{5.40}$$

where

$$\frac{\delta \mathcal{F}(\{Q\})}{\delta \bar{Q}} = -4\bar{\partial}\partial Q - 2\epsilon^{-2}(1 - |Q|^2)Q \tag{5.41}$$

$$\mathcal{I}_\alpha(Q) = -(\partial Q \partial Q + \bar{\partial}\bar{Q}\bar{\partial}Q) + (\partial^2 Q - \bar{\partial}^2 \bar{Q})Q \tag{5.42}$$

We work in the deep nematic limit ($\epsilon \to 0$). For simplicity, we consider a single defect of charge $\sigma = \pm 1/2$ at the origin, in which case our ansatz is

$$Q_0 = e^{i\psi(t)} \left(\frac{z}{\bar{z}}\right)^\sigma \ , \tag{5.43}$$

where now the phase $\psi(t)$ is dynamical. Minimizing the error

$$\begin{aligned} E &= \int d^2 z dz d\bar{z} \left| \partial_t Q(z, \bar{z}, t) - \frac{d}{dt} Q_0(z, \bar{z}|\psi(t)) \right|^2 \\ &\approx \int dz d\bar{z} \left| \mathcal{I}(Q_0) - \dot{\psi} \frac{\partial Q_0}{\partial \psi} \right|^2 \end{aligned} \tag{5.44}$$

with respect to $\dot{\psi}$ (the analogue of Eq. (5.17)) leads to

$$\int d^2 z |\frac{\partial Q_0}{\partial \psi}|^2 \dot{\psi} = \frac{\alpha}{2} \int d^2 z \frac{\partial \bar{Q}_0}{\partial \psi} \mathcal{I}_\alpha + c.c \tag{5.45}$$

(the analogue of Eq. (5.19)). We now evaluate both sides of this equation in a region near the defect of size ℓ. As before,

$$\int d^2 z |\frac{\partial Q_0}{\partial \psi}|^2 = \pi \ell^2 \tag{5.46}$$

We now evaluate the RHS. We have

$$\int d^2z \frac{\partial \bar{Q}_0}{\partial \psi}\mathcal{I}_\alpha + c.c = \tag{5.47}$$

$$-i\int d^2z[-\sigma^2(\frac{Q_0}{z^2} - \frac{\bar{Q}_0}{\bar{z}^2}) + \sigma(\sigma-1)(\frac{Q_0}{z^2} - \frac{\bar{Q}_0}{\bar{z}^2})] + c.c$$

$$= 0 \tag{5.48}$$

which implies that

$$\dot{\psi} = 0 \tag{5.49}$$

and we thus learn that the phase is frozen, in accordance with the expectation in [100]. Here there is no preferred orientation, unlike in the active polar case, where asters or anti-asters are preferred, depending on the sign of λ.

In related models, +1 defect states consisting of two +1/2 defects have been observed in active nematics [88, 168, 169], and in [98, 188], it was argued that the type of +1 defect was determined by the activity: asters in extensile systems, and vortices in contractile systems. This observation is related to our result of finding a stationary +1 defect in the active polar model, as we will now see. We now review and present another argument for the existence and stability of a stationary defect pair of two +1 defects in the active nematics case.

Let's consider two +1/2 defects situated on the real axis. The orientations of the +1/2 defects anti-align [163, 168, 169, 100]. For simplicity, let's assume that the orientations are along the real axis, so they either point away from each other (phase is 0), or toward each other (phase is π). There are four forces: the defect drag force, the repulsive Coulomb force, the self-propulsion, and the active induced pair-wise force. We will ignore the defect drag force and active induced pair-wise force because they renormalize the velocity and Coulomb force, respectively. In this case, for $\alpha > 0$ (contractile), the +1/2 defects move with constant velocity in the direction of their phase, and for $\alpha < 0$ (extensile), the +1/2 defects move with constant velocity in the opposite direction of their phase. Therefore, at a unique separation r_* the repulsive Coulomb force can balance the attractive self-propulsion force depending on the sign of α and the phase. The configuration is stationary for either extensile system and phase is 0 or contractile system and phase is π. In the former, the two $+1/2$ defects form a bound aster state, and in the latter, they form a bound vortex state (see Fig. 5.6). This argument was pointed out in [98, 189, 188].

Moreover, this bound state is stable to transverse fluctuations of the polarization [98]. Here we present an alternative argument. If the defects are not exactly aligned, one would naively think that the self-propulsion will cause the $+1/2$ defects to go away from each other. However, we will now show that as the defects move, the orientation readjusts in such a way that it leads to inward spiral motion of the pair of defects. From arguments presented in [100], in terms of this phase ϕ (the angle of the orientation, that is, the deviation from radial line connecting the two defects), the solution takes the form

$$Q(z,t) = e^{i\phi} \frac{z - z_i(t)}{|z - z_i(t)|} \frac{z - z_j(t)}{|z - z_j(t)|} \tag{5.50}$$

where z_i and z_j are the positions of defects i and j, respectively. The orientation $Q_i(t)$ of defect i is simply

$$Q_i(t) = e^{i\phi} \frac{z_i(t) - z_j(t)}{|z_i(t) - z_j(t)|} \tag{5.51}$$

Since $+1/2$ defects are self-propelled along their orientation, in the direction of Q_i, then they will always move at a constant angle ϕ relative to the radial line connecting the two defects. Thus for example in contractile system, if ϕ is sufficiently close to 0, and the activity is not too large, then the two defects will simply spiral towards each other (see Fig. 5.6). The solution is thus stable, but not stationary.

Given that it seems that a composite made of a pair of $+1/2$ defects is a stationary solution for the active nematic model and far away it looks like an aster or vortex, it is natural to ask if an aster or vortex is actually a solution to Eq. (5.40). By inspection,

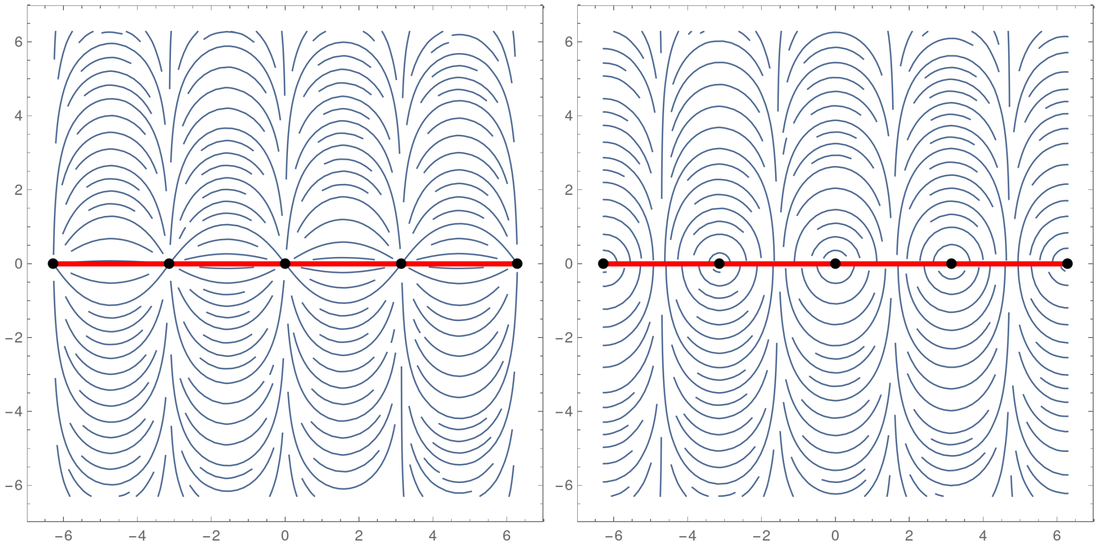

(a) Asters

(b) Vortices

Figure 5.7: Configuration of 1D chain of equally spaced +1 defects for active nematics model that screens the activity term.

indeed a nontrivial solution is $Q = \pm\frac{z}{\bar{z}}$ (as one can easily check that the active term $\mathcal{I}_\alpha = 0$), where the + sign corresponds to an aster and the − sign corresponds to a vortex. Note that this solution of aster or vortex is consistent with the picture in Fig. 5.6, as any other phase results in a non-stationary state. Thus a single aster or a vortex is indeed a stationary solution to Eq. (5.40).

Screening of activity term by +1 defects in active nematics is similar to what we found in active polar fluids. In active polar fluids, this is the only configuration which screens the active term and that is the reason for transient behavior of defects. Is this the case in active nematics or are there more general configurations that screen the active term? Or can we extend this solution to allow multiple defects? A natural place to look for this (ignoring the passive forces) is to look for configurations that screen the active term ($\mathcal{I}_\alpha = 0$), as in the case of single aster/vortex. In the polar case, a single aster was the only defect configuration that screened the active term. Here we will see that the situation (and solution) is more interesting for a nematic system.

We are thus interested in solving

$$\mathcal{I}_\alpha = 0 \; , \tag{5.52}$$

where

$$\mathcal{I}_\alpha = -\partial Q \partial Q - \bar{\partial}\bar{Q}\bar{\partial}Q + (\partial^2 Q - \bar{\partial}^2 \bar{Q})Q \tag{5.53}$$

Deep in the ordered phase, $Q = \pm e^{i(f(z)+\bar{f}(\bar{z}))}$, and so

$$iQ\left(\partial^2 f e^{2if} + \bar{\partial}^2 \bar{f} e^{-2i\bar{f}}\right) = 0 \tag{5.54}$$

Other than the constant solution, the unique solution is

$$f(z) = -i \ln \sin k(z - z_0) \tag{5.55}$$

where without loss of generality we can assume $k \in \mathbb{R}$ by rotation of z coordinate if necessary and place the origin at z_0. Therefore,

$$Q = \pm e^{i(f(z)+\bar{f}(\bar{z}))} = \pm \frac{\sin kz}{\sin k\bar{z}} \; . \tag{5.56}$$

Notice that this vanishes at $z = n\pi/k$, for $n \in \mathbb{Z}$, and near each zero, $Q \sim \pm\frac{z}{\bar{z}}$. We thus have an infinite chain of $+1$ nematic defects on the real axis, separated by π/k. Because of the sign of Q, either the defects are all asters (when the sign is positive), or the defects are all vortices (when the sign is negative). These configurations are depicted in Fig. 5.7.

Ignoring the Coulomb term, we have analytically found a stationary $1D$ lattice solution. For example, in the geometry of a thin annulus (or equivalently, long channel with periodic boundary conditions), we can imagine that the boundary condition balances the Coulomb forces. In any case, this shows that $\mathcal{I}_\alpha = 0$ has a much more interesting set of solutions than $\mathcal{I}_\lambda = 0$, and deserves further study, pointing to the importance of defects in active nematic systems as opposed to active polar systems.

Chapter 6

Defect-driven morphodynamics of active surfaces

6.1 Introduction

Morphogenesis, the origin of self-organized form in biology, results from the complex interplay of mechanical and biochemical processes. To understand the dynamics of development, we need to complement our knowledge of the molecular constituents that unify many developmental programs across species with effective, coarse-grained theories that couple flows, forces and self-regulation to generate shape and link them to testable experimental predictions. At the cellular level, there are four geometric fields– cell number, size, shape, and position–that vary in space and time that are together responsible for generating shape. In connection to the rest of this thesis, we focus on the epithelial morphogenesis of nematically ordered cells. A particularly intriguing question in this context is the role of topological defects in guiding or controlling morphogenesis, as has been uncovered in a few different systems, such as cell extrusion [68, 67], layer formation [61], and the body shape of basal marine invertebrates such as *Hydra* [72]. Here, we attempt to address the question of a minimal theory that focuses on the relaxational dynamics of the *intrinsic* geometry of active epithelial surfaces, complementing work on evolving passive surfaces that has focused on/included allowing the *induced* geometry to relax e.g. [190, 191, 192], see [128] for a recent review. In particular, we focus on the role of topological defects in determining how the intrinsic geometry of surfaces changes (Fig. 6.1), inspired by the observations in two different epithelial systems: cultured murine neural progenitor cells (NPCs) [67] which show the onset of bulges/pits or sites of cellular apoptosis as a function of defect type, and *Hydra* [72] which shows a correlation between the sign of the local Gaussian curvature and the sign of the defect, as well as correlations between the formation of tentacles and the presence of bound arrays of defects.

We model epithelial layers using the theory of active nematics. Although previously discussed in Chapter 5, the following will be important for the discussion in this chapter. Activity can induce a bound +1 defect state of two +1/2 defects, when the Coulomb repulsion balances the self-propulsion of the +1/2 defects; depending on the sign of the activity or equivalently, the orientation of the +1/2 defects [98, 188, 143], one then gets either asters or vortices (see Fig. 5.6).[7]

---

[7] As discussed in Chapter 3, there are other forces, such as collective defect drag and activity-induced pair-wise interactions, but we neglect these forces since they are subleading [100].

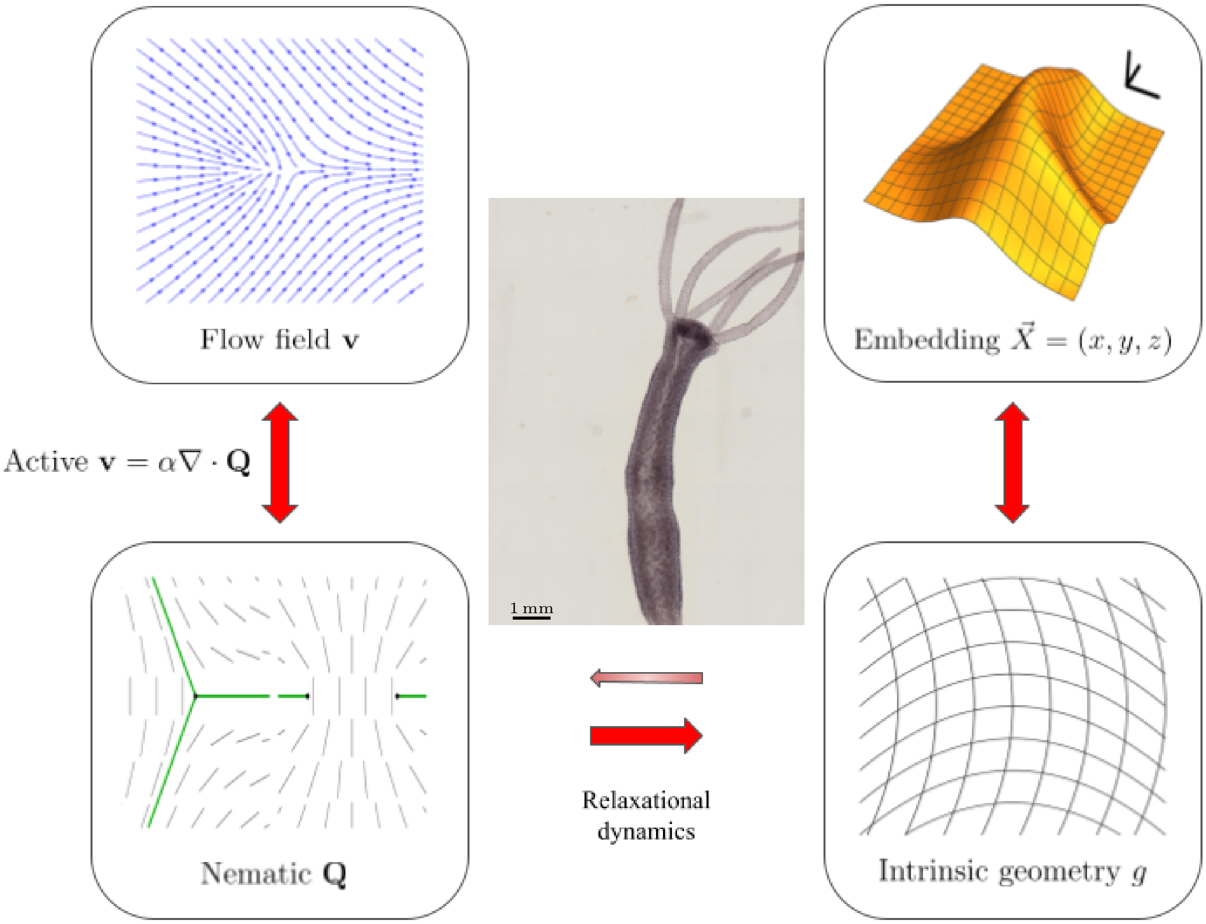

Figure 6.1: Schematic of our model. The activity through the flow field feeds into the model by stabilizing the nematic texture, and in particular the defects. The defects then induce growth and curvature for the intrinsic metric, which gets realized as the induced metric by the embedding. Image of *Hydra* in the center, adapted from [193] (approximate scale bar).

6.2 Minimal model

A minimal model that couples the relevant degrees of freedom in an active system must allow for spatio-temporal variations in the two-dimensional nematic tensor $Q^{\mu\nu}$, a velocity field v^a determined by an activity parameter which we will denote by α and which is controlled by the local nematic field, and the intrinsic 2D metric $g_{\mu\nu}$ (which can be deduced from tissue geometry), in addition to the extrinsic geometry of the sheet. For simplicity, here we will assume that the extrinsic geometry is harnessed to the intrinsic geometry, and further assume that the dynamics of the other fields are controlled by the gradient descent associated with variations in the free energy along with active flow dynamics. There are two main contributions to the free energy that we consider: (i) a contribution due to the nematic tensor $Q^{\mu\nu} = A[\hat{n}^\mu \hat{n}^\nu - \frac{1}{2}\delta^{\mu\nu}]$, where A is the magnitude of the nematic order, and $\hat{n}^\mu$ is the local director field (ii) a contribution purely due to the metric $g_{\mu\nu}$, so that the total free energy $\mathcal{F}$ is the sum of contributions from the nematic field as well as from the intrinsic metric, with $\mathcal{F} = \mathcal{F}_Q + \mathcal{F}_g$.

For the nematic order parameter, the two-dimensional Landau-de Gennes free energy [10], $\mathcal{F}_Q$, in its covariant form can be written as

$$\begin{aligned}\mathcal{F}_Q &= \int d^2x\sqrt{g}[K g_{\beta\delta}\nabla_\alpha Q^{\alpha\beta}\nabla_\gamma Q^{\gamma\delta} \\ &\qquad + \frac{1}{4}\epsilon^{-2}(1 - 4 g_{\beta\gamma} g_{\alpha\delta} Q^{\alpha\beta} Q^{\gamma\delta})^2] \\ &= \int d^2x\sqrt{g}[K\mathrm{Tr}[(\nabla\cdot Q)^2] + \frac{1}{4}\epsilon^{-2}(1 - 4\mathrm{Tr}[Q^2])^2] \qquad (6.1)\end{aligned}$$

where $g_{\mu\nu}$ is the metric and ∇_α is the covariant derivative associated with it. Here $K(>0)$ is the elasticity in the single-elastic Frank constant approximation, and the last term governs the isotropic-nematic transition, with ϵ controlling the microscopic nematic correlation length.[8]

---

[8] One can also add $\beta R \mathrm{Tr}[Q^2]$ to $\mathcal{F}_Q$, where R is the scalar curvature. This term will be generated

Inspired by the gradient dynamics of Ricci flow [194], we can write the free energy due to variations in the metric $\mathcal{F}_g$ as

$$\mathcal{F}_g = \int d^2x\sqrt{g}[K_\varphi R\varphi - \lambda], \tag{6.2}$$

where $\sqrt{g} = \exp(\varphi)$, with φ being a scalar field, $K_\varphi(> 0)$ is an elastic constant penalizing changes in the Gauss curvature R, and $\lambda = \lambda(t)$ is the term accounting for growth which we can use to enforce the condition that the surface area does not change.

Then the dynamics of the nematic and metric fields associated with gradient descent and advection by a non-equilibrium flow v^c yields

$$\partial_t Q^{\alpha\beta} = -v^c\nabla_c Q^{\alpha\beta} + [Q,\Omega]^{\alpha\beta} - \gamma_Q^{-1} g^{\alpha\mu} g^{\beta\nu}\frac{1}{\sqrt{g}}\frac{\delta\mathcal{F}}{\delta Q^{\mu\nu}} \tag{6.3}$$

$$\partial_t g_{\alpha\beta} = -(\nabla_\alpha v^c)g_{c\beta} - (\nabla_\beta v^c)g_{c\alpha} - \gamma_\varphi^{-1}\frac{1}{\sqrt{g}}\frac{\delta\mathcal{F}}{\delta g^{\alpha\beta}}\ , \tag{6.4}$$

with $\Omega_{ab} = (\nabla_a v_b - \nabla_b v_a)/2$ the vorticity, and γ_Q and γ_φ are the viscous coefficients for the dynamics of $Q^{\alpha\beta}$ and $g_{\alpha\beta}$, respectively, with units of radians^2/time.

Closure of the system (6.3)-(6.4) requires an equation for the active velocity field generated by the active stress $\sigma^{\alpha\beta}$, which we assume is proportional to $Q^{\alpha\beta}$, that is, $\sigma^{\alpha\beta} = \tilde{\alpha}Q^{\alpha\beta}$ [102, 33]. Here $\tilde{\alpha}$ has units of energy density, with $\tilde{\alpha} > 0$ ($\tilde{\alpha} < 0$) corresponding to contractile (extensile) activity. In the overdamped, biologically relevant limit, assuming that flow arises due to the balance of active forces with the substrate friction μ, we write

$$v^c = \alpha\nabla_\nu Q^{\nu c} \tag{6.5}$$

with $\alpha = \tilde{\alpha}/\mu$ being what we refer to as the activity. Equations (6.3)-(6.5) are a closed set of nonlinear partial differential equations that dictate the evolution of the nematic field $Q^{\alpha\beta}$ and the intrinsic geometry $g_{\alpha\beta}$ as a function of the activity α, when complemented

---

depending on the choice of the two Frank constants in the non-flat geometry, and for simplicity, we will ignore it for now.

by appropriate initial and boundary conditions. We note that our theory is related to but simpler than recent phase field models for active deformable shells [195, 196] that account for both the induced and the intrinsic geometry of the manifolds.

6.3 A limit of our model

To make progress in a minimal setting for epithelial morphogenesis, we choose 2D isothermal (conformal) complex coordinates z and $\bar{z}$ such that [21]

$$ds^2 = g_{z\bar{z}}dzd\bar{z} + g_{\bar{z}z}d\bar{z}dz = 2g_{z\bar{z}}|dz|^2 = e^{\varphi}|dz|^2 \tag{6.6}$$

and assume that the metric remains diagonal in these coordinates for all time. Furthermore, since the nematic tensor $Q^{\mu\nu}$ is a traceless real bivector, we can write its components $Q = Q^{zz}$, $\bar{Q} = Q^{\bar{z}\bar{z}}$, and $Q^{z\bar{z}}$, with $Q^{z\bar{z}} = 0$, and $Q = (\bar{Q})^*$. In these coordinates, $\mathcal{F}_Q$ and $\mathcal{F}_g$ take the form

$$\begin{aligned}
\mathcal{F}_Q &= \int d^2z\sqrt{g}[2Kg_{z\bar{z}}\nabla_z Q^{zz}\nabla_{\bar{z}}Q^{\bar{z}\bar{z}} + 2K'g_{z\bar{z}}\nabla_{\bar{z}}Q^{zz}\nabla_z Q^{\bar{z}\bar{z}} \\
&\quad + \frac{1}{4}\epsilon^{-2}(1 - 4g_{z\bar{z}}g_{z\bar{z}}Q^{zz}Q^{\bar{z}\bar{z}})^2] \\
&= \int d^2z\sqrt{g}[2K|\nabla_z Q|^2 + 2K'|\nabla_{\bar{z}}Q|^2 + \frac{1}{4}\epsilon^{-2}(1-4|Q|^2)^2] && (6.7) \\
\mathcal{F}_g &= \int d^2z\sqrt{g}[K_\varphi R\varphi - \lambda] && (6.8)
\end{aligned}$$

where $Q = Q^{zz}$ and $\bar{Q} = Q^{\bar{z}\bar{z}}$, $|\cdot|$ is defined in terms of the metric, the covariant derivatives used are $\nabla_z Q^{zz} = \partial Q + 2(\partial\varphi)Q$ and $\nabla_{\bar{z}}Q^{zz} = \bar{\partial}Q$, and the scalar curvature $R = -4e^{-\varphi}\partial\bar{\partial}\varphi$. We note that the asymmetry in the appearance of $\partial\varphi$ between $\nabla_z Q$ and $\nabla_{\bar{z}}$ is the underlying reason behind asymmetry in cell growth near defects: cells accumulate at positive defects and deplete at negative defects. Note that $K, K' > 0$ in order for the elastic energy to be positive.[9]

In terms of the eight independent parameters: K, K', ϵ, α, K_φ, γ_Q, γ_φ, and the system size L, we can define a number of natural length and time scales: the nematic coherence length $\xi = \sqrt{K+K'}\epsilon$, which is proportional to the defect core radius, the

---

[9] Here we have added a term $\propto |\nabla_{\bar{z}}Q|^2$ to $\mathcal{F}_Q$, which is equivalent to adding a term $\propto R|Q|^2$ to $\mathcal{F}_Q$.

geometric coherence length $\ell_\varphi = \sqrt{K_\varphi}\epsilon$, and the nematic response to curvature length $\ell_{R,Q} = \sqrt{|K-K'|}\epsilon$; and the relaxation times of Q and φ, $\tau_Q = \gamma_Q \epsilon^2$ and $\tau_\varphi = \gamma_\varphi L^2/K_\varphi$. This leads to the following dimensionless quantities: ξ/ℓ_φ, the ratio of coherence lengths for the nematic field and intrinsic geometry (< 1 because extrinsic geometry variations occur on scales large compared to the nematic defect core size); $\tau_\varphi/\tau_Q = (\gamma_\varphi/\gamma_Q)(L/\ell_\varphi)^2$ ($\gg 1$ because we assume that the long wavelength extrinsic geometry relaxes slowly compared to the local nematic order); K/K', the ratio of the two different types of nematic elastic deformations (~ 1); and $K/(\gamma_Q \alpha)$, the ratio of passive to active stresses, which can be large or small.

6.3.1 Passive

Before moving towards understanding the role of active defects in driving the intrinsic geometry of the surface, we first consider a passive nematic, when $\alpha = 0$, so that the dynamics for Q and φ in isothermal conformal coordinates can be written as

$$\gamma_Q \partial_t Q = 2K g^{z\bar{z}} \nabla_{\bar{z}} \nabla_z Q + 2K' g^{z\bar{z}} \nabla_z \nabla_{\bar{z}} Q + 2\epsilon^{-2}(1-4|Q|^2)Q \tag{6.9}$$

$$\begin{aligned}\gamma_\varphi \partial_t \varphi = &-K_\varphi R + 4K|\nabla_z Q|^2 + 4K g_{z\bar{z}}(Q\nabla_z\nabla_{\bar{z}}\bar{Q} + \bar{Q}\nabla_{\bar{z}}\nabla_z Q) - 4K'|\nabla_{\bar{z}} Q|^2 \\ &- \frac{1}{2}\epsilon^{-2}(1-4|Q|^2)(1-20|Q|^2) + \lambda,\end{aligned} \tag{6.10}$$

where the new covariant derivative terms are $\nabla_{\bar{z}}\nabla_z Q = \bar{\partial}\partial Q + 2(\bar{\partial}\partial\varphi)Q + 2\partial\varphi\bar{\partial}Q$ and $\nabla_z\nabla_{\bar{z}} Q = \partial\bar{\partial}Q$.

In the neighborhood of ±1/2 defects, we denote $\varphi^\pm$ and $Q^\pm$ as the local geometry and nematic field, respectively. If we start with a flat configuration, with $\varphi = 0$, Eq. (6.10) describing the evolution of φ in the neighborhood of a defect simplifies to

$$\begin{aligned}\gamma_\varphi \partial_t \varphi^+ &= 4K|\partial Q^+|^2 + 2K(Q^+\partial\bar{\partial}\bar{Q}^+ + \bar{Q}^+\bar{\partial}\partial Q^+) - 4K'|\bar{\partial}Q^+|^2 \\ &\quad - \frac{1}{2}\epsilon^{-2}(1-4|Q^+|^2)(1-20|Q^+|^2) + \lambda \end{aligned} \tag{6.11}$$

$$\begin{aligned}\gamma_\varphi \partial_t \varphi^- &= 4K|\partial Q^-|^2 + 2K(Q^-\partial\bar{\partial}\bar{Q}^- + \bar{Q}^-\bar{\partial}\partial Q^-) - 4K'|\bar{\partial}Q^-|^2 \\ &\quad - \frac{1}{2}\epsilon^{-2}(1-4|Q^-|^2)(1-20|Q^-|^2) + \lambda \end{aligned} \tag{6.12}$$

Now noting that $Q^+ = (Q^-)^*$ and that in the vicinity of the positive (negative) defect core $\bar{\partial}Q^+$ $(\partial Q^-) = 0$ leads to

$$\gamma_\varphi \partial_t \varphi^+ - \gamma_\varphi \partial_t \varphi^- = 4K|\partial Q^+|^2 + 4K'|\bar{\partial}Q^-|^2 > 0. \tag{6.13}$$

In the absence of net surface growth, this implies that φ will increase at a $+1/2$ defect and decrease near a $-1/2$ defect. Interpreting φ as the log of the cell density (since the Gauss curvature $R = -4e^{-\varphi}\partial\bar{\partial}\varphi$), we expect the cell density to increase (decrease) at plus (minus) defects, which means we can interpret as cells accumulating (depleting) at the defects.

In Fig. 6.2, we compare this result with observations from two different experiments. In Fig. 6.2(a) is the initial profile of φ at $t = 0$ from our analysis, showing the dynamic asymmetry between a plus and minus defect, which is consistent with the experimental observations of cell density in the vicinity of defects in murine neural progenitor epithelia [67]. In Fig. 6.2(b), we show that this asymmetry in the shape in the neighborhood of $\pm 1/2$ defects is reflected in the Gauss curvature of the surface which is positive (negative) near a plus (minus) defect, consistent with independent observations in a different experiment [72]. This correlation between the charge of the defects and the sign of the curvature is a consequence of the relaxational dynamics of the metric even in an active nematic, and as we will see later remains valid even at later (late) times.

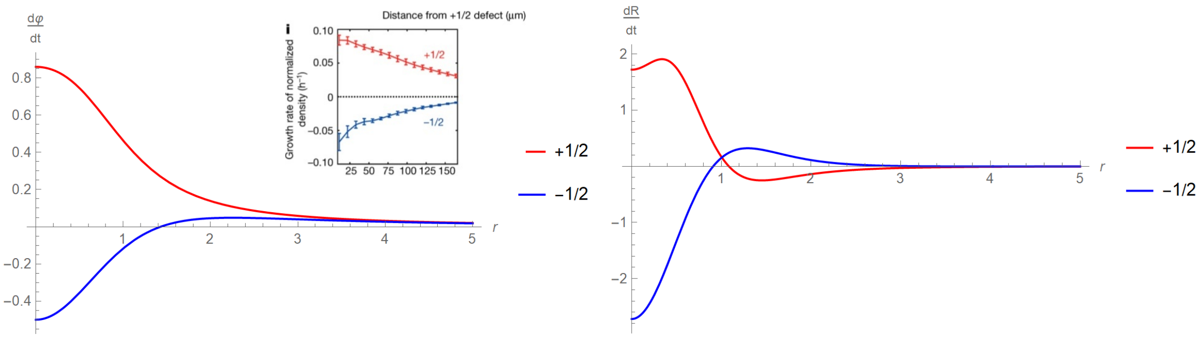

(a) (b)

Figure 6.2: Plots of (a) $\frac{d\varphi}{dt}$ and (b) $\frac{dR}{dt}$ for a single $+1/2$ (in red) and a single $-1/2$ defect (in blue) following from Eqs. (6.11)-(6.12), where $R = -4e^{-\varphi}\partial\bar{\partial}\varphi$. φ and R grow (shrink) for a $+1/2$ ($-1/2$) defect. Inset: for comparison of $\frac{d\varphi}{dt}$, corresponding figure (growth rate of normalized cell density) adapted from [67]. In both plots, parameters used are $K = 1$, $K' = 0$, and $\epsilon = 1$.

6.3.2 Active

We now turn to consider the effect of activity, i.e. $\alpha \neq 0$. In complex coordinates, $\partial_t Q \to D_t Q = \partial_t Q + v^z \nabla_z Q + v^{\bar{z}} \nabla_{\bar{z}} Q - (\nabla_z v^z - \nabla_{\bar{z}} v^{\bar{z}}) Q$ and $\partial_t \varphi \to D_t \varphi = \partial_t \varphi + \nabla_z v^z \varphi$. We are thus led to the coupled equations (6.9)- (6.10) (with this substitution $\partial_t \to D_t$), where in the over-damped, friction dominated limit,

$$v^z = \alpha \nabla_z Q = \alpha[\partial Q + 2(\partial\varphi)Q] \tag{6.14}$$

and $\nabla_z v^z = \partial_z v^z + (\partial\varphi) v^z$.

6.4 Stationary defect configuration

To solve equations (6.9)-(6.10) (with the substitution $\partial_t \to D_t$), motivated by the experimental system in [72], we use a finite-difference scheme with periodic boundary conditions to simulate a ring-like structure seen in *Hydra*. We find that an initial state, defined by a flat geometry and defect configuration of a single $+1$ defect in the center and two $-1/2$ defects on the edges, using the ansatz from [100], settles into a stationary defect configuration of a ring of equally spaced $+1$ defects (bound state of two $+1/2$ defects) separated by pairs of $-1/2$ defects in a cylindrical geometry (see Fig. 6.3(a)), similar to that observed in [72]. Activity plays a key role in stabilizing this configuration, and in particular, the $+1$ bound state is a result of balance of Coulombic repulsion force between the defects and motility (see Fig. 5.6). Indeed, the larger the activity parameter for the extensile case $\alpha < 0$, the tighter is the $+1$ bound defect. Moreover, the curvature is positive near a plus defect, and negative near a minus defect, as can be seen in Fig. 6.3(b). Plotting the profiles of $|Q|$ and φ along the vertical y-axis, we find that the peak in φ near the origin indicates outward bulging of the geometry. Moreover, the profile of $|Q|$ which is dictated by the nematic coherence length is much narrower than the width of φ along the y-axis, which is expected given that the geometric coherence length is larger than the nematic coherence length, i.e. $\ell_\varphi > \xi$ and similar to what was observed experimentally in [67] and in numerical simulations of phase field models e.g. [196].

In Fig. 6.3(d), a qualitative rendering of the shape associated with the presence of these bound states provides a simple projective view of the body plan in the neighborhood of the ring of tentacles, which we will now connect to tentacle formation in *Hydra*.

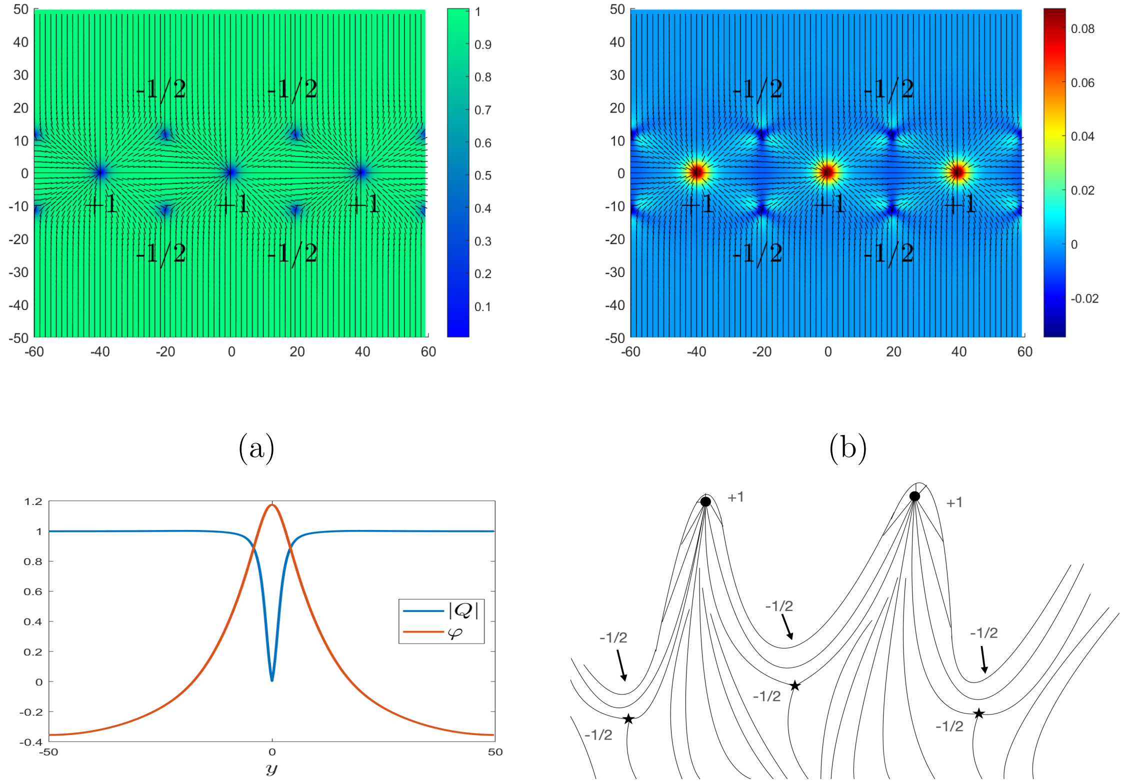

(a)

(b)

(c)

(d)

Figure 6.3: We numerically integrate equations (6.9)-(6.10) (with the substitution $\partial_t \to D_t$) to obtain steady state plots of (a) the magnitude of the nematic order parameter $|Q|$ and (b) the curvature density (given by $-4\partial\bar{\partial}\varphi$). We note that the sign of the curvature correlates with the sign of the defect, and that the defect configuration is a lattice of $+1$ bound states separated by pairs of $-1/2$ defects. In (c), we show the profile of the nematic order $|Q|$ (blue) and φ (red) along the y-axis. The profile of $|Q|$, which is dictated by the nematic coherence length, is smaller than the width of the profile of φ since $\ell_\varphi > \xi$. In (d), we sketch the geometry for the tentacle configuration from our simulation. The black dots represent $+1$ defects, the stars represent $-1/2$ defects, and black lines depict the nematic order. Three of the $-1/2$ defects are on the opposite side. Parameters for simulations: $\alpha = -0.8$, $K = 1$, $K' = 0$, $\gamma_Q = \gamma_\varphi = 1$, $K_\varphi = 4$, and $\epsilon = 2$, in terms of which $\xi = 1$, $\ell_{R,Q} = 1$, and $\ell_\varphi = 2$.

To ground these results, we turn to observations of epithelial morphogenesis in *Hydra*, a small, fresh-water basal marine invertebrate that has been a model organism for studying the dynamics of body shaping [197, 198, 72]. The tubular body of the organism consists of a bilayer of epithelial cells which contains parallel, condensed supracellular actin fibers, which align parallel to the body axis in the outer (ectoderm) layer and perpendicular to the body axis in the inner (endoderm) layer [199]. A variable number of tentacles form a ring around the body, near the head, and form when a single +1 defect is surrounded by a pair of $-1/2$ defects [72], with the sign of the curvature is correlated with the sign of the defect, consistent with our results summarized in Fig. 6.3.

But what is the actual shape of the epithelium in three dimensions? We note that knowing the intrinsic geometry does not always allow us to deduce the extrinsic geometry, but it is possible to get an approximation by numerically solving the two-dimensional Monge-Ampère equation as follows.

In terms of $X^i = (x, y, u(x, y))$, the Monge representation of the surface in 3D, the Gauss curvature R is given by

$$R(x,y) = \frac{u_{xx} \cdot u_{yy} - u_{xy}^2}{(1 + u_x^2 + u_y^2)^2} \, . \tag{6.15}$$

In terms of R, noting that $(\Delta u)^2 = u_{xx}^2 + u_{yy}^2 + 2u_{xy}^2 + 2R(1 + |\nabla u|^2)^2$ allows us to determine u for positive R by an iterative procedure,[10]

$$u^{(n+1)} = \mathcal{P}[u^{(n)}] \, , \tag{6.16}$$

where

$$\mathcal{P}[u] = \Delta^{-1} \sqrt{u_{xx}^2 + u_{yy}^2 + 2u_{xy}^2 + 2R(1 + |\nabla u|^2)^2} \, . \tag{6.17}$$

(See [200, 201, 202] and references therein for more details, and [203] and [204] are accompanying open source codes for the latter two references.) Expressing u as $u =$

---

[10] I would like to thank Xianfeng David Gu for explaining this method.

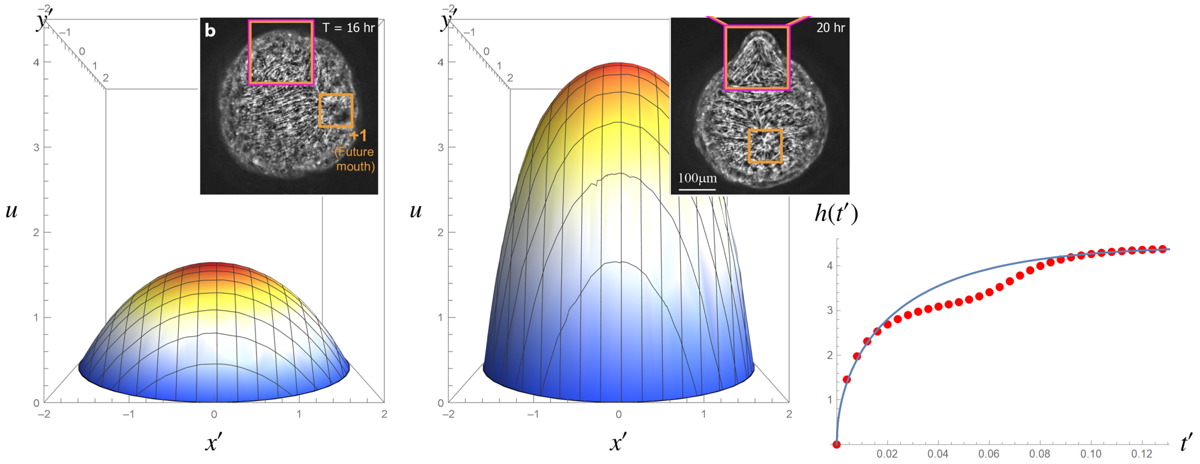

(a) $t = 0.004\tau_\varphi$ (b) $t = 0.13\tau_\varphi$ (c)

Figure 6.4: In (a) and (b): snapshots from simulations of height u of tentacle in real space near a +1 defect for early and late times, where insets (adapted from [72] are snapshots of tentacle formation near a +1 defect for early and late times. In (c), plot of the height $h(t)$ at the center of the +1 defect as a function of time t. Red points are data from simulation and blue curve is the fit $h(t) = h_0[1 - \exp(-t/\tau)]^{1/2}$, where we find that $h_0 = 4.46L$ and $\tau = 0.04\tau_\varphi$. Initially, $h(t) \propto \frac{L}{\xi}\frac{L}{\ell_\varphi}L\sqrt{\frac{t}{\tau_\varphi}}$ and $\tau \propto \tau_\varphi$. All plots use rescaled coordinates $x' = x/L$, $y' = y/L$, and $t' = t/\tau_\varphi$.

$u_0 + \delta u$, where $u_0 = \frac{\beta}{2}(x^2 + y^2)$ is our initial seed for the iterative procedure, and δu is a small correction, with β chosen so that $\beta^2 \sim R$ at the peak, we can determine u for representative times, as shown in Fig. 6.4. For our data, we did three such iterations.

Motivated by our simulations in Fig. 6.4, we now present a heuristic argument for the dynamics of budding. From Eq. (6.11), at the center of a +1 defect,

$$\partial_t \varphi^+ \sim \gamma_\varphi^{-1} K |\partial Q^+|^2 \sim \gamma_\varphi^{-1}\epsilon^{-2} = (L/\ell_\varphi)^2 \tau_\varphi^{-1} \,, \tag{6.18}$$

and so by taking the Laplacian,

$$\partial_t R \sim \gamma_\varphi^{-1} K \nabla^2 |\partial Q^+|^2 \sim (L/\ell_\varphi)^2 \tau_\varphi^{-1} \xi^{-2} \implies R \sim (L/\ell_\varphi)^2 (t/\tau_\varphi) \xi^{-2} \,. \tag{6.19}$$

Combining this with the fact that at the center of a +1 defect core, $h \propto \beta L^2$, where L is the separation between neighboring positive and negative defects, leads to

$$h^2 \propto RL^4 \propto \left(\frac{L}{\xi}\right)^2 \left(\frac{L}{\ell_\varphi}\right)^2 L^2 \frac{t}{\tau_\varphi} \ . \tag{6.20}$$

Since the nematic order is a fast variable, we can assume it settles before the (slower) geometric relaxation, the leftover dynamics is diffusive nature of the Ricci flow (essentially the heat equation), leading to $(\varphi - \varphi_{\text{eq}}) \to \exp[-t/\tau]$, where $\tau \sim \tau_\varphi$. Similarly, this leads to $(h - h_0) \to \exp[-t/\tau]$.

These asymptotics are consistent with the fit we found that we found from our simulations in Fig. 6.4,

$$h(t)^2 = h_0^2 \left(1 - e^{-t/\tau}\right) \ , \tag{6.21}$$

if we take $h_0 \sim \left(\frac{L}{\xi}\right)\left(\frac{L}{\ell_\varphi}\right) L$ and $\tau \sim \tau_\varphi$.

We thus see that the relative size of the tentacle h_0 to the average tentacle separation L is

$$\frac{h_0}{L} \sim \left(\frac{L}{\xi}\right)\left(\frac{L}{\ell_\varphi}\right) \ . \tag{6.22}$$

so that a tentacle can grow in two different ways for fixed tentacle separation (L): by decreasing either the nematic (ξ) or geometric (ℓ_φ) coherence length.

6.5 Discussion

To summarize, in this chapter we developed a minimal framework that couples the dynamics of an active nematic on a curved surface to the intrinsic geometry of the surface via relaxational dynamics. This led to three simple conclusions: (i) the sign of the curvature is correlated with the sign of the defect, (ii) cells accumulate and form mounds at positive defects and are depleted at negative defects, and (iii) a stationary ring configuration of equally spaced $+1$ defects separated by pairs of $-1/2$ defects can form. These results are consistent with experimental observations in different systems such as neural progenitor cells in-vitro and *Hydra* morphogenesis in-vivo.

A more complete description must include a complete characterization of the dynamics of embedding and the possible time-dependence of isothermal coordinates, as well as feedback on activity of the form $\alpha = \alpha(Q^{\mu\nu}, g_{\mu\nu}, \ldots)$, potential directions for future work. We expect our formalism for active nematic liquids to apply well to other examples in the context of animals where cell flow is relevant. However, we expect that in order to study the morphogenesis of plants, where cell motion is minimal [132, 205], would require a different formalism, for example, that of active nematic solids [206]. We outline some of these directions in the next (and final) chapter.

Chapter 7

Future directions

In the remainder of this thesis, we breifly review what we have found and then discuss extensions.

7.1 Summary

In this thesis, we have expanded upon the dynamics of active matter and the interactions between topological defects, and presented a simple model of morphogenesis, driven by active nematics.

In Chapter 2, we developed a coarse-grained model that demonstrated how noise can simultaneously generate both local nematic order and extensile stresses in a self-consistent manner. We thus posed a solution to the question of why generally epithelial monolayers have been observed to be extensile even though naively we would have expected them to be contractile due to the acto-myosin contractile machinery.

Having presented a model for the generation of local nematic order, we explored aspects of the dynamics of local orientational order in the remaining chapters. Starting in Chapter 3, we explored the dynamics of defects in nematic systems. Motivated by minimal energy configuration for pinned defects, we considered a multi-defect ansatz. We then used the variational principle to optimize the parameters in our ansatz (in this case, the defect velocities). We uncovered a number of novel features including: a position dependent "collective mobility matrix", the polarization being fixed by the defect positions (no longer an independent degree of freedom), and non-reciprocal and non-central active-induced interactions between defects.

In Chapter 4, we built upon this framework and considered natural extensions, including: checking the validity of our ansatz through computation of the residual error and various simulations, extending the ansatz by introducing a dynamical polarization deformation variable (so now the polarization is no longer fixed and has its own dynamics) in order so study excited states of our model (not just the ground state), formulating the continuum model, and considering other topologies and geometries, such as the torus and finite disk, which is applicable to actual experimental systems.

In Chapter 5, we applied the techniques develped in the past two chapters to polar active fluids, its cousin. Our results for polar active fluids include: non-central and non-reciprocal interactions between defects, the importance of orientational dynamics, in particular in relaxation to the single aster stationary state , and an explanation for the transient feature of active polar defects via a scaling argument. Motivated by these findings, we revisit active nematics and apply similar ideas, offering another explanation as to why vortices or asters should emerge as bound states of a pair of $+1/2$ defects, and relatedly the intriguing appearance of a stationary linear chain of equally spaced bound states of pairs of $+1/2$ defects that screen the activity.

Finally, in Chapter 6, we applied these ideas and what we have learned in active matter to the context of morphogenesis. We developed a minimal framework to study the dynamics of a curved surface, driven by active nematics. In addition to allowing the nematic order parameter to relax, we also allowed the *intrinsic* geometry to relax. Doing so led to several consequences regarding defects: (i) the sign of the curvature is correlated with the sign of the defect, (ii) cells accumulate and form mounds at positive defects and are depleted at negative defects, and (iii) a stationary ring configuration of equally spaced $+1$ defects separated by pairs of $-1/2$ defects can form. We applied this framework to study the dynamics of cells in NPCs and *Hydra*.

In the last three sections of this thesis, we discuss exciting new directions of research, corresponding to the three main research themes.

7.2 Noise-induced active nematics

Chapter 2 highlighted the key role of noise arising from subcellular active processes in mesoscopic models of tissue, something that has been little explored, opening up several future directions.

A natural question that we did not answer in Chapter 2 is what is the microscopic model? For example, we introduced a coarse-grained model, but did not specify exactly where the noise comes from or how exactly it couples to biological systems or traction forces. Continuing this theme of relation to experiments, it would be interesting to estimate the active stresses with numbers relevant to real tissues and compare to real tissues.

Cells can also coordinate their motion, leading to emergent or persistent migration. Well-known examples include the collective directed migration of follicular cells in the *Drosophila* egg-chamber [207, 208] and of epithelial cells in wound healing [209, 210]. The emergence of cell migration has been modeled in the literature by simply assuming local alignment of traction forces of adjacent cells or alignment of cell tractions with the local tissue flow, which at the continuum level, yield an instability associated with a change in the sign of the traction damping rate τ^{-1} plus a saturating cubic term, as can be derived from mesoscopic Vicsek-type models [211, 212, 181]. It would be interesting to study whether effective alignment and collective migration can be generated from noisy tractions, similar to how in our model local nematic order and extensile stress were generated.

We can also generalize this idea of noise-induced spontaneous symmetry breaking: in the classical regime (absence of noise), there was no order parameter breaking the symmetry of the system, but in the non-classical regime (presence of noise), there was an order parameter that broke the symmetry of the system by picking a preferred direction due to the noise. This can perhaps be a general mechanism in biology for generating non-trivial value of order parameter which would be interesting to study.

7.3 Multi-defect states

There are many possible and relevant extensions of the content presented in Chapters 3,4, and 5. Pertinent to these chapters is the refinement of the quasi-stationary multi-defect ansatz, first for simplicity restricted to the passive case and then generalized to the active case. For example, we know that corrections to the ansatz will include the velocity. There are two possible paths: one to attempt to formulate a perturbative scheme, and the second to improve the ansatz using intuition. Relatedly, we studied these systems in the limit of low defect density and low activity, and it would be interesting to extend our analysis to the limit of larger defect density and larger activity, where chaotic, turbulent-like behavior is observed, and in particular study the statistical mechanics of the defects. Of course, we need to develop a continuum theory in order to do this, which we have initiated and even by itself is a useful endeavor.

Both polar and apolar (antiferromagnetic) ordering of the polar $+1/2$ defects have been reported in experiments and simulations by different authors [165, 150, 213, 149, 87, 98, 168, 169]. It has been suggested that the type and range of defect order may be influenced by density fluctuations and viscous dissipation. While our model does not take these effects into account, perhaps by extending the model we can use it to determine the type and range of order. It would also be interesting to investigate more generally the possibility of ordered lattices of defects that have been reported in simulations [167] and in Chapter 6. To that end, we would need to study many-body interactions. Here, we only explicitly considered pair-wise interactions, but by turning the crank we can compute three-body interactions or even higher.

Although we have only considered active matter systems, in particular active nematics and active polar fluids and their passive counterparts, we expect our framework to be generically applicable to other systems containing defects. Lastly, here we have considered only classical systems, that is, absent of noise. Realistic biological systems are noisy, and so we should incorporate the effects of noise. We can do so for example by formulating a non-equilibrium effective action.

7.4 Morphogenesis

We now direct our attention to morphogenesis, which in some sense is an amalgation of the previous two research themes, and discuss various extensions.

7.4.1 Non-diagonal metric

Throughout Chapter 6, for simplicity, we have assumed that the metric is diagonal, meaning that the off-diagonal components remain zero. However, we know that this is not the case as $\delta\mathcal{F}/\delta g^{zz}$ and $\delta\mathcal{F}/\delta g^{\bar{z}\bar{z}}$ do not vanish. There are two possible paths towards remedying this problem. One option is to not assume that g is diagonal and to evolve each of its components. Similarly, the diagonal components of $Q^{\mu\nu}$ will also evolve. The equations now will get complicated as we cannot use any of the conformal math simplifications. Another option is to make $(z, \bar{z})$ dynamical, that is, have them evolve so that at time t the metric is diagonal in the $(z(t), \bar{z}(t))$ coordinates, which itself raises its own complications. In any case, we leave this extension to future work.

7.4.2 Embedding and the induced metric

We also need to account for the fact that our surface is embedded in three-dimensional space, and we want to have a dynamical model that explains the relation between the intrinsic g in the above model and the embedding of the two-dimensional surface. A simple way to incorporate X^i is to set the intrinsic metric equal to the induced metric, that is, assume

$$g_{\alpha\beta} = \partial_\alpha X^i \partial_\beta X^i, \tag{7.1}$$

and then vary the action with respect to X^i since now X^i is the fundamental field. Morally speaking, minimizing the action with respect to $g_{\mu\nu}$ is equivalent to minimizing the action with respect to X^i. Moreover, as long as the metric is sufficiently smooth, there is a locally isometric embedding, so using the metric should be equivalent to using the embedding as the embedding can locally be recovered from the metric [214, 215, 216]. We indirectly adopted the approach when we numerically obtained the embedding.

Another way around this problem is to introduce the following additional term to the free energy

$$F_X = \frac{T}{2} \int d^2x \sqrt{g} g^{\mu\nu} \partial_\mu X^i \partial_\nu X^i, \tag{7.2}$$

known as the Polyakov action [217] (see also [218, 219]), with T the surface tension. In the absence of $Q^{\mu\nu}$, the variation of F_X with respect to g is

$$T^X_{\mu\nu} = \frac{1}{\sqrt{g}} \frac{\delta F_X}{\delta g^{\mu\nu}} = \frac{T}{2} \left(G_{\mu\nu} - \frac{1}{2} g_{\mu\nu} g^{\alpha\beta} G_{\alpha\beta} \right) = 0 \tag{7.3}$$

where

$$G_{\alpha\beta} = \partial_\alpha X^i \partial_\beta X^i, \tag{7.4}$$

leading to

$$G_{\mu\nu} = \frac{1}{2} g_{\mu\nu} g^{\alpha\beta} G_{\alpha\beta} \tag{7.5}$$

This means that g and G are related by

$$g_{\mu\nu} = e^{\varphi} G_{\mu\nu} \tag{7.6}$$

where φ is the conformal factor. Moreover, F_X is conformal invariant, that it is, it is invariant under $g_{\mu\nu} \to e^{\varphi} g_{\mu\nu}$ where φ is conformal factor, and thus why our model introduced in Chapter 6 is unchanged as a result. This term leads to

$$\mathcal{F}_X = T \int d^2x \sqrt{G} = TA, \tag{7.7}$$

where A is the surface area. Adding $\mathcal{F}_Q$ and $\mathcal{F}_g$ to the free energy would modify Eq. (7.6) and $g_{\mu\nu}$ would no longer be directly related to the induced metric. Nonetheless, this model would still be interesting to study.

Here we have considered the simplest model and not considered explicit couplings between $Q^{\mu\nu}$ and X^i. A reasonable extension would be to consider the following term to the free energy that couples $Q^{\mu\nu}$ to X^i:

$$\mathcal{F}_{Q,X} = C \int d^2x \sqrt{g} Q^{\mu\nu} \partial_\mu X^i \partial_\nu X^i \tag{7.8}$$

Then the free energy $\mathcal{F} = \mathcal{F}[g, Q, X]$, and we would extremize $\mathcal{F}$ with respect to each of these fields. In any case, we leave the extension of how to incorporate the embedding to future work.

7.4.3 Regulation and feedback of v and other fields into activity

Here we assumed, as is standard, that the activity is constant. However, it could itself depend on the various fields in our model which regulate and feed back into the activity [128]. More precisely, we can consider $\alpha = \alpha(v^a, Q^{\mu\nu}, g_{\mu\nu}, \ldots)$. Given the complexity of biology, in particular the many degrees of freedom (perhaps even unknown), it might seem an insurmountable task to elucidate the form of α. However, that being said, recent progress has been made in fitting active polar theories by using the dynamics of constrained topological defects [220, 221].

7.4.4 Other topologies and boundary conditions

We can also consider other topologies or boundary conditions. As in the case of *Hydra*, we are interested in the topology of a sphere. If the shape is sufficiently elongated, like an ellipsoid, we can view the bulk as a cylinder, which we can model by an elongated torus, as in our simulations. Therefore, our results also apply to ellipsoidal geometries, as in the case of *Hydra*. Nevertheless, it would be interesting to consider other topologies, such as the sphere, or other boundary conditions, such as free boundary conditions, etc.

Appendix A

Computational details for Chapter 3

In this appendix, we present the details of the computations for Chapter 3.

A.1 Computation of $\mathcal{M}_{ab}$

We compute the metric tensor of the multi-defect manifold $\mathcal{M}_{ij}$ by computing the “overlaps”.

In the deep nematic limit, we can take $A = 1$:

$$\begin{aligned}\mathcal{M}_{ij} &= \textstyle\int d^2 z \frac{\sigma_j}{\bar{z}-\bar{z}_j}\frac{\sigma_i}{z-z_i} \\ &= 2\textstyle\int dz d\bar{z} \frac{\sigma_i\sigma_j}{\bar{z}[z-(z_j-z_i)]} \\ &= 2\sigma_i\sigma_j \textstyle\int_a^L \frac{dR}{R} \oint\limits_R \frac{dz}{i[z-(z_j-z_i)]} \\ &= 4\pi\sigma_i\sigma_j \textstyle\int_{|z_j-z_i|}^L \frac{dR}{R}\end{aligned} \tag{A.1}$$

so that

$$\mathcal{M}_{ij} = 4\pi\sigma_i\sigma_j \log \tfrac{L}{\max(|z_j-z_i|,a)}\ . \tag{A.2}$$

Here $a = 0.8\epsilon$, as we will see below in a more careful treatment, by accounting for the fact that near the defect core $A \neq 1$.

We can also calculate $\mathcal{N}_{ij}$, which is given by

$$\mathcal{N}_{ij} = -2\int d^2 z \frac{\sigma_i\sigma_j}{(\bar{z}-\bar{z}_i)(\bar{z}-\bar{z}_j)}\ . \tag{A.3}$$

We first note that for $i = j$, $\mathcal{N}_{ii}$ vanishes due to the phase integral. Thus below we assume $i \neq j$.

Shifting $z \to z + z_j$ and then rescaling $z \to z_{ij}z$, we have

$$\mathcal{N}_{ij} = -2\int d^2 z \frac{\sigma_i}{\bar{z}-\bar{z}_{ij}}\frac{\sigma_j}{\bar{z}} = 2\sigma_i\sigma_j\frac{z_{ij}}{\bar{z}_{ij}}\int \frac{dz d\bar{z}}{\bar{z}(1-\bar{z})}\ . \tag{A.4}$$

Splitting the region of integration to $|z| < 1$, and $|z| > 1$, and analytically expanding the integrand near $z = 0$ (for $|z| < 1$) and $z = \infty$ (for $|z| > 1$) yields

$$\mathcal{N}_{ij} = 2\pi\sigma_i\sigma_j\frac{z_{ij}}{\bar{z}_{ij}}\ . \tag{A.5}$$

Since we're interested in the large L limit, $|\mathcal{M}_{ij}| \gg |\mathcal{N}_{ij}|$, and thus in this paper we will ignore $\mathcal{N}_{ij}$ and set $\mathcal{N}_{ij} = 0$.

We now consider a more careful treatment of the core for $\mathcal{M}_{ii}$. In order to compute $\mathcal{M}_{ii}$, we need to take into account the fact that near defect cores, $A \neq 1$ [104, 5]. We have

$$\begin{aligned}\mathcal{M}_{ii} &= \int d^2z A^2 \left(-\bar{\partial} \ln A_i - \frac{\sigma_i}{\bar{z} - \bar{z}_i}\right) \left(-\partial \ln A_i - \frac{\sigma_i}{z - z_i}\right) \\ &\quad + \int d^2z A^2 \left(-\bar{\partial} \ln A_i + \frac{\sigma_i}{\bar{z} - \bar{z}_i}\right) \left(-\partial \ln A_i + \frac{\sigma_i}{z - z_i}\right) \\ &= 2 \int d^2z A^2 \left[|\partial \ln A_i|^2 + \frac{\sigma_i^2}{|z - z_i|^2}\right] \\ &= \int d^2z \frac{1}{2}(A')^2 + 2\sigma_i^2 \int d^2z \frac{A^2}{|z - z_i|^2} \\ &= 4\pi\sigma_i^2 \ln \frac{L}{a} \ ,\end{aligned} \tag{A.6}$$

where $a \approx 0.8\epsilon$ (using the approximate solution for A in Eq. (1.9)).

A.2 Computation of $\mathcal{U}_i$

In this appendix, we compute $\mathcal{U}_i$ (Eq. 3.47), from Chapter 3. We are interested in computing

$$\mathcal{U}_i = \int d^2z \bar{\partial}_i \bar{Q} \mathcal{I}_\alpha + \int d^2z \bar{\partial}_i Q \bar{\mathcal{I}}_\alpha = I_1 + I_2 \ , \tag{A.7}$$

where

$$I_1 = \int d^2z \bar{\partial}_i \bar{Q}[Q\partial^2 Q - (\partial Q)^2] - \int d^2z \bar{\partial}_i Q[\bar{Q}\partial^2 Q + \partial Q \partial \bar{Q}] \tag{A.8}$$

$$I_2 = \int d^2z \bar{\partial}_i Q[\bar{Q}\bar{\partial}^2 \bar{Q} - (\bar{\partial}\bar{Q})^2] - \int d^2z \bar{\partial}_i \bar{Q}[Q\bar{\partial}^2 \bar{Q} + \bar{\partial}\bar{Q}\bar{\partial}Q] \ . \tag{A.9}$$

We compute I_1 and I_2 in order.

A.2.1 Computation of I_1

Here we assume that $A = 1$, as is the case in the deep nematic limit. A more careful treatment can be found later in this appendix.

We first note that

$$Q_0\partial^2 Q_0 - (\partial Q_0)^2 = -Q_0^2 \sum_j \frac{\sigma_j}{(z - z_j)^2} \tag{A.10}$$

$$\bar{Q}_0\partial^2 Q_0 + \partial Q_0 \partial \bar{Q}_0 = -\sum_j \frac{\sigma_j}{(z - z_j)^2} \ . \tag{A.11}$$

Then

$$\begin{aligned} &\bar{\partial}_i \bar{Q}_0(Q_0\partial^2 Q_0 - (\partial Q_0)^2) - \bar{\partial}_i Q_0(\bar{Q}_0\partial^2 Q_0 + \partial Q_0 \partial \bar{Q}_0) = \\ &2Q_0 \frac{\sigma_i}{\bar{z} - \bar{z}_i} \sum_j \frac{\sigma_j}{(z - z_j)^2} \ . \end{aligned} \tag{A.12}$$

Therefore,

$$I_1 \approx 2 \int d^2z Q_0 \frac{\sigma_i}{\bar{z} - \bar{z}_i} \sum_j \frac{\sigma_j}{(z - z_j)^2} \ . \tag{A.13}$$

We can write

$$I_1 = I_{\text{leading}} + I_{\text{sub}} \ , \tag{A.14}$$

where

$$I_{\text{leading}} = 2\int d^2 z Q_0 \frac{\sigma_i^2}{|z-z_i|^2}\frac{1}{z-z_i} \tag{A.15}$$

$$I_{\text{sub}} = 2\int d^2 z Q_0 \frac{\sigma_i}{\bar{z}-\bar{z}_i}\sum_{j\neq i}\frac{\sigma_j}{(z-z_j)^2} \ . \tag{A.16}$$

We explicitly compute and find that

$$I_{\text{leading}} = 4\pi\sigma_i^2 \alpha Q_i \delta_{2\sigma_i,1}\int dr \frac{1}{r^2} = 4\pi\sigma_i^2\frac{\alpha}{a}Q_i\delta_{2\sigma_i,1} \ , \tag{A.17}$$

where

$$Q_i = \prod_{j\neq i}\frac{(z_i-z_j)^{\sigma_j}}{(\bar{z}_i-\bar{z}_j)^{\sigma_j}} \ . \tag{A.18}$$

We will see later in the subsection of this appendix that a more careful treatment again yields $a \approx 0.8\epsilon$.

We now compute the subleading term I_{sub}:

$$I_{\text{sub}} \approx \sigma_i\sigma_j Q_{ij}\int d^2 z \frac{(z-z_i)^{\sigma_i}}{(\bar{z}-\bar{z}_i)^{\sigma_i}} \ \frac{(z-z_j)^{\sigma_j}}{(\bar{z}-\bar{z}_j)^{\sigma_j}}\frac{1}{\bar{z}-\bar{z}_i}\frac{1}{(z-z_j)^2} \ , \tag{A.19}$$

where

$$Q_{ij} = \prod_{r\neq i,j}\frac{(z_i-z_r)^{\sigma_r}}{(\bar{z}_i-\bar{z}_r)^{\sigma_r}} \ . \tag{A.20}$$

Shifting $z \to z + z_j$, we have

$$I_{\text{sub}} \approx \sigma_i\sigma_j Q_{ij}\int d^2 z \frac{(z-z_{ij})^{\sigma_i}}{(\bar{z}-\bar{z}_{ij})^{\sigma_i}} \ \frac{z^{\sigma_j}}{\bar{z}^{\sigma_j}}\frac{1}{\bar{z}-\bar{z}_{ij}}\frac{1}{z^2} \ . \tag{A.21}$$

Rescaling $z \to z_{ij}z$, we have

$$I_{\text{sub}} = \sigma_i\sigma_j q_{ij}\frac{I_{ij}^{(1)}}{\bar{z}_{ij}} \ , \tag{A.22}$$

where

$$q_{ij} = Q_i \hat{z}_{ij}^{2(\sigma_i - 1)} \tag{A.23}$$

$$I_{ij}^{(1)} = \int d^2 z \frac{(z-1)^{\sigma_i}}{(\bar{z}-1)^{\sigma_i}} \frac{z^{\sigma_j}}{\bar{z}^{\sigma_j}} \frac{1}{\bar{z}-1} \frac{1}{z^2} \; . \tag{A.24}$$

We'll now outline how to compute $I_{ij}^{(1)}$. We first make the change of variables

$$w^2 = \frac{z}{z-1} \; . \tag{A.25}$$

Then we split the region of integration to $|w| < 1$, and $|w| > 1$, and finally, we analytically expand the integrand near $w = 0$ and $w = \infty$. Noting that $I_{ij}^{(1)}$ vanishes unless the powers of w and $\bar{w}$ are equal yields

$$I_{ij}^{(1)} = (-1)^{\delta_{\sigma_i + \sigma_j, 1}} \frac{\pi}{1 - \sigma_j} \; . \tag{A.26}$$

We want to remark that this expression is valid for $(\sigma_i, \sigma_j) = (\pm 1/2, \pm 1/2)$.

A.2.2 Computation of I_2

We first note that

$$Q_0 \bar{\partial}^2 \bar{Q}_0 + \bar{\partial} \bar{Q}_0 \bar{\partial} Q_0 = -\sum_j \frac{\sigma_j}{(\bar{z} - \bar{z}_j)^2} \tag{A.27}$$

$$\bar{Q}_0 \bar{\partial}^2 \bar{Q}_0 - (\bar{\partial} \bar{Q}_0)^2 = -\bar{Q}_0^2 \sum_j \frac{\sigma_j}{(\bar{z} - \bar{z}_j)^2} \; . \tag{A.28}$$

Then

$$\begin{aligned} &- \bar{\partial}_i \bar{Q}_0 [Q_0 \bar{\partial}^2 \bar{Q}_0 + \bar{\partial} \bar{Q}_0 \bar{\partial} Q_0] + \bar{\partial}_i Q_0 [\bar{Q}_0 \bar{\partial}^2 \bar{Q}_0 - (\bar{\partial} \bar{Q}_0)^2] = \\ &- 2 \bar{Q}_0 \frac{\sigma_i}{\bar{z} - \bar{z}_i} \sum_j \frac{\sigma_j}{(\bar{z} - \bar{z}_j)^2} \; . \end{aligned} \tag{A.29}$$

Therefore

$$I_2 = -2 \int d^2 z \bar{Q}_0 \frac{\sigma_i}{\bar{z} - \bar{z}_i} \sum_j \frac{\sigma_j}{(\bar{z} - \bar{z}_j)^2} \; . \tag{A.30}$$

We now compute I_2:

$$I_2 \approx -\sigma_i\sigma_j\bar{Q}_{ij}\int d^2z\frac{(\bar{z}-\bar{z}_i)^{\sigma_i}}{(z-z_i)^{\sigma_i}}\,\frac{(\bar{z}-\bar{z}_j)^{\sigma_j}}{(z-z_j)^{\sigma_j}}\frac{1}{\bar{z}-\bar{z}_i}\frac{1}{(\bar{z}-\bar{z}_j)^2}\ . \tag{A.31}$$

Shifting $z \to z + z_j$, we have

$$I_2 = -\sigma_i\sigma_j\bar{Q}_{ij}\int d^2z\frac{(\bar{z}-\bar{z}_{ij})^{\sigma_i}}{(z-z_{ij})^{\sigma_i}}\,\frac{\bar{z}^{\sigma_j}}{z^{\sigma_j}}\frac{1}{\bar{z}-\bar{z}_{ij}}\frac{1}{\bar{z}^2}\ . \tag{A.32}$$

Rescaling $z \to z_{ij}z$, we have

$$I_2 = -\sigma_i\sigma_j\bar{q}_{ij}\frac{I^{(2)}_{ij}}{\bar{z}_{ij}}\ , \tag{A.33}$$

where

$$I^{(2)}_{ij} = \int d^2z\frac{(\bar{z}-1)^{\sigma_i}}{(z-1)^{\sigma_i}}\frac{\bar{z}^{\sigma_j}}{z^{\sigma_j}}\frac{1}{\bar{z}-1}\frac{1}{\bar{z}^2}\ . \tag{A.34}$$

To compute $I^{(2)}_{ij}$, we use the same method that we used to compute $I^{(1)}_{ij}$. Doing so yields

$$I^{(2)}_{ij} = \frac{\pi}{1-\sigma_j}\ . \tag{A.35}$$

Note that $|I^{(1)}_{ij}| = |I^{(2)}_{ij}|$, and the sign differs only when $\sigma_i + \sigma_j = 1$.

A.2.3 A more careful treatment of the cores for I_{leading}

In order to quantify a in the leading contribution, we need to take into account the deviation of A away from 1 near the defect cores. Doing so yields

$$\begin{aligned} I_{\text{leading}} = 2\int d^2zQ_0A^2\Bigg[&\frac{\sigma_i^2}{|z-z_i|^2}\frac{1}{z-z_i} - \frac{\sigma_i}{\bar{z}-\bar{z}_i}\partial^2\ln A_i \\ &+|\partial\ln A_i|^2\partial\ln A_i - \frac{\sigma_i}{\bar{z}-\bar{z}_i}(\partial\ln A_i)^2 \\ &-\frac{\sigma_i^2}{|z-z_i|^2}\partial\ln A_i + |\partial\ln A_i|^2\frac{\sigma_i}{z-z_i}\Bigg]\ . \end{aligned} \tag{A.36}$$

We first compute I_{leading} by computing each term separately:

$$\begin{aligned}&-2\int d^2zQ_0A^2\frac{\sigma_i}{\bar{z}-\bar{z}_i}\partial^2\ln A_i\\ &\quad=-\pi\sigma_i\delta_{2\sigma_i,1}Q_i\int drA\left[AA''-(A')^2-\frac{AA'}{r}\right]\end{aligned} \tag{A.37}$$

$$2\int d^2zQ_0A^2\frac{\sigma_i^2}{|z-z_i|^2}\frac{1}{z-z_i}=4\pi\sigma_i^2\delta_{2\sigma_i,1}Q_i\int dr\frac{A^3}{r^2} \tag{A.38}$$

$$2\int d^2zQ_0A^2|\partial\ln A_i|^2\partial\ln A_i=\frac{1}{2}\pi\delta_{2\sigma_i,1}Q_i\int drr(A')^3 \tag{A.39}$$

$$-2\int d^2zQ_0A^2\frac{\sigma_i}{\bar{z}-\bar{z}_i}(\partial\ln A_i)^2=-\pi\sigma_i\delta_{2\sigma_i,1}Q_i\int drA(A')^2 \tag{A.40}$$

$$-2\int d^2zQ_0A^2\frac{\sigma_i^2}{|z-z_i|^2}\partial\ln A_i=-2\pi\sigma_i^2\delta_{2\sigma_i,1}Q_i\int dr\frac{A^2A'}{r} \tag{A.41}$$

$$2\int d^2zQ_0A^2|\partial\ln A_i|^2\frac{\sigma_i}{z-z_i}=\pi\sigma_i\delta_{2\sigma_i,1}Q_i\int drA(A')^2\ . \tag{A.42}$$

Combining all of these terms and computing, we find that

$$\begin{aligned}&I_{\text{leading}}\approx\\ &\quad 2\pi\sigma_i^2\alpha Q_i\delta_{2\sigma_i,1}\int dr\left[-A^2A''+A(A')^2+\frac{2A^3}{r^2}+r(A')^3\right]\\ &\quad\approx 4\pi\sigma_i^2\frac{\alpha}{a}Q_i\delta_{2\sigma_i,1}\ ,\end{aligned} \tag{A.43}$$

where $a\approx 0.8\epsilon$ (using the approximate solution for A in Eq. (**??**)).

Appendix B

Computational details for Chapter 5

B.1 Computation of $\mathcal{U}_i$

In this chapter, we compute $\mathcal{U}_i$ (Eq. (5.23)), from Chapter 5. We are interested in computing

$$\mathcal{U}_i = \int d^2z \bar{\partial}_i \bar{p}_0 \mathcal{I}_\lambda + \int d^2z \bar{\partial}_i p_0 \bar{\mathcal{I}}_\lambda = I_1 + I_2 \ , \tag{B.1}$$

where

$$I_1 = -\int d^2z \bar{\partial}_i \bar{p}_0 p_0 \partial p_0 - \int d^2z \bar{\partial}_i p_0 p_0 \partial \bar{p}_0 \tag{B.2}$$

$$I_2 = -\int d^2z \bar{\partial}_i p_0 \bar{p}_0 \bar{\partial} \bar{p}_0 - \int d^2z \bar{\partial}_i \bar{p}_0 \bar{p}_0 \bar{\partial} p_0 \ . \tag{B.3}$$

Substituting for p_0, we find that

$$I_1 = \frac{1}{2} \sum_j \int d^2z p_0 \frac{\sigma_i \sigma_j}{(\bar{z} - \bar{z}_i)(z - z_j)} \tag{B.4}$$

$$I_2 = -\frac{1}{2} \sum_j \int d^2z \bar{p}_0 \frac{\sigma_i \sigma_j}{(\bar{z} - \bar{z}_i)(\bar{z} - \bar{z}_j)} \tag{B.5}$$

It is convenient to rewrite the above as

$$I_1 = \frac{1}{2}\int d^2z p_0 \frac{\sigma_i^2}{|z-z_i|^2} + \frac{1}{2}\sum_{j\neq i}\int d^2 z p_0 \frac{\sigma_i\sigma_j}{(\bar{z}-\bar{z}_i)(z-z_j)} \tag{B.6}$$

$$I_2 = -\frac{1}{2}\int d^2z \bar{p}_0 \frac{\sigma_i^2}{(\bar{z}-\bar{z}_i)^2} - \frac{1}{2}\sum_{j\neq i}\int d^2 z \bar{p}_0 \frac{\sigma_i\sigma_j}{(\bar{z}-\bar{z}_i)(\bar{z}-\bar{z}_j)} \tag{B.7}$$

The first term for I_1 vanishes by phase integral. The first term for I_2 is only non-zero for $\sigma_i = 2$, in which case (since we are assuming that defects are well-separated), we can approximate

$$\begin{aligned} -\frac{1}{2}\int d^2z\bar{p}_0\frac{\sigma_i^2}{(\bar{z}-\bar{z}_i)^2} &\approx -\delta_{\sigma_i,2}\frac{1}{2}\bar{P}_i\int d^2z\frac{(\bar{z}-\bar{z}_i)^2}{|z-z_i|^2}\frac{4}{(\bar{z}-\bar{z}_i)^2} \\ &= -8\pi\bar{P}_i\delta_{\sigma_i,2}\ln\frac{L}{a} \end{aligned} \tag{B.8}$$

which we can identify as the self-propulsion of a +2 defect. In the following, we will explicitly be assuming that $\sigma_i = \pm 1$, so this term does not appear. Thus we can write

$$I_1 \approx \frac{1}{2}\sum_j P_{ij}\int d^2z\frac{(z-z_i)^{\sigma_i}}{|z-z_i|^{\sigma_i}}\frac{(z-z_j)^{\sigma_j}}{|z-z_j|^{\sigma_j}}\frac{\sigma_i\sigma_j}{(\bar{z}-\bar{z}_i)(z-z_j)} \tag{B.9}$$

$$I_2 \approx -\frac{1}{2}\sum_j \bar{P}_{ij}\int d^2z\frac{(\bar{z}-\bar{z}_i)^{\sigma_i}}{|z-z_i|^{\sigma_i}}\frac{(\bar{z}-\bar{z}_j)^{\sigma_j}}{|z-z_j|^{\sigma_j}}\frac{\sigma_i\sigma_j}{(\bar{z}-\bar{z}_i)(\bar{z}-\bar{z}_j)}\ , \tag{B.10}$$

where

$$P_{ij} = \prod_{r\neq i,j}\frac{(z_i-z_r)^{\sigma_r}}{|z_i-z_r|^{\sigma_r}}\ . \tag{B.11}$$

First shifting $z \to z + z_j$ and then rescaling $z \to z_{ij}z$, we have

$$I_1 = \frac{1}{2}\sum_j \sigma_i\sigma_j P_{ij}\left(\frac{z_{ij}}{|z_{ij}|}\right)^{\sigma_i+\sigma_j} I_{ij}^{(1)} \tag{B.12}$$

$$I_2 = -\frac{1}{2}\sum_j \sigma_i\sigma_j \bar{P}_{ij}\left(\frac{\bar{z}_{ij}}{|z_{ij}|}\right)^{\sigma_i+\sigma_j-2} I_{ij}^{(2)} \tag{B.13}$$

where

$$I_{ij}^{(1)} = \int d^2z\frac{(z-1)^{\sigma_i}}{|z-1|^{\sigma_i}}\frac{z^{\sigma_j}}{|z|^{\sigma_j}}\frac{1}{\bar{z}-1}\frac{1}{z} \tag{B.14}$$

$$I_{ij}^{(2)} = \int d^2z\frac{(\bar{z}-1)^{\sigma_i}}{|z-1|^{\sigma_i}}\frac{\bar{z}^{\sigma_j}}{|z|^{\sigma_j}}\frac{1}{\bar{z}-1}\frac{1}{\bar{z}} \tag{B.15}$$

are integrals that need to be computed. For notation, let $+(-)$ index denote plus (minus) defect. Using techniques utilized in [100], we find that

$$\begin{aligned}
I^{(1)}_{++} &= I^{(1)}_{--} = 2\pi \\
I^{(1)}_{+-} &= I^{(1)}_{-+} = 2\pi \ln \frac{L}{r_{ij}} + \mathcal{O}(L^0) \\
I^{(2)}_{++} &= 2\pi \ln \frac{L}{r_{ij}} + \mathcal{O}(L^0); \quad I^{(2)}_{--} = 0 \\
I^{(2)}_{+-} &= I^{(2)}_{-+} = 2\pi
\end{aligned} \tag{B.16}$$

To summarize, $\mathcal{U}_i$ can be written explicitly in terms of the defect positions as

$$\lambda \mathcal{U}_i = -8\pi \ln \frac{L}{a} \lambda \bar{P}_i \delta_{\sigma_i,2} + \sum_{j \neq i} f_{ij}, \tag{B.17}$$

where

$$f_{ij} = \frac{1}{2}\sigma_i \sigma_j \left(P_{ij} \hat{z}_{ij}^{\sigma_i+\sigma_j} I^{(1)}_{ij} - \bar{P}_{ij} \hat{\bar{z}}_{ij}^{\sigma_i+\sigma_j-2} I^{(2)}_{ij} \right) \tag{B.18}$$

can be interpreted as the active induced pair-wise force on defect i due to defect j. f_{ij} can be rewritten as

$$f_{ij} = \frac{1}{2}\sigma_i \sigma_j \hat{z}_{ij} \left(P_{ij} \hat{z}_{ij}^{\sigma_i+\sigma_j-1} I^{(1)}_{ij} - \bar{P}_{ij} \hat{\bar{z}}_{ij}^{\sigma_i+\sigma_j-1} I^{(2)}_{ij} \right) \tag{B.19}$$

or equivalently as

$$f_{ij} = \frac{1}{2}\sigma_i \sigma_j \hat{z}_{ij} \left(P_i \hat{z}_{ij}^{\sigma_i-1} I^{(1)}_{ij} - \bar{P}_i \hat{\bar{z}}_{ij}^{\sigma_i-1} I^{(2)}_{ij} \right) \tag{B.20}$$

B.2 Orientation dynamics computations

In this Appendix, we derive the orientation dynamics (Eq. (5.31)), for Chapter 5

For simplicity, we consider a single defect of charge σ at the origin, in which case our ansatz is

$$p_0 = e^{i\psi(t)} \left(\frac{z}{|z|}\right)^{\sigma} , \tag{B.21}$$

where now the phase $\psi(t)$ is dynamical. Choosing $w_a(t) = \psi(t)$ in Eq. (5.17) leads to

$$\int d^2z |\frac{\partial p_0}{\partial \psi}|^2 \dot{\psi} = \frac{\lambda}{2} \int d^2z \frac{\partial \bar{p}_0}{\partial \psi} \mathcal{I}_\lambda(p_0) + c.c, \tag{B.22}$$

where the Coulomb term vanishes because there is only one defect. We now evaluation both sides of the above equation in a region of size ℓ near the defect, where $a \ll \ell \ll L$ and a is the core size. We first evaluate the LHS. Since $|\frac{\partial p_0}{\partial \psi}| = 1$, then

$$\int d^2z |\frac{\partial p_0}{\partial \psi}|^2 = \pi \ell^2 . \tag{B.23}$$

We now evaluate the RHS. We have

$$\begin{aligned} \frac{\lambda}{2} \int d^2z \frac{\partial \bar{p}_0}{\partial \psi} \mathcal{I}_\lambda(p_0) + c.c &= -\frac{\lambda}{2} \int d^2z \frac{\partial \bar{p}_0}{\partial \psi} (p_0 \partial + \bar{p}_0 \bar{\partial}) p_0 + c.c \\ &= i \frac{\lambda}{2} \frac{\sigma}{2} \int d^2z (\frac{p_0}{z} - \frac{\bar{p}_0}{\bar{z}}) + c.c . \end{aligned} \tag{B.24}$$

By phase integral, the above vanishes unless $p_0 = e^{i\psi} \frac{z}{|z|}$, that is, $\sigma = 1$. Thus

$$\begin{aligned} \frac{\lambda}{2} \int d^2z \frac{\partial \bar{p}_0}{\partial \psi} \mathcal{I}_\lambda(p_0) + c.c &= -\frac{\lambda}{2} \sin\psi \delta_{\sigma,1} \int d^2z \frac{1}{|z|} + c.c \\ &= -2\pi\lambda\ell \sin\psi \delta_{\sigma,1} . \end{aligned} \tag{B.25}$$

Putting it all together,

$$\pi \ell^2 \dot{\psi} = -2\pi\lambda\ell \sin\psi \delta_{\sigma,1} \implies \dot{\psi} = -2\frac{\lambda}{\ell} \sin\psi \delta_{\sigma,1} . \tag{B.26}$$

Bibliography

[1] P. W. Anderson, *Basic notions of condensed matter physics.* Addison-Wesley, 1997.

[2] L. D. Landau, *On the theory of phase transitions*, *Zh. Eksp. Teor. Fiz.* **7** (1937) 19–32.

[3] L. D. Landau, *On the theory of superconductivity*, *Zh. Eksp. Teor. Fiz.* **20** (1950) 1064–1082.

[4] N. D. Mermin, *The topological theory of defects in ordered media*, *Rev. Mod. Phys.* **51** (Jul, 1979) 591–648.

[5] P. M. Chaikin and T. C. Lubensky, *Principles of condensed matter physics.* Cambridge university press, 2000.

[6] V. Volterra, *Sur l'équilibre des corps élastiques multiplement connexes*, *Annales scientifiques de l'École Normale Supérieure* **24** (1907) 401–517.

[7] G. I. Taylor, *The mechanism of plastic deformation of crystals. part i–theoretical*, *Proc. Royal Soc. Lond. Ser. A* **145** (1934) 362–387.

[8] J. Friedel, *Dislocations.* Pergamon Press, 1967.

[9] F. R. N. Nabarro, *Theory of crystal dislocations.* Clarendon Press, 1967.

[10] P.-G. d. Gennes and J. Prost, *The physics of liquid crystals.* Clarendon Press, 1993.

[11] S. Chandrasekhar and G. Ranganath, *The structure and energetics of defects in liquid crystals*, *Advances in Physics* **35** (1986) 507–596.

[12] M. Kleman, *Defects in liquid crystals*, *Reports on Progress in Physics* **52** (may, 1989) 555–654.

[13] G. P. Alexander, B. G.-g. Chen, E. A. Matsumoto and R. D. Kamien, *Colloquium: Disclination loops, point defects, and all that in nematic liquid crystals*, *Rev. Mod. Phys.* **84** (Apr, 2012) 497–514.

[14] T. H. R. Skyrme, *A unified field theory of mesons and baryons*, *Nuclear Physics* **31** (Apr., 1962) 556–569.

[15] N. Turok, *Global texture as the origin of cosmic structure*, *Phys. Rev. Lett.* **63** (Dec, 1989) 2625–2628.

[16] I. Chuang, R. Durrer, N. Turok and B. Yurke, *Cosmology in the laboratory: Defect dynamics in liquid crystals*, *Science* **251** (1991) 1336–1342.

[17] R. H. Brandenberger, *Topological defects and structure formation*, *International Journal of Modern Physics A* **09** (1994) 2117–2189.

[18] P. A. M. Dirac, *Quantised singularities in the electromagnetic field,*, *Proc. of the Royal Soc. of Lond. Ser. A* **133** (1931) 60–72.

[19] J. Preskill, *Magnetic monopoles*, *Annual Review of Nuclear and Particle Science* **34** (1984) 461–530.

[20] A. Belavin, A. Polyakov, A. Schwartz and Y. Tyupkin, *Pseudoparticle solutions of the yang-mills equations*, *Physics Letters B* **59** (1975) 85–87.

[21] M. Nakahara, *Geometry, Topology and Physics.* Taylor & Francis, 2003.

[22] D. R. Nelson, *Defects and geometry in condensed matter physics.* Cambridge University Press, 2002.

[23] S. Coleman, *Quantum sine-gordon equation as the massive thirring model*, *Phys. Rev. D* **11** (Apr, 1975) 2088–2097.

[24] R. Zwanzig, *Nonequilibrium statistical mechanics.* Oxford Univ. Press, 2001.

[25] S. Ramaswamy, *Issues in the statistical mechanics of steady sedimentation*, *Advances in Physics* **50** (May, 2001) 297–341.

[26] P. Jung, *Periodically driven stochastic systems*, *Physics Reports* **234** (1993) 175–295.

[27] F. Harper, R. Roy, M. S. Rudner and S. Sondhi, *Topology and broken symmetry in floquet systems*, *Annual Review of Condensed Matter Physics* **11** (2020) 345–368.

[28] S. Grossmann, D. Lohse and C. Sun, *High–reynolds number taylor-couette turbulence*, *Annual Review of Fluid Mechanics* **48** (2016) 53–80.

[29] S. Brazovskii, *Phase transition of an isotropic system to a nonuniform state*, *Zh. Eksp. Teor. Fiz.* **68** (1975) 175.

[30] J. Swift and P. C. Hohenberg, *Hydrodynamic fluctuations at the convective instability*, *Phys. Rev. A* **15** (Jan, 1977) 319–328.

[31] M. C. Cross and P. C. Hohenberg, *Pattern formation outside of equilibrium*, *Rev. Mod. Phys.* **65** (Jul, 1993) 851–1112.

[32] S. Ramaswamy, *The mechanics and statistics of active matter*, *Annual Review of Condensed Matter Physics* **1** (2010) 323–345.

[33] M. C. Marchetti, J. F. Joanny, S. Ramaswamy, T. B. Liverpool, J. Prost, M. Rao et al., *Hydrodynamics of soft active matter*, *Rev. Mod. Phys.* **85** (Jul, 2013) 1143–1189.

[34] S. Ramaswamy, *Active matter*, *Journal of Statistical Mechanics: Theory and Experiment* **2017** (May, 2017) 054002.

[35] S. Shankar, A. Souslov, M. J. Bowick, M. C. Marchetti and V. Vitelli, *Topological active matter*, `2010.00364`.

[36] F. Schweitzer, *Brownian agents and active particles: collective dynamics in the natural and social sciences*. Springer, 2007.

[37] E. Lifshitz and L. Pitaevskii, *Physical kinetics*, vol. 10 of *Course of Theoretical Physics*. Pergamon, 1981.

[38] F. S. Gnesotto, F. Mura, J. Gladrow and C. P. Broedersz, *Broken detailed balance and non-equilibrium dynamics in living systems: a review*, *Reports on Progress in Physics* **81** (apr, 2018) 066601.

[39] K. E. Kasza, A. C. Rowat, J. Liu, T. E. Angelini, C. P. Brangwynne, G. H. Koenderink et al., *The cell as a material*, *Current Opinion in Cell Biology* **19** (2007) 101–107.

[40] D. Needleman, *The material basis of life*, *Trends in Cell Biology* **25** (2015) 713–716.

[41] D. Needleman and Z. Dogic, *Active matter at the interface between materials science and cell biology*, *Nature Reviews Materials* **2** (Jul, 2017) 17048.

[42] W. Bialek, A. Cavagna, I. Giardina, T. Mora, E. Silvestri, M. Viale et al., *Statistical mechanics for natural flocks of birds*, *PNAS* **109** (2012) 4786–4791.

[43] A. Cavagna and I. Giardina, *Bird flocks as condensed matter*, *Annual Review of Condensed Matter Physics* **5** (2014) 183–207.

[44] Y. Katz, K. Tunstrøm, C. C. Ioannou, C. Huepe and I. D. Couzin, *Inferring the structure and dynamics of interactions in schooling fish*, *PNAS* **108** (2011) 18720–18725.

[45] K. Tunstrøm, Y. Katz, C. C. Ioannou, C. Huepe, M. J. Lutz and I. D. Couzin, *Collective states, multistability and transitional behavior in schooling fish*, *PLOS Computational Biology* **9** (02, 2013) 1–11.

[46] F. Ginelli, F. Peruani, M.-H. Pillot, H. Chaté, G. Theraulaz and R. Bon, *Intermittent collective dynamics emerge from conflicting imperatives in sheep herds*, *PNAS* **112** (2015) 12729–12734.

[47] J. Buhl, D. J. T. Sumpter, I. D. Couzin, J. J. Hale, E. Despland, E. R. Miller et al., *From disorder to order in marching locusts*, *Science* **312** (2006) 1402–1406.

[48] D. H. Kelley and N. T. Ouellette, *Emergent dynamics of laboratory insect swarms*, *Scientific Reports* **3** (Jan., 2013) 1073.

[49] M. Tennenbaum, Z. Liu, D. Hu and A. Fernandez-Nieves, *Mechanics of fire ant aggregations*, *Nature Materials* **15** (2015) 54–59.

[50] M. Sinhuber and N. T. Ouellette, *Phase coexistence in insect swarms*, *Phys. Rev. Lett.* **119** (Oct, 2017) 178003.

[51] M. Moussaïd, E. G. Guillot, M. Moreau, J. Fehrenbach, O. Chabiron, S. Lemercier et al., *Traffic instabilities in self-organized pedestrian crowds*, *PLOS Computational Biology* **8** (03, 2012) 1–10.

[52] J. L. Silverberg, M. Bierbaum, J. P. Sethna and I. Cohen, *Collective motion of humans in mosh and circle pits at heavy metal concerts*, *Phys. Rev. Lett.* **110** (May, 2013) 228701.

[53] A. Bottinelli, D. T. J. Sumpter and J. L. Silverberg, *Emergent structural mechanisms for high-density collective motion inspired by human crowds*, *Phys. Rev. Lett.* **117** (Nov, 2016) 228301.

[54] N. Bain and D. Bartolo, *Dynamic response and hydrodynamics of polarized crowds*, *Science* **363** (2019) 46–49.

[55] C. Dombrowski, L. Cisneros, S. Chatkaew, R. E. Goldstein and J. O. Kessler, *Self-concentration and large-scale coherence in bacterial dynamics*, *Phys. Rev. Lett.* **93** (Aug, 2004) 098103.

[56] A. Sokolov, I. S. Aranson, J. O. Kessler and R. E. Goldstein, *Concentration dependence of the collective dynamics of swimming bacteria*, *Phys. Rev. Lett.* **98** (Apr, 2007) 158102.

[57] H. H. Wensink, J. Dunkel, S. Heidenreich, K. Drescher, R. E. Goldstein, H. Löwen et al., *Meso-scale turbulence in living fluids*, *PNAS* **109** (2012) 14308–14313.

[58] J. Dunkel, S. Heidenreich, K. Drescher, H. H. Wensink, M. Bär and R. E. Goldstein, *Fluid dynamics of bacterial turbulence*, *Phys. Rev. Lett.* **110** (May, 2013) 228102.

[59] S. Zhou, A. Sokolov, O. D. Lavrentovich and I. S. Aranson, *Living liquid crystals*, *PNAS* **111** (2014) 1265–1270.

[60] D. Nishiguchi, K. H. Nagai, H. Chaté and M. Sano, *Long-range nematic order and anomalous fluctuations in suspensions of swimming filamentous bacteria*, *Phys. Rev. E* **95** (Feb, 2017) 020601.

[61] K. Copenhagen, R. Alert, N. S. Wingreen and J. W. Shaevitz, *Topological defects promote layer formation in Myxococcus xanthus colonies*, *Nature Physics* **17** (Feb., 2021) 211–215.

[62] I. H. Riedel, K. Kruse and J. Howard, *A self-organized vortex array of hydrodynamically entrained sperm cells*, *Science* **309** (2005) 300–303.

[63] Gruler, H., Dewald, U. and Eberhardt, M., *Nematic liquid crystals formed by living amoeboid cells **, *Eur. Phys. J. B* **11** (Sep, 1999) 187–192.

[64] R. Kemkemer, D. Kling, D. Kaufmann and H. Gruler, *Elastic properties of nematoid arrangements formed by amoeboid cells*, *Eur. Phys. J. E* **1** (2000) 215–225.

[65] B. Szabó, G. J. Szöllösi, B. Gönci, Z. Jurányi, D. Selmeczi and T. Vicsek, *Phase transition in the collective migration of tissue cells: Experiment and model*, *Phys. Rev. E* **74** (Dec, 2006) 061908.

[66] G. Duclos, C. Erlenkämper, J.-F. Joanny and P. Silberzan, *Topological defects in confined populations of spindle-shaped cells*, *Nat. Phys.* **13** (Sep, 2016) 58–62.

[67] K. Kawaguchi, R. Kageyama and M. Sano, *Topological defects control collective dynamics in neural progenitor cell cultures*, *Nature* **545** (Apr, 2017) 327–331.

[68] T. B. Saw, A. Doostmohammadi, V. Nier, L. Kocgozlu, S. Thampi, Y. Toyama et al., *Topological defects in epithelia govern cell death and extrusion*, *Nature* **544** (Apr, 2017) 212–216.

[69] N. Noll, M. Mani, I. Heemskerk, S. J. Streichan and B. I. Shraiman, *Active tension network model suggests an exotic mechanical state realized in epithelial tissues*, *Nature Physics* **13** (Aug, 2017) 1221–1226.

[70] C. Blanch-Mercader, V. Yashunsky, S. Garcia, G. Duclos, L. Giomi and P. Silberzan, *Turbulent dynamics of epithelial cell cultures*, *Phys. Rev. Lett.* **120** (May, 2018) 208101.

[71] E. Latorre, S. Kale, L. Casares, M. Gómez-González, M. Uroz, L. Valon et al., *Active superelasticity in three-dimensional epithelia of controlled shape*, *Nature* **563** (Oct, 2018) 203–208.

[72] Y. Maroudas-Sacks, L. Garion, L. Shani-Zerbib, A. Livshits, E. Braun and K. Keren, *Topological defects in the nematic order of actin fibres as organization centres of hydra morphogenesis*, *Nature Physics* (Nov., 2020) .

[73] J. Brugués and D. Needleman, *Physical basis of spindle self-organization*, *PNAS* **111** (2014) 18496–18500.

[74] A. Kumar, A. Maitra, M. Sumit, S. Ramaswamy and G. V. Shivashankar, *Actomyosin contractility rotates the cell nucleus*, *Scientific Reports* **4** (Jan, 2014) 3781.

[75] V. Narayan, S. Ramaswamy and N. Menon, *Long-lived giant number fluctuations in a swarming granular nematic*, *Science* **317** (2007) 105–108.

[76] J. Deseigne, O. Dauchot and H. Chaté, *Collective motion of vibrated polar disks*, *Phys. Rev. Lett.* **105** (Aug, 2010) 098001.

[77] N. Kumar, H. Soni, S. Ramaswamy and A. K. Sood, *Flocking at a distance in active granular matter*, *Nature Communications* **5** (Sep, 2014) 4688.

[78] J. Palacci, S. Sacanna, A. P. Steinberg, D. J. Pine and P. M. Chaikin, *Living crystals of light-activated colloidal surfers*, *Science* **339** (2013) 936–940.

[79] A. Bricard, J.-B. Caussin, N. Desreumaux, O. Dauchot and D. Bartolo, *Emergence of macroscopic directed motion in populations of motile colloids*, *Nature* **503** (Nov, 2013) 95–98.

[80] L. Giomi, N. Hawley-Weld and L. Mahadevan, *Swarming, swirling and stasis in sequestered bristle-bots*, *Proceedings of the Royal Society A: Mathematical, Physical and Engineering Sciences* **469** (2013) 20120637.

[81] M. Mijalkov, A. McDaniel, J. Wehr and G. Volpe, *Engineering sensorial delay to control phototaxis and emergent collective behaviors*, *Phys. Rev. X* **6** (Jan, 2016) 011008.

[82] C. Scholz, M. Engel and T. Pöschel, *Rotating robots move collectively and self-organize*, *Nature Communications* **9** (2018) 931.

[83] V. Schaller, C. Weber, C. Semmrich, E. Frey and A. R. Bausch, *Polar patterns of driven filaments*, *Nature* **467** (Sep, 2010) 73–77.

[84] T. Sanchez, D. T. N. Chen, S. J. DeCamp, M. Heymann and Z. Dogic, *Spontaneous motion in hierarchically assembled active matter*, *Nature* **491** (2012) 431–434.

[85] F. C. Keber, E. Loiseau, T. Sanchez, S. J. DeCamp, L. Giomi, M. J. Bowick et al., *Topology and dynamics of active nematic vesicles*, *Science* **345** (2014) 1135–1139.

[86] P. Guillamat, J. Ignés-Mullol and F. Sagués, *Taming active turbulence with patterned soft interfaces*, *Nature communications* **8** (2017) 564.

[87] P. W. Ellis, D. J. G. Pearce, Y.-W. Chang, G. Goldsztein, L. Giomi and A. Fernandez-Nieves, *Curvature-induced defect unbinding and dynamics in active nematic toroids*, *Nature Physics* **14** (Oct, 2017) 85–90.

[88] N. Kumar, R. Zhang, J. J. de Pablo and M. L. Gardel, *Tunable structure and dynamics of active liquid crystals*, *Sci. Adv.* **4** (Oct, 2018) eaat7779.

[89] B. A. Finlayson and L. E. Scriven, *Convective instability by active stress*, *Proc. Royal Soc. Lond. Ser. A* **310** (1969) 183–219.

[90] Y. Bouligand, *Liquid crystalline order in biological materials*, *Liquid Crystalline Order in Polymers* (1978) 261–297.

[91] A. Doostmohammadi, S. P. Thampi and J. M. Yeomans, *Defect-mediated morphologies in growing cell colonies*, *Phys. Rev. Lett.* **117** (2016) 048102.

[92] L. Giomi, M. J. Bowick, X. Ma and M. C. Marchetti, *Defect annihilation and proliferation in active nematics*, *Phys. Rev. Lett.* **110** (May, 2013) 228101.

[93] S. P. Thampi, R. Golestanian and J. M. Yeomans, *Velocity correlations in an active nematic*, *Phys. Rev. Lett.* **111** (2013) 118101.

[94] L. Giomi, *Geometry and topology of turbulence in active nematics*, *Physical Review X* **5** (2015) 031003.

[95] A. Doostmohammadi, T. N. Shendruk, K. Thijssen and J. M. Yeomans, *Onset of meso-scale turbulence in active nematics*, *Nature communications* **8** (2017) 15326.

[96] A. Doostmohammadi, J. Ignés-Mullol, J. M. Yeomans and F. Sagués, *Active nematics*, *Nat. Comm.* **9** (Aug, 2018) 3246.

[97] L. M. Pismen, *Dynamics of defects in an active nematic layer*, *Phys. Rev. E* **88** (Nov, 2013) 050502.

[98] S. Shankar, S. Ramaswamy, M. C. Marchetti and M. J. Bowick, *Defect unbinding in active nematics*, *Physical review letters* **121** (2018) 108002.

[99] S. Shankar and M. C. Marchetti, *Hydrodynamics of active defects: From order to chaos to defect ordering*, *Phys. Rev. X* **9** (Dec, 2019) 041047.

[100] F. Vafa, M. J. Bowick, M. C. Marchetti and B. I. Shraiman, *Multi-defect dynamics in active nematics*, `2007.02947`.

[101] Y.-H. Zhang, M. Deserno and Z.-C. Tu, *Dynamics of active nematic defects on the surface of a sphere*, *Phys. Rev. E* **102** (Jul, 2020) 012607.

[102] R. Aditi Simha and S. Ramaswamy, *Hydrodynamic fluctuations and instabilities in ordered suspensions of self-propelled particles*, *Phys. Rev. Lett.* **89** (Jul, 2002) 058101.

[103] P. G. de Gennes, *An analogy between superconductors and smectics a*, *Solid State Communications* **10** (1972) 753 – 756.

[104] L. Pismen, *Vortices in nonlinear fields: From liquid crystals to superfluids, from non-equilibrium patterns to cosmic strings*, vol. 100. Oxford University Press, 5, 1999.

[105] J. Toner and Y. Tu, *Long-range order in a two-dimensional dynamical* XY *model: How birds fly together*, *Phys. Rev. Lett.* **75** (Dec, 1995) 4326–4329.

[106] J. Toner and Y. Tu, *Flocks, herds, and schools: A quantitative theory of flocking*, *Phys. Rev. E* **58** (Oct, 1998) 4828–4858.

[107] K. Husain and M. Rao, *Emergent structures in an active polar fluid: Dynamics of shape, scattering, and merger*, *Phys. Rev. Lett.* **118** (Feb, 2017) 078104.

[108] B. Mahault, X.-c. Jiang, E. Bertin, Y.-q. Ma, A. Patelli, X.-q. Shi et al., *Self-propelled particles with velocity reversals and ferromagnetic alignment: Active matter class with second-order transition to quasi-long-range polar order*, *Phys. Rev. Lett.* **120** (Jun, 2018) 258002.

[109] H. Chaté, *Dry aligning dilute active matter*, *Annual Review of Condensed Matter Physics* **11** (2020) 189–212.

[110] K. Kruse, J. F. Joanny, F. Jülicher, J. Prost and K. Sekimoto, *Asters, vortices, and rotating spirals in active gels of polar filaments*, *Phys. Rev. Lett.* **92** (Feb, 2004) 078101.

[111] K. Kruse, J. Joanny, F. Jülicher, J. Prost and K. Sekimoto, *Generic theory of active polar gels: a paradigm for cytoskeletal dynamics*, *The European physical journal. E, Soft matter* **16** (January, 2005) 5—16.

[112] J. Elgeti, M. E. Cates and D. Marenduzzo, *Defect hydrodynamics in 2d polar active fluids*, *Soft Matter* **7** (2011) 3177–3185.

[113] A. Gopinath, M. F. Hagan, M. C. Marchetti and A. Baskaran, *Dynamical self-regulation in self-propelled particle flows*, *Phys. Rev. E* **85** (Jun, 2012) 061903.

[114] V. Schaller and A. R. Bausch, *Topological defects and density fluctuations in collectively moving systems*, *PNAS* **110** (2013) 4488–4493.

[115] K. Gowrishankar and M. Rao, *Nonequilibrium phase transitions, fluctuations and correlations in an active contractile polar fluid*, *Soft Matter* **12** (2016) 2040–2046.

[116] W. Kung, M. Cristina Marchetti and K. Saunders, *Hydrodynamics of polar liquid crystals*, *Phys. Rev. E* **73** (Mar, 2006) 031708.

[117] D. W. Thompson, *On Growth and Form.* Cambridge Univ. Press, 1917.

[118] J. B. A. Green and J. Sharpe, *Positional information and reaction-diffusion: two big ideas in developmental biology combine*, *Development* **142** (04, 2015) 1203–1211.

[119] A. M. Turing, *The chemical basis of morphogenesis*, *Philosophical Transactions of the Royal Society of London. Series B, Biological Sciences* **237** (1952) 37–72.

[120] T. Lecuit and P.-F. Lenne, *Cell surface mechanics and the control of cell shape, tissue patterns and morphogenesis*, *Nature Reviews Molecular Cell Biology* **8** (Aug, 2007) 633–644.

[121] C.-P. Heisenberg and Y. Bellaïche, *Forces in tissue morphogenesis and patterning*, *Cell* **153** (2013) 948–962.

[122] D. Gilmour, M. Rembold and M. Leptin, *From morphogen to morphogenesis and back*, *Nature* **541** (Jan, 2017) 311–320.

[123] P. Gross, K. V. Kumar and S. W. Grill, *How active mechanics and regulatory biochemistry combine to form patterns in development*, *Annual Review of Biophysics* **46** (2017) 337–356.

[124] T. Lecuit and L. Mahadevan, *Morphogenesis one century after on growth and form*, *Development* **144** (2017) 4197–4198.

[125] N. C. Heer and A. C. Martin, *Tension, contraction and tissue morphogenesis*, *Development* **144** (2017) 4249–4260.

[126] K. D. Irvine and B. I. Shraiman, *Mechanical control of growth: ideas, facts and challenges*, *Development* **144** (2017) 4238–4248.

[127] C. Collinet and T. Lecuit, *Programmed and self-organized flow of information during morphogenesis*, *Nature Reviews Molecular Cell Biology* **22** (Apr, 2021) 245–265.

[128] S. C. Al-Izzi and R. G. Morris, *Active flows and deformable surfaces in development*, `2103.12264`.

[129] S. B. Carroll, J. K. Grenier and S. D. Weatherbee, *From DNA to Diversity: Molecular Genetics and the Evolution of Animal Design.* Blackwell Science Inc, 2001.

[130] A. S. Wilkins, *The Evolution of Developmental Pathways.* Sinauer Associates, Inc, 2002.

[131] E. H. Davidson, *The Regulatory Genome.* Elsevier, 2006.

[132] E. M. Meyerowitz, *Genetic control of cell division patterns in developing plants*, *Cell* **88** (1997) 299–308.

[133] E. Coen, R. Kennaway and C. Whitewoods, *On genes and form*, *Development* **144** (2017) 4203–4213.

[134] M. Mavrakis, O. Pourquié and T. Lecuit, *Lighting up developmental mechanisms: how fluorescence imaging heralded a new era*, *Development* **137** (2010) 373–387.

[135] F. Bosveld, I. Bonnet, B. Guirao, S. Tlili, Z. Wang, A. Petitalot et al., *Mechanical control of morphogenesis by fat/dachsous/four-jointed planar cell polarity pathway*, *Science* **336** (2012) 724–727.

[136] R. Tomer, K. Khairy, F. Amat and P. J. Keller, *Quantitative high-speed imaging of entire developing embryos with simultaneous multiview light-sheet microscopy*, *Nature Methods* **9** (Jul, 2012) 755–763.

[137] U. Krzic, S. Gunther, T. E. Saunders, S. J. Streichan and L. Hufnagel, *Multiview light-sheet microscope for rapid in toto imaging*, *Nature Methods* **9** (Jul, 2012) 730–733.

[138] P. J. Keller, *Imaging morphogenesis: Technological advances and biological insights*, *Science* **340** (2013) .

[139] P. Pantazis and W. Supatto, *Advances in whole-embryo imaging: a quantitative transition is underway*, *Nature Reviews Molecular Cell Biology* **15** (May, 2014) 327–339.

[140] B. I. Shraiman, *Mechanical feedback as a possible regulator of tissue growth*, *PNAS* **102** (2005) 3318–3323.

[141] R. Farhadifar, J.-C. Röper, B. Aigouy, S. Eaton and F. Jülicher, *The influence of cell mechanics, cell-cell interactions, and proliferation on epithelial packing*, *Current Biology* **17** (2007) 2095–2104.

[142] F. Vafa, M. J. Bowick, B. I. Shraiman and M. C. Marchetti, *Fluctuations can induce local nematic order and extensile stress in monolayers of motile cells*, *Soft Matter* **17** (2021) 3068–3073.

[143] F. Vafa, *Defect dynamics in active polar fluids vs. active nematics*, `2009.10723`.

[144] F. Vafa and L. Mahadevan, *Active nematic defects and epithelial morphogenesis*, `2105.01067`.

[145] A. Doostmohammadi, S. P. Thampi, T. B. Saw, C. T. Lim, B. Ladoux and J. M. Yeomans, *Celebrating soft matter's 10th anniversary: Cell division: a source of active stress in cellular monolayers*, *Soft Matter* **11** (2015) 7328–7336.

[146] D. Dell'Arciprete, M. L. Blow, A. T. Brown, F. D. C. Farrell, J. S. Lintuvuori, A. F. McVey et al., *A growing bacterial colony in two dimensions as an active nematic*, *Nat. Comm.* **9** (Oct, 2018) 4190.

[147] R. Mueller, J. M. Yeomans and A. Doostmohammadi, *Emergence of active nematic behavior in monolayers of isotropic cells*, *Phys. Rev. Lett.* **122** (Feb, 2019) 048004.

[148] L. Balasubramaniam, A. Doostmohammadi, T. B. Saw, G. H. N. S. Narayana, R. Mueller, T. Dang et al., *Investigating the nature of active forces in tissues reveals how contractile cells can form extensile monolayers*, *Nature Materials* (Feb., 2021) .

[149] P. Srivastava, P. Mishra and M. C. Marchetti, *Negative stiffness and modulated states in active nematics*, *Soft Matter* **12** (2016) 8214–8225.

[150] E. Putzig, G. S. Redner, A. Baskaran and A. Baskaran, *Instabilities, defects, and defect ordering in an overdamped active nematic*, *Soft Matter* **12** (2016) 3854–3859.

[151] S. Santhosh, M. R. Nejad, A. Doostmohammadi, J. M. Yeomans and S. P. Thampi, *Activity induced nematic order in isotropic liquid crystals*, *Journal of Statistical Physics* (2020) 1–11.

[152] M. R. Nejad, A. Doostmohammadi and J. M. Yeomans, *Memory effects, arches and polar defect ordering at the cross-over from wet to dry active nematics*, *Soft Matter* (2021) .

[153] J. Prost, F. Jülicher and J.-F. Joanny, *Active gel physics*, *Nature physics* **11** (2015) 111–117.

[154] A. Brugués, E. Anon, V. Conte, J. H. Veldhuis, M. Gupta, J. Colombelli et al., *Forces driving epithelial wound healing*, *Nature physics* **10** (2014) 683–690.

[155] J. Notbohm, S. Banerjee, K. J. Utuje, B. Gweon, H. Jang, Y. Park et al., *Cellular contraction and polarization drive collective cellular motion*, *Biophysical journal* **110** (2016) 2729–2738.

[156] L. Landau and E. Lifshitz, *Fluid Mechanics*. Butterworth-Heinemann, 1998.

[157] P. G. D. Gennes, *Short range order effects in the isotropic phase of nematics and cholesterics*, *Molecular Crystals and Liquid Crystals* **12** (1971) 193–214.

[158] L. Giomi, T. B. Liverpool and M. C. Marchetti, *Sheared active fluids: Thickening, thinning, and vanishing viscosity*, *Phys. Rev. E* **81** (May, 2010) 051908.

[159] E. J. Hemingway, P. Mishra, M. C. Marchetti and S. M. Fielding, *Correlation lengths in hydrodynamic models of active nematics*, *Soft Matter* **12** (2016) 7943–7952.

[160] M. C. Calderer and B. Mukherjee, *Chevron patterns in liquid crystal flows*, *Physica D: Nonlinear Phenomena* **98** (1996) 201–224.

[161] H. Baza, T. Turiv, B.-X. Li, R. Li, B. M. Yavitt, M. Fukuto et al., *Shear-induced polydomain structures of nematic lyotropic chromonic liquid crystal disodium cromoglycate*, *Soft Matter* **16** (2020) 8565–8576.

[162] S. P. Gido and E. L. Thomas, *Lamellar diblock copolymer grain boundary morphology. 4. tilt boundaries*, *Macromolecules* **27** (1994) 6137–6144.

[163] A. J. Vromans and L. Giomi, *Orientational properties of nematic disclinations*, *Soft matter* **12** (2016) 6490–6495.

[164] X. Tang and J. V. Selinger, *Orientation of topological defects in 2d nematic liquid crystals*, *Soft Matter* **13** (2017) 5481–5490.

[165] S. J. DeCamp, G. S. Redner, A. Baskaran, M. F. Hagan and Z. Dogic, *Orientational order of motile defects in active nematics*, *Nature materials* **14** (2015) 1110.

[166] A. Patelli, I. Djafer-Cherif, I. S. Aranson, E. Bertin and H. Chaté, *Understanding dense active nematics from microscopic models*, *Phys. Rev. Lett.* **123** (Dec, 2019) 258001.

[167] A. Doostmohammadi, M. F. Adamer, S. P. Thampi and J. M. Yeomans, *Stabilization of active matter by flow-vortex lattices and defect ordering*, *Nature communications* **7** (2016) 10557.

[168] D. J. G. Pearce, J. Nambisan, P. W. Ellis, A. Fernandez-Nieves and L. Giomi, *Scale-free defect ordering in passive and active nematics*, `2004.13704`.

[169] K. Thijssen, M. R. Nejad and J. M. Yeomans, *Large scale ordering of active defects*, `2005.01164`.

[170] D. Cortese, J. Eggers and T. B. Liverpool, *Pair creation, motion, and annihilation of topological defects in two-dimensional nematic liquid crystals*, *Physical Review E* **97** (2018) 022704.

[171] C. Denniston, *Disclination dynamics in nematic liquid crystals*, *Phys. Rev. B* **54** (Sep, 1996) 6272–6275.

[172] R. Temam, *Inertial manifolds*, *The Mathematical Intelligencer* **12** (Sep, 1990) 68–74.

[173] M. V. Dyke, *perturbation methods in fluid dynamics.* Academic, 1964.

[174] J. C. Neu, *Vortices in complex scalar fields*, *Physica D: Nonlinear Phenomena* **43** (1990) 385–406.

[175] L. M. Pismen and J. D. Rodriguez, *Mobility of singularities in the dissipative ginzburg-landau equation*, *Phys. Rev. A* **42** (Aug, 1990) 2471–2474.

[176] I. Fredholm, *Sur une classe d'équations fonctionnelles*, *Acta Math.* **27** (1903) 365–390.

[177] J. F. Brady and G. Bossis, *Stokesian dynamics*, *Annual Review of Fluid Mechanics* **20** (1988) 111–157.

[178] A. Maitra, M. Lenz and R. Voituriez, *Chiral active hexatics: Giant number fluctuations, waves, and destruction of order*, *Phys. Rev. Lett.* **125** (Dec, 2020) 238005.

[179] L. Giomi and M. C. Marchetti, *Polar patterns in active fluids*, *Soft Matter* **8** (2012) 129–139.

[180] L. Chen, C. F. Lee and J. Toner, *Mapping two-dimensional polar active fluids to two-dimensional soap and one-dimensional sandblasting*, *Nature communications* **7** (2016) 12215.

[181] J. Toner, Y. Tu and S. Ramaswamy, *Hydrodynamics and phases of flocks*, *Ann. Phys.* **318** (2005) 170 – 244.

[182] A. Souslov, B. C. van Zuiden, D. Bartolo and V. Vitelli, *Topological sound in active-liquid metamaterials*, *Nature Physics* **13** (Nov, 2017) 1091–1094.

[183] F. Pacard and T. Rivière, *Linear and Nonlinear Aspects of Vortices: The Ginzburg-Landau Model.* Birkhäuser, Boston, MA, 2000.

[184] I. S. Aranson and L. S. Tsimring, *Pattern formation of microtubules and motors: Inelastic interaction of polar rods*, *Phys. Rev. E* **71** (May, 2005) 050901.

[185] I. S. Aranson and L. S. Tsimring, *Theory of self-assembly of microtubules and motors*, *Phys. Rev. E* **74** (Sep, 2006) 031915.

[186] H. Youn Lee and M. Kardar, *Macroscopic equations for pattern formation in mixtures of microtubules and molecular motors*, *Phys. Rev. E* **64** (Oct, 2001) 056113.

[187] S. Sankararaman, G. I. Menon and P. B. Sunil Kumar, *Self-organized pattern formation in motor-microtubule mixtures*, *Phys. Rev. E* **70** (Sep, 2004) 031905.

[188] K. Thijssen and A. Doostmohammadi, *Binding self-propelled topological defects in active turbulence*, *Phys. Rev. Research* **2** (Oct, 2020) 042008.

[189] T. Turiv, J. Krieger, G. Babakhanova, H. Yu, S. V. Shiyanovskii, Q.-H. Wei et al., *Topology control of human fibroblast cells monolayer by liquid crystal elastomer*, *Science Advances* **6** (2020) .

[190] T. C. Lubensky and J. Prost, *Orientational order and vesicle shape*, *Journal de Physique II* **2** (Mar., 1992) 371–382.

[191] H. S. Seung and D. R. Nelson, *Defects in flexible membranes with crystalline order*, *Phys. Rev. A* **38** (Jul, 1988) 1005–1018.

[192] J. R. Frank and M. Kardar, *Defects in nematic membranes can buckle into pseudospheres*, *Phys. Rev. E* **77** (Apr, 2008) 041705.

[193] D. J. Drew, "Hydra (YPM IZ 091796)." Digital Image: Yale Peabody Museum of Natural History, 2018.

[194] R. S. Hamilton, *Three-manifolds with positive ricci curvature*, *J. Differential Geom.* **17** (1982) 255–306.

[195] A. Mietke, F. Jülicher and I. F. Sbalzarini, *Self-organized shape dynamics of active surfaces*, *PNAS* **116** (2019) 29–34.

[196] L. Metselaar, J. M. Yeomans and A. Doostmohammadi, *Topology and morphology of self-deforming active shells*, *Physical review letters* **123** (2019) 208001.

[197] B. Galliot, *Hydra, a fruitful model system for 270 years*, *The International Journal of Developmental Biology* **56** (2012) 411–423.

[198] E. Braun and K. Keren, *Hydra regeneration: Closing the loop with mechanical processes in morphogenesis*, *BioEssays* **40** (2018) 1700204.

[199] R. Aufschnaiter, R. Wedlich-Söldner, X. Zhang and B. Hobmayer, *Apical and basal epitheliomuscular f-actin dynamics during hydra bud evagination*, *Biology Open* **6** (2017) 1137–1148.

[200] Benamou, Jean-David, Froese, Brittany D. and Oberman, Adam M., *Two numerical methods for the elliptic monge-ampère equation*, *ESAIM: M2AN* **44** (2010) 737–758.

[201] X. Gu, F. Luo, J. Sun and S. T. Yau, *Variational principles for minkowski type problems, discrete optimal transport, and discrete monge-ampere equations*, `1302.5472`.

[202] L. Cui, X. Qi, C. Wen, N. Lei, X. Li, M. Zhang et al., *Spherical optimal transportation*, *Computer-Aided Design* **115** (2019) 181–193.

[203] X. D. Gu, *Geometric optimal transportation*, 2020.

[204] X. D. Gu, *Spherical optimal transportation*, 2021.

[205] E. Coen, A.-G. Rolland-Lagan, M. Matthews, J. A. Bangham and P. Prusinkiewicz, *The genetics of geometry*, *PNAS* **101** (2004) 4728–4735.

[206] A. Maitra and S. Ramaswamy, *Oriented active solids*, *Phys. Rev. Lett.* **123** (Dec, 2019) 238001.

[207] D. J. Montell, *Morphogenetic cell movements: Diversity from modular mechanical properties*, *Science* **322** (2008) 1502–1505.

[208] K. Barlan, M. Cetera and S. Horne-Badovinac, *Fat2 and lar define a basally localized planar signaling system controlling collective cell migration*, *Developmental Cell* **40** (2017) 467 – 477.e5.

[209] M. Poujade, E. Grasland-Mongrain, A. Hertzog, J. Jouanneau, P. Chavrier, B. Ladoux et al., *Collective migration of an epithelial monolayer in response to a model wound*, *Proc. Natl. Acad. Sci. USA* **104** (2007) 15988–15993.

[210] V. Hakim and P. Silberzan, *Collective cell migration: a physics perspective*, *Rep. Prog. in Phys.* **80** (apr, 2017) 076601.

[211] T. Vicsek, A. Czirók, E. Ben-Jacob, I. Cohen and O. Shochet, *Novel type of phase transition in a system of self-driven particles*, *Phys. Rev. Lett.* **75** (Aug, 1995) 1226–1229.

[212] E. Bertin, M. Droz and G. Grégoire, *Hydrodynamic equations for self-propelled particles: microscopic derivation and stability analysis*, *J. of Phys. A: Math. Theor.* **42** (oct, 2009) 445001.

[213] A. U. Oza and J. Dunkel, *Antipolar ordering of topological defects in active liquid crystals*, *New Journal of Physics* **18** (2016) 093006.

[214] C.-S. Lin, *The local isometric embedding in r3 of two-dimensional riemannian manifolds with gaussian curvature changing sign cleanly*, *Communications on Pure and Applied Mathematics* **39** (1986) 867–887.

[215] C. S. Lin, *The local isometric embedding in* $\mathbf{R}^3$ *of 2-dimensional riemannian manifolds with nonnegative curvature*, *Journal of Differential Geometry* **21** (1985) 213–230.

[216] Q. Han and J.-X. Hong, *Isometric embedding of riemannian manifolds in euclidean spaces*, *Mathematical Surveys and Monographs* **130** (2006) .

[217] A. Polyakov, *Quantum geometry of bosonic strings*, *Physics Letters B* **103** (1981) 207–210.

[218] S. Deser and B. Zumino, *Consistent supergravity*, *Physics Letters B* **62** (1976) 335–337.

[219] L. Brink, P. Di Vecchia and P. Howe, *A locally supersymmetric and reparametrization invariant action for the spinning string*, *Physics Letters B* **65** (1976) 471–474.

[220] C. Blanch-Mercader, P. Guillamat, A. Roux and K. Kruse, *Quantifying material properties of cell monolayers by analyzing integer topological defects*, *Phys. Rev. Lett.* **126** (Jan, 2021) 028101.

[221] C. Blanch-Mercader, P. Guillamat, A. Roux and K. Kruse, *Integer topological defects of cell monolayers: Mechanics and flows*, *Phys. Rev. E* **103** (Jan, 2021) 012405.